NORTHWESTERN UNIVERSITY

Modeling Large-Scale Dynamics and Intercellular Communication in Bacterial Biofilms

A DISSERTATION

SUBMITTED TO THE GRADUATE SCHOOL

IN PARTIAL FULFILLMENT OF THE REQUIREMENTS

for the degree

DOCTOR OF PHILOSOPHY

Field of Engineering Sciences and Applied Mathematics

By

Noah Ford

EVANSTON, ILLINOIS

September 2020

ABSTRACT

Modeling Large-Scale Dynamics and Intercellular Communication in Bacterial Biofilms

Noah Ford

We present two novel, computational models of biofilm growth within an experimental flow cell. First, we use asymptotic approximations to develop a reduced model that captures the large-scale dynamics within an entire flow cell. The reduced model's predicted growth and nutrient distribution are close to the values predicted by previous models at a fraction of the computational cost. Experimentalists can use this model to better understand the internal concentration and growth distribution throughout their flow cells. Second, we present a modified model of the metabolic and voltage oscillations experimentally observed in some *Bacillus subtilis* cultures. We develop a two-dimensional simulation from this model that mimics the two-dimensional structure of the experiments and allows us to directly compare the model to experimental data. These two models provide a closer look at some of the complex and interesting behaviors biofilms can exhibit.

Acknowledgements

Many people supported and contributed to the work that I present here, and I greatly appreciate their help. The Applied Math Department at Northwestern was a comfortable home where I could discuss a range of interesting problems with professors and other students, and the work presented here comes directly from these conversations.

First and foremost, I would like to thank my advisor, Dr. David Chopp. He helped guide me during every stage of my research. When I began my research, he proposed a range of ideas for potential research projects and continued to provide suggestions and guidance as I found my own path. He was supportive as I explored new research projects and learned about a range of other subjects that I found interesting. He gave thoughtful feedback on all of my writing, which greatly improved the quality of the work.

I would also like to thank Dr. Aaron Packman, who served on my qualifying exam committee, and Dr. Michael Miksis, who served on both my qualifying exam committee and on my thesis committee. They listened to my research presentations each year and helped keep me focused on a productive research path. I thank them for their helpful comments and suggestions along the way.

I would like to thank Dr. Arthur Prindle, who also served on my thesis committee, and his graduate student Garth Fisher. They enthusiastically introduced me to a new and interesting biological phenomena that I then modeled as part of my thesis work. They

were always eager to meet, and they explained to me many components of bacteria that I had not previously been exposed to. I appreciate their patience as I learned.

I would like to thank Joshua Levy, a graduate student in Applied Math who was in the same cohort. He was always available to bounce around ideas, and he was able to provide some biological background to the problems that I was working on.

Finally, I would like to thank my mom and my dad for encouraging me to follow my academic goals. I have wanted to earn a doctorate since middle school, and my parents supported my journey while I explored a variety of academic fields. My path has not always been simple, but they were there to provide some much needed support as I confronted each challenge.

Table of Contents

[1]Adapted by permission from Springer Nature Customer Service Centre GmbH: Springer Nature Bulletin of Mathematical Biology, A Dimensionally Reduced Model of Biofilm Growth Within a Flow Cell, Noah Ford, David Chopp, Copyright 2020 Society for Mathematical Biology (2020) https://www.springer.com/journal/11538

List of Tables

List of Figures

CHAPTER 1

Introduction

A biofilm is a colony of bacteria that grows on a surface. The bacteria produce extracellular polymeric substance, or EPS, which forms a matrix that connects the bacteria to the surface and to each other. These bacteria are called sessile, as opposed to the familiar planktonic bacteria that float or swim in search of nutrients. Many types of bacteria can switch between these two distinct modes or phenotypes. Biofilms commonly grow on a range of surfaces that are submerged in fluid. These surfaces provide an attachment point for the bacteria from which they consume nutrients available in the environment. Biofilms exhibit a range of unique, collective behaviors that can benefit the individual cells and improve their ability to survive and reproduce. Scientists study biofilms because the colonies can greatly impact human life in a variety of ways, including by corroding machinery and causing infections. Both experimentation and modeling are common tools that help scientists to better understand the complex behaviors of biofilms within their various environments.

Bacterial biofilms grow on many types of surfaces located in distinct environments. Biofilms grow on several surfaces of humans' and other mammals' bodies including in the digestive tract [**12**], on the skin [**13**], and on teeth, on which biofilms often produce dental plaque [**14**]. An image of a biofilm within the intestines of a rat is shown in Figure 1.1. Biofilms also grow in other natural and human-made environments such as in streams [**15**], on plants [**16**], and on the hulls of ships [**17**]. An image of a biofilm growing in a

stream is shown in Figure 1.2. Different bacteria or consortia of bacteria are suited to different environments based on each environment's nutrient availability and prevalent stressors. Within the intestines, the bacteria consume some of the nutrients found in the food that their host animal ingests. In stream environments, bacteria largely consume the oxygen and various organic materials present in the flow. Because of the differences in the environment, the types of bacteria found in an animal's intestine will likely not appear in the same proportions in a biofilm within a stream. A closer look at the types of bacteria present in biofilms in these different environments is provided in [**18**].

Biofilms typically exhibit a defined life cycle. In this life cycle, planktonic cells attach to a surface, change their phenotype to become sessile, grow into a mature biofilm, and then some cells switch back into planktonic cells and detach from the biofilm to colonize new surfaces. The biofilm life cycle is described in more detail in [**19**]. This cycle is a good example of the mutualistic cooperation that arises in biofilms, in which the coordinated growth improves the bacteria's ability to survive. A particular example of this coordinated growth can be seen in the development of fruiting bodies, which some biofilms create in their detachment phase. The fruiting bodies are formations in which a group of bacteria that are enclosed within the biofilm switch their phenotype from sessile to planktonic. These planktonic cells contained within the biomass are sometimes referred to as seeds. The fruiting bodies safely incubate these swimmers before they are released to colonize other surfaces. More details on the development of these structures can be found in [**20**].

The development of fruiting bodies is just one example of a communal behavior observed in biofilms. Biofilms exhibit many collective behaviors, which also include the formation of complex patterns and shapes in some biofilms' structure. The purpose of

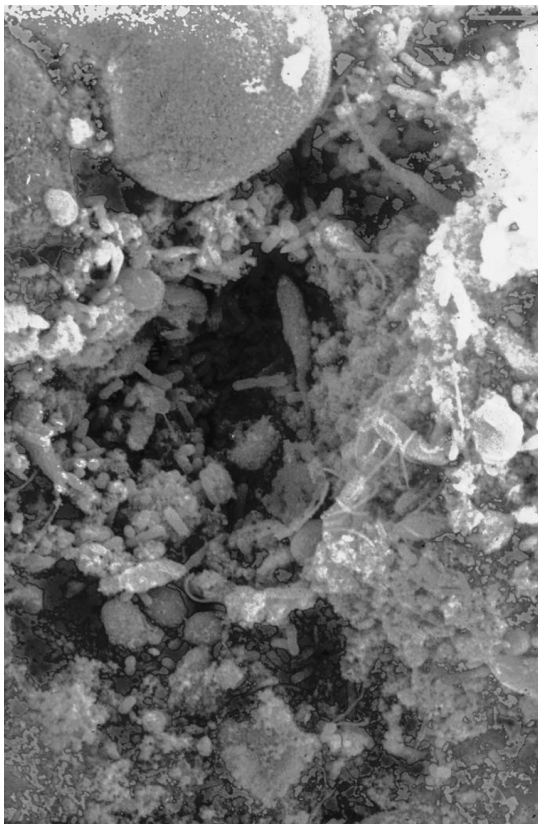

Figure 1.1. Reproduced from [**2**]. This image depicts a biofilm within a rat's intestine that has a diverse population. Copyright Springer-Verlag Berlin Heidelberg 2007. Reprinted by permission from Springer Nature Customer Service Centre GmbH: Springer Nature, The Biofilm Primer: Direct Observations by J. W. Coserterton, Copyright 2007, Springer-Verlag Berlin Heidelberg (2007) https://www.springer.com/gp/book/9783540680215

Figure 1.2. Reproduced from [**2**]. Top image is of an alpine stream under Marmolata Spire in the Bugaboo Mountains of British Columbia. Bottom image is from a transmission electron microscope of a biofilm on a methacrylate surface immersed in this stream for 30 minutes. Copyright Springer-Verlag Berlin Heidelberg 2007. Reprinted by permission from Springer Nature Customer Service Centre GmbH: Springer Nature, The Biofilm Primer: The Microbiology of the Healthy Human Body by J. W. Coserterton, Copyright 2007, Springer-Verlag Berlin Heidelberg (2007) https://www.springer.com/gp/book/9783540680215

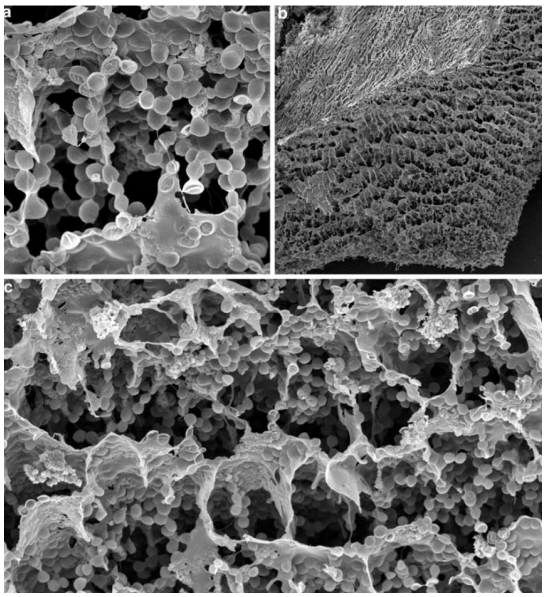

Figure 1.3. Reproduced from [**2**]. Images from a scanning electron microscope of a biofilm that expresses a honeycomb pattern. Copyright Springer-Verlag Berlin Heidelberg 2007. Reprinted by permission from Springer Nature Customer Service Centre GmbH: Springer Nature, The Biofilm Primer: Direct Observations by J. W. Coserterton, Copyright 2007, Springer-Verlag Berlin Heidelberg (2007) https://www.springer.com/gp/book/9783540680215

these complex structures is often to increase the nutrient access of the bacteria throughout the biofilm. An example of such a structure can be seen in Figure 1.3 where the bacteria form a honeycomb pattern which promotes microscopic flow through the biomass. This flow allows nutrients to disperse faster than diffusion alone, and the bacteria are better able to survive. These physical structures are visual examples of the cooperative nature of biofilms.

There are many advantages to living within a biofilm, including metabolic, genetic, and protective benefits [**2**]. Biofilms can grow in many environments in which few planktonic

bacteria could survive. For example, biofilms can survive in the low-nutrient environment of mountain streams, which typically have few free-floating, planktonic bacteria [**2**]. Biofilms also provide bacteria with the opportunity to share pieces of their DNA with their neighbors, which allows the cells to incorporate advantageous genes into their genome, improving their fitness. The connection between biofilm formation and the transfer of genetic material is explored in [**21**]. Another advantage of living in a biofilm is that the bacteria in the colony are significantly more resistant to outside stressors, most notably to antibiotics. The possible mechanisms that contribute to bacteria's resistance could include the physical barrier of the colony, environmental differences, and the genetic expression of the cells [**22**]. The protection provided by the physical barrier can be inferred by the lower antibiotic susceptibility of clumps of biofilm compared to physically disrupted pieces of biofilms [**23**]. A genetic component of the protection is suggested by experiments demonstrating that biofilms of *Pseudomonas aeruginosa* consisting of a certain mutant strain are more susceptible to antibiotics than biofilms consisting of wild-type bacteria [**24**], which implies that the genetic expression of the bacteria may provide some of the protection. These significant benefits of living in a biofilm demonstrate why many bacteria spend a portion of their life living within one of these communities.

We study biofilms because they are important to both our built environment and our bodies. Biofilms can grow on machinery and equipment, which can lead to damaging bulk formation or the corrosion of these surface. For example, biofilm growth in ultrafiltration systems decreases the flux of water through the filtration system reducing their efficiency [**25**]. Biofilms of sulfate-reducing bacteria can also corrode machinery [**26**]. Scientists are continually exploring new ways to manage biofilm growth. For example, bacteriophages

may be able to reduce the formation of biofilms on the ultrafiltration systems and improve the fluid flux through the filters [**25**]. In some filtration systems, biofilms can actually improve the performance of the filters, particularly in filtering wastewater. Biofilms within a filtration system can remove carbon from wastewater and prevent biofilms from forming on downstream surfaces [**27**]. Reducing biofilm growth in industrial systems is only one example of how managing biofilm growth can save substantial amounts of money in industrial applications.

Biofilms also live in the bodies of many animals, including humans, and can greatly impact their health. The presence of some biofilms can be beneficial to the host animal. For example, they contribute to the digestive process within the intestines. However, biofilms can also lead to infections particularly when there is excess growth or growth somewhere that is typically bacteria free. Medical devices such as catheters, pacemakers, and other implants, are ideal surfaces for biofilm growth because they are inert and do not have the natural defenses of human cells. Biofilm colonization on venous catheters of hospitalized patients can lead to sepsis [**28**]. A thick biofilm can also form on biological surfaces in the body such as in the lungs and sinuses causing chronic infections. Biofilms can play a role in infections, particularly in cystic fibrosis, in which biofilms often cause chronic inflammation in patients' lungs [**29, 30**]. Scientists dedicate a large amount of resources to finding ways to fight these infections. Some of the techniques used to fight these infections include removing infected objects, using antibiotics, and even administering dispersal agents to prevent the bacteria from forming a biofilm [**31**]. Because of biofilms' resistance to common antibacterial methods, scientist continue to study biofilms and their complex properties to find new ways to control their growth.

Scientists use a combination of experiments and simulations to study biofilms. The experiments provide important data on how a biofilm behaves in different environments, examining behaviors such as the growth rate and how biofilms respond to various factors such as the concentration of nutrients and the flow rate. Though bacteria are simpler than many other types of cells, these organisms still express many complex behaviors that are controlled by chemical pathways in the cell. These reaction networks can be quite complicated, and we often have an incomplete picture of the networks for even the most well-studied bacteria. Scientists perform experiments to probe the mechanisms that give rise to an observed behavior, and they often compare wild-type bacteria to mutant strains with the hope of connecting a difference in behavior to a difference in genes. For example, the authors of [**24**] compare wild-type and mutant strains of *Pseudomonas aeruginosa* to suggest that genetics may contribute to antibiotic resistance. These types of experiments typically explore a single mechanism at a time, and the combined effect of cellular differences can be difficult to predict. We can use modeling to methodically combine the data from individual experiments to develop a more precise picture of the cellular behavior.

To gain a clearer picture of the driving forces behind a biofilm's behavior, mathematicians develop models that reproduce important experimental features. A model that reproduces the observed dynamics of the system can demonstrate that certain proposed mechanisms of a bacterium's chemical network are sufficient or insufficient to explain the observed behavior. A well-fitted model that is based on known physical and biological relationships can provide even more confidence in the proposed role of a particular mechanism. Models not only help us to understand the bacteria's behavior, they can also

be used to predict behavior and other relevant quantities within the biofilm system. A model is particularly useful for predicting bacteria's behavior in a new environment and for approximating data that is difficult to measure in an experiment. Both experiments and modeling are integral components in understanding these bacterial systems, which can help scientists formulate control strategies for biofilms in industrial environments and within the body.

In Chapters 3 and 4, we present two new methods to simulate biofilms that provide insight into behaviors seen in experiments. In Chapter 3, we introduce a dimensionally reduced model of biofilm growth within a flow cell. This model provides a closer look at the dynamics within experimental flow cells in which biofilms are often studied. Typically only a small portion of the cell is imaged in an experiment due to the limitations of the microscope. Estimating the local environmental conditions at the point of observation is challenging because upstream bacteria consume substrates and alter these concentrations in the fluid as it moves from the inlet port to the observation point. The absence of accurate environmental data presents a challenge to understanding biofilm growth and quantitatively comparing observed growth to the models.

It is possible to estimate these local conditions by simulating the biofilm in the entire chamber using existing numerical methods, but in practice this computation is expensive. The cost of simulating a small region containing a biofilm is large to begin with, and simulating the entire flow cell is prohibitive. In Chater 3, we propose an alternative approach that uses asymptotic approximations to reduce the dimensionality of computing biofilm growth and the growth-limiting substrate concentration in the flow cell. This simplified

system runs orders of magnitude faster than previous models and allows researchers to better understand the growth and the nutrient concentrations throughout the flow cell.

In Chapter 4, we introduce a two-dimensional model of potassium signaling and oscillatory growth in a biofilm, which may promote nutrient sharing within the biofilm. Biofilms often exhibit cooperative behavior to manage the distribution of nutrients, such as developing channels and structures that enable nutrients to penetrate the biomass more deeply. In this chapter we explore *Bacillus subtilis'* oscillatory growth pattern that may emerge from potassium signaling. This behavior was introduced in [**10**] and in [**8**] as another mechanism for biofilm cooperation to improve the nutrient availability at the center of the colony.

Previous studies, such as [**9**], primarily used one-dimensional models to examine this behavior. In Chapter 4, we develop a two-dimensional model and introduce a new method of cell-to-cell communication in which the cells react to changing potassium levels instead of to the absolute potassium level. We show that this model can more accurately represent some important features of the experimental data in [**8**], and we use the model to explore the spatial variations in the oscillation patterns seen in these experiments.

CHAPTER 2

Methods

2.1. Previous Work

To simulate a biofilm growing in a flow cell, we split the domain into two regions: the interior of the biofilm where the bacteria are located, Ω^-, and the surrounding fluid that provides the nutrients that the bacteria use to survive and grow, Ω^+. We show a visual representation of the two subregions of the domain in Figure 2.1. To simulate the flow-cell environment, we solve for the fluid flow in Ω^+, the nutrient distribution in the entire domain, and the biomass growth in Ω^-.

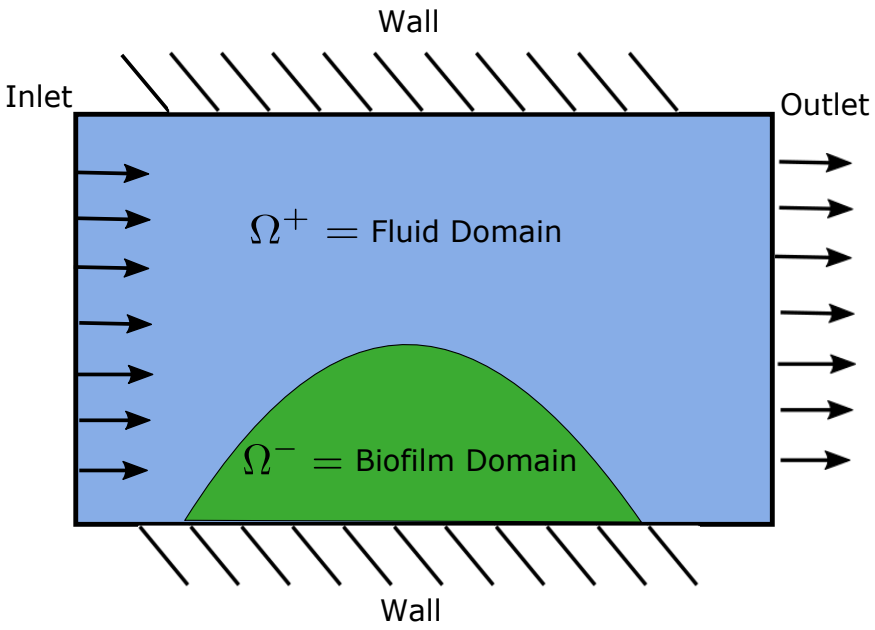

Figure 2.1. An illustration of a two-dimensional, flow-cell domain

In the fluid domain, Ω^+, we solve for the fluid velocity around the biofilm. The flow pattern strongly influences the biofilm's growth because the flow carries important nutrients to the biofilm's interface. Though the flow provides these essential nutrients, high flow can create a level of shear stress that limits the biofilm's growth. The flow can also deform the biofilm, but typically these deformations are small enough that most models ignore their effects. Though many environments have some fluid flow, some environments may not have any flow in the surrounding fluid. In these environments the nutrients diffuse passively through the fluid to reach the bacteria, which often exhibit limited growth due to the lower nutrient availability. The environmental characteristics of the flow or lack thereof greatly affect the biofilm's growth, which makes accurately calculating the flow an important component of the biofilm simulation.

We solve for the nutrient distribution in both the fluid, Ω^+, and the biofilm, Ω^-. Modeling these nutrients in the fluid results in an advection-diffusion equation in Ω^+. The nutrients diffuse from the fluid into the biofilm at its interface. In Ω^- the nutrients diffuse through the spaces between the cells and can be carried by micro-scale flows through channels that form within the biomass. Tracking these channels and then solving for the flow through these spaces would be quite challenging. Most models treat the biofilm as a homogeneous substance that has no defined channels and thus no flow. This simplification allows the computations to consider only the diffusive transport of the nutrients. Most models use an effective diffusion coefficient to solve for the diffusion within the biofilm. The effective diffusion coefficient can be estimated from experiments and is generally a fraction of the diffusion coefficient within an aqueous solution [**32**]. Only representing the

diffusion and not the advection inside the biofilm can underestimate its nutrient intake and internal transport, but we are still able to accurately represent most biofilm systems.

As the bacteria reproduce, the cells push out the biomass around them, and we track the evolving interface between Ω^+ and Ω^-. In Ω^-, the model represents common quantities such as living cells, extracellular polymeric substance, and the various species of bacteria within the biofilm. The proportions of these biological materials typically shift as bacteria reproduce because the bacteria produce the biomass components at different rates and the growth can push the biomass from one region into a different region. There are three primary computational methods that have been used to track the biomass growth: the cellular automata model [**33**], the agent-based model [**34**], and the continuum model (the one-dimensional model was introduced in [**35**] and the multi-dimensional model was introduced in [**36**]).

The cellular automata model tracks the growing biomass by dividing the domain of the flow cell into a rectangular grid, and then it tracks the biomass quantities within each grid box. One of the first applications of this model to a biofilm is discussed in [**33**]. It was further developed in [**37**], [**38**], and [**39**]. In the model, some of the grid boxes are completely full of biomass and other boxes have no biomass and only fluid. More detailed versions of the model may track the density of the various biomass components in each box. Though this method allows the simulation to track the shape and makeup of the biofilm, it's growth algorithm often relies on bacteria from one box moving into a randomly chosen neighboring box, which may not be physically accurate. For example, in [**40**], once the biomass in one box reaches a threshold, half of the biomass in the box is randomly displaced to a neighboring box. Under these growth conditions, changes

to the model's representation of the biomass can lead to differences in the mixture of the biomass components [**40**]. These complications in implementation have reduced the model's popularity within the biofilm modeling community.

Another method to simulate the biomass growth is an agent-based model where the simulation tracks collections of cells and biological substances within the biofilm. This method was introduced by [**34**] in which the authors develop a simulation framework for bacterial biofilms. A multidimensional model based on this method was introduced in [**41**] which examines larger "particles" of biomass instead of individual cells. The model was improved in [**42**] to model the EPS and cellular detachment in more depth. The growth algorithm commonly used in these models is the shoving algorithm in which the agents shove each other to grow outward [**40**]. Agent-based models provide a more detailed representation of small collections of bacteria, which can be useful when studying many biological phenomena that emerge from the behavior of a small number of cells. However, since these models use the small collections of cells to represent the entire biofilm, they may require more detail than necessary to model large-scale phenomena.

The third model commonly used for tracking the biomass growth is the continuum model. This model is based on a volume fraction formulation that continuously defines the proportions of each biomass at each point. For example, if the biofilm near a grid point is made up of equal quantities of living cells and EPS, the model defines both of these proportions to be 0.5, but it does not distinguish the precise location of the cells and the EPS. This model was introduced by [**35**] as a one-dimensional model, but has since been extended to multi-dimensional models in [**36**] and extended to multispecies biofilms in [**43**]. The continuum model is a logical choice for simulating large-scale, aggregate

behavior because the model can easily capture the collective behavior without delving into the detail of tracking individual cells.

In our studies we use the continuum model to approximate the biofilm's growth. We use the biofilm simulation system developed in [**5**] as the basis of our simulations and algorithm development. This simulation system is described in more detail within [**44**], and it is used as the modeling framework in [**45, 46**]. This system begins by initializing a biofilm colony from a user-prescribed shape. It can then solve for the fluid flow around the biofilm, the nutrient distributions within the fluid and the biofilm, and the resulting growth of the biofilm.

In [**5**], the simulation uses a fluid solver based on an extended finite-element method (XFEM) formulation. This solver was developed in [**47**], and it solves for the flow using a Stokes-flow approximation, which assumes that the flow is slow enough to be laminar. The XFEM formulation allows the fluid solver to accurately capture the fluid velocities near the biofilm interface, but the solver runs slowly. Here, we address the long runtime by replacing the solver, which we discuss in the following section.

The biofilm simulation in [**5**] solves for the nutrient concentration throughout the fluid and biomass in the domain using a quasi-steady-state approximation and a mixture of boundary conditions to represent the physical boundaries of the flow cell. The system solves the solute equations as quasi-steady-state because the time-scale of diffusion is much faster than the time scales of consumption and growth. Since diffusion occurs relatively quickly, the solute distribution is approximately equal to its diffusive steady state within the biofilm. Here, the boundary conditions for the nutrients include a Dirichlet boundary at the inlet, which is set to the bulk concentration, no-flux conditions at the two walls on

the top and bottom of the flow cell, and a far-field condition at the outlet in which the derivative in the outgoing direction is set to zero. The boundary condition at the interface of the biofilm and the fluid requires that the concentration and the flux of the nutrients are continuous. The resulting nutrient distribution helps to determine the biofilm's growth, and the simulation tracks the moving biofilm interface.

The biofilm system from [**5**] uses the level-set method to track the location of the biofilm/fluid interface. This method was introduced in [**48**], and it is discussed further in [**49**], [**50**], [**51**], and references therein. This method tracks an interface within a domain by defining the function ϕ, where the zero level-set of ϕ corresponds to the boundary. The interface is then the image of $\phi^{-1}(0)$. Furthermore, ϕ is defined so that $||\nabla\phi|| \approx 1$ throughout the domain so that the value of ϕ at any point is approximately equal to the signed distance from that point to the nearest point on the biofilm interface. In Figure 2.2, we show that the level-set method can accurately represent the irregular boundary of the three biofilm colonies from [**8**], which we will discuss in Chapter 4.

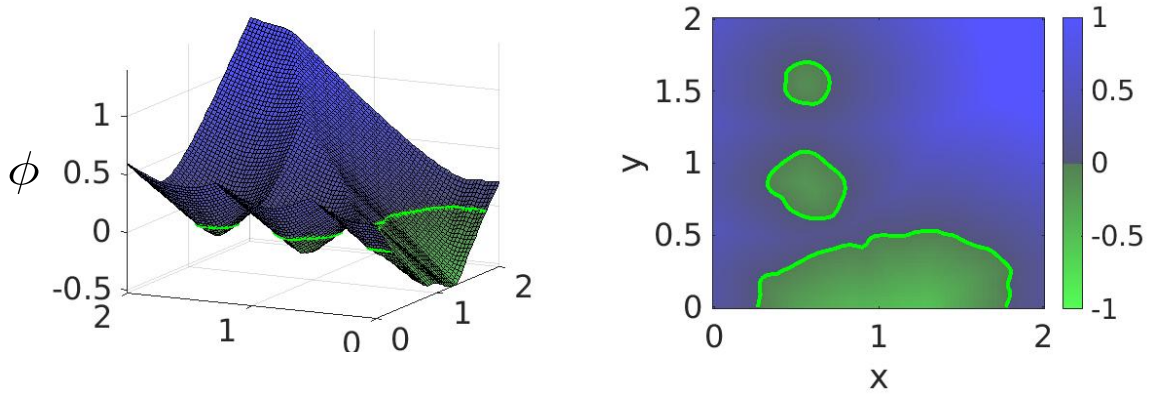

Figure 2.2. The level-set function, ϕ, represents the shape of the biofilms. The zero level-set of ϕ, drawn in light green, defines the boundary of the biofilm colonies. There are three distinct colonies. The regions colored green are the biofilms and the region colored blue is the surrounding fluid.

The continuum model solves for the biofilm's growth using the level-set method in which the growth velocity is the solution to the potential function

$$\nabla^2 \Phi = g, \tag{2.1}$$

$$\vec{V} = \nabla \Phi, \tag{2.2}$$

where g is the local growth, Φ is the potential function, and $\vec{V}$ is the biomass velocity. The biofilm interface, defined by ϕ, moves according to the biomass velocity, $\vec{V}$ from Equation (2.2), evaluated along the boundary. The speed, F, of the moving interface is equal to the normal component of the biomass velocity, which is calculated as $F = \vec{V} \cdot \vec{n}$ where $\vec{n}$ is the unit normal at the interface. Once we have defined the speed of the interface, we evolve ϕ using the level-set evolution equation:

$$\phi_t + F||\phi|| = 0. \tag{2.3}$$

The speed, F, is only defined at the boundary, but to evolve the level-set function, ϕ, we need the values of F at the grid points. We use velocity extensions to find velocity values at the grid points throughout the domain. The velocity extensions are constructed so that the gradient of ϕ remains approximately 1, which improves the accuracy and stability of the solution. A quick method to accurately compute velocity extensions is provided in [**52**], and we use this method here. Despite our efforts to maintain the gradient of ϕ using velocity extensions, the norm of ϕ may gradually begin to deviate from 1 after successive updates. Once the gradient sufficiently deviates from 1, we reinitialize the surface to maintain the accuracy of the solution. [**53**] introduced the reinitialization

of level-set functions to compute minimal surfaces. Since that initial usage, numerous alternative approaches to reinitialization have been proposed. For example, an iterative method to reinitialize the level-set function is presented in [**54**]. Here, we use an improved method for reinitializing the level-set function presented in [**55**]. More discussion on the implementation of the level-set method can be found in [**50**], [**51**], and references therein.

We use the biofilm simulation system developed in [**5**] as both a benchmark and as a basis for new models. To use the system in these contexts, we made a few important updates to the system. First, we updated the fluid solver in [**5**] simulation to improve the entire simulation's runtime. Second, we added the ability to solve for cellular state variables and to solve for the nutrient distribution as time dependent. We use the updated model to validate a new, dimensionally reduced model and to model the oscillatory growth behavior observed in *Bacillus subtilis* in [**8**].

The fluid solver in the system from [**5**] ran slowly, and it accounted for the majority of the simulation time. We replaced the fluid solver from [**5**] to improve the speed. We implemented a high-performance fluid solver that runs on a Graphics Processing Unit, or GPU, which runs up to 30 times faster than the original solver. This change improves the simulation speed, which allows for quicker comparisons to our new, dimensionally reduced model.

We also updated the simulation to allow it to represent cellular state variables. Models typically represent diffusive quantities that diffuse fast enough that the biofilm's growth minimally affects the quantity's distribution. However, this assumption of fast diffusion does not apply to cellular state variables which are attached to a single cell and do not diffuse. Since these state variables move at the same time-scale as the biofilm's

growth, we account for the biofilm's growth when solving for the state variables. The state variables are an important component in the oscillatory growth behavior observed in *Bacillus subtilis*.

We enabled the simulation to solve for the solutes and state variables as time dependent. Previously, the simulation solved for all these variables as if they were at steady state. This assumption is accurate for most biofilms in which the diffusion of the quantities occurs more quickly than the changes in the bacteria's intake and release. However, the oscillatory behavior in *Bacillus subtilis* is based on rapid changes in the solutes, which also affect the state variables. Solving for the solutes and state variables as time dependent allows us to capture this oscillatory phenomenon. In the following sections, we discuss these changes in more detail.

2.2. High-Performance Fluid Solver

We implemented a high-performance, fluid solver within the biofilm system to improve the speed of the simulation. The original fluid solver was based on an extended finite-element method (XFEM) formulation. Finite elements are a common choice when solving for fluid flow around an irregular shape such as the interface of a biofilm. The elements are able to accurately solve for fluid in the irregular domain. However, creating the finite-element mesh can be computationally costly and time consuming. Furthermore, the XFEM method computes the fluid velocity values near the biofilm interface using additional basis functions. Each time the boundary moves, the simulation creates a new set of basis functions and incorporates them into the calculation, and solving the new system of equations can be time-consuming. This method for solving for the fluid flow

around the irregular shape of a biofilm is presented in [**47**]. Thankfully, the growth is slow enough that the system typically only recalculates the flow every 10-50 steps. However, solving for the flow every few steps could still constitute around 90% of the simulation time.

We introduced a high-performance, finite-difference algorithm to quickly compute the fluid flow around the biofilm. To create this solver, we first assume that the flow is slow enough that it can be modeled as laminar. This assumption is accurate for most experiments performed in biofilm flow cells. If the flow is too fast near the biofilm, the bacteria experience high levels of shear stress and cannot grow. To keep the bacteria from detaching, experimentalists typically set the flow to be slow enough so that it is laminar.

The laminar flow assumption allows us to use a Stokes-flow approximation to solve for the fluid velocities. This approximation provides the following set of equations:

$$\mu \nabla^2 u = \frac{\partial P}{\partial x}, \tag{2.4}$$

$$\mu \nabla^2 v = \frac{\partial P}{\partial y}, \tag{2.5}$$

$$\nabla^2 P = 0, \tag{2.6}$$

where u is the x-directional velocity, v is the y-directional velocity, P is the pressure, and μ is the viscosity. The domain of the flow cell is a rectangle with an inlet on the left side, an outlet on the right side, and walls on the top and the bottom of the domain. The fluid moves through this domain and around the biomass. At the inlet we use an inflow boundary condition where $u = u_0$, $v = 0$, and $\partial u/\partial x = 0$, and at the outlet we approximate a far-field boundary with the conditions $\partial u/\partial x = 0$, $v = 0$, and $P = 0$.

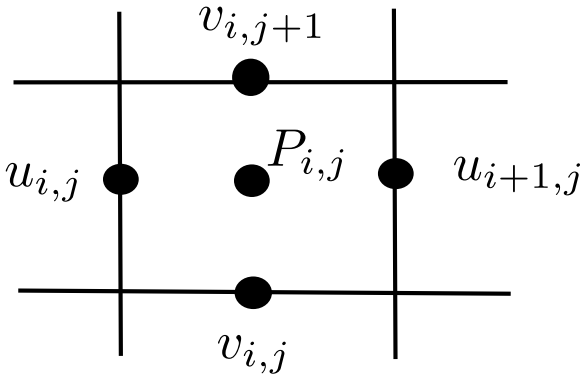

Figure 2.3. Marker-and-cell (MAC) grid for fluid solve

At the interior walls and at the biofilm interface we have a no-slip and no-penetration boundary condition, which requires that $u = 0$, $v = 0$, and $\nabla P \cdot \vec{n} = 0$, where $\vec{n}$ is the outward normal.

We solve these equations by discretizing the domain using a uniform mesh with a marker-and-cell, or MAC, grid, which is a discretized grid with staggered points for different variables. This grid is represented in Figure 2.3.

We discretize Equations (2.4) and (2.5) and implement a successive-over-relaxation (SOR) scheme with a red-black ordering. In this algorithm, all the red points are updated simultaneously and then all the black points are updated simultaneously. Once all points of one color are updated, the points of the other color are updated using those newer values in their calculations. In this scheme we solve for both u and v using a red-black ordering for their respective grids. The red-black grid for u is shown in Figure 2.4.

The red-black SOR algorithm consists of the following steps to solve for u and v:

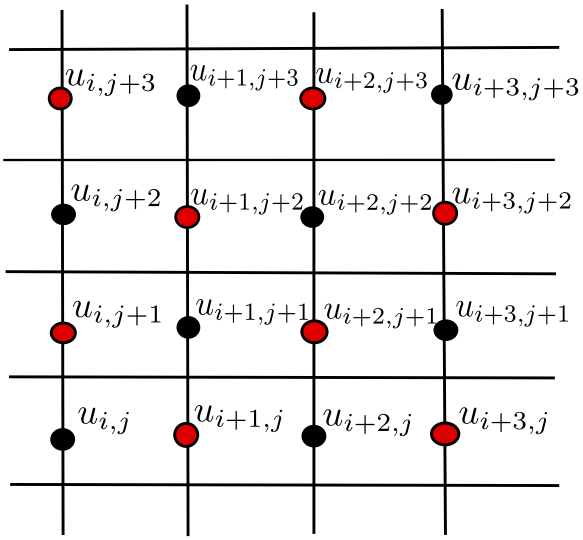

Figure 2.4. Red-black grid for computing u, the $x-$directional velocity

- Update red and black grid points for u, where red nodes are updated on half steps and black nodes are updated on whole steps

(2.7)

$$u_{i,j}^{n+1/2} = (1-\omega)u_{i,j}^{n} + \omega(u_{i+1,j}^{n} + u_{i-1,j}^{n} + u_{i,j+1}^{n} + u_{i,j-1}^{n} + (P_{i,j}^{n} - P_{i-1,j}^{n})dx/\mu)/4,$$

(2.8)

$$u_{i,j}^{n+1} = (1-\omega)u_{i,j}^{n+1/2} + \omega(u_{i+1,j}^{n+1/2} + u_{i-1,j}^{n+1/2} + u_{i,j+1}^{n+1/2} + u_{i,j-1}^{n+1/2} + (P_{i,j}^{n} - P_{i-1,j}^{n})dx/\mu)/4.$$

- Update red and black grid points for v, where red nodes are updated on half steps and black nodes are updated on whole steps

(2.9)

$$v_{i,j}^{n+1/2} = (1-\omega)v_{i,j}^{n} + \omega(v_{i+1,j}^{n} + v_{i-1,j}^{n} + v_{i,j+1}^{n} + v_{i,j-1}^{n} + (P_{i,j}^{n} - P_{i,j-1}^{n})dy/\mu)/4,$$

(2.10)

$$v_{i,j}^{n+1} = (1-\omega)v_{i,j}^{n+1/2} + \omega(v_{i+1,j}^{n+1/2} + v_{i-1,j}^{n+1/2} + v_{i,j+1}^{n+1/2} + v_{i,j-1}^{n+1/2} + (P_{i,j}^{n} - P_{i,j-1}^{n})dy/\mu)/4.$$

The boundary points for u and v can be updated according to the desired boundary conditions. Near the biofilm, the no flux and no penetration boundary conditions require that u and v are zero at the interface. We extrapolate the velocities to points within the biofilm that border the fluid so that the velocities are approximately zero at the boundary. These grid points inside the biofilm then have negative values for u and v. If a grid point inside the biofilm has only one neighbor that is inside the fluid domain, we use a one-dimensional, linear extrapolation to calculate the u and v velocities at the interior point. If an interior grid point has multiple neighbors outside in the fluid domain, then we perform multiple one-dimensional extrapolations and approximate the value at the interior grid point using the average. While the boundary computations produce a small degree of error, which we will examine in more detail below, they produce relatively accurate solutions.

We update pressure to maintain continuity within the fluid, meaning that we ensure that the divergence is zero. In our discretization from Figure 2.3 we ensure that the

divergence within each square on the grid is equal to zero, which we compute as

$$\text{Divergence} = \frac{u_{i+1,j}^{n+1} - u_{i,j}^{n+1}}{dx} + \frac{v_{i,j+1}^{n+1} - v_{i,j}^{n+1}}{dy}. \tag{2.11}$$

If the divergence is negative within a box, then some amount of fluid is disappearing there, and we increase pressure in the box to decrease the amount of fluid flowing into it. By decreasing the amount of fluid flowing into the box, we balance the inflowing and outflowing fluid to maintain continuity in the flow. Conversely, if the divergence is positive in a box, then fluid is being created there, and we decrease pressure to reduce the amount of fluid leaving the box, which balances the fluid fluxes. The pressure is updated as follows:

$$P_{i,j}^{n+1} = P_{i,j}^{n} - \alpha[(u_{i+1,j}^{n+1} - u_{i,j}^{n+1})/dx + (v_{i,j+1}^{n+1} - v_{i,j}^{n+1})/dy], \tag{2.12}$$

$$= P_{i,j}^{n} - \alpha \times \text{Divergence in box surrounding } P_{i,j}. \tag{2.13}$$

In solving for the fluid flow, we have two iteration parameters, ω and α, where ω is the iteration parameter for updating u and v, and α is the iteration parameter for updating P. The pressure update does not follow the same form as an SOR update, so the user should test various iteration parameters to find appropriate parameters for their fluid system. In implementing this scheme, we used $\omega = 0.5$ and $\alpha = \mu$, the fluid viscosity. In most of our simulations, the fluid viscosity was set to that $\mu = 0.0011$ kilograms per meter second.

One major benefit of using an iterative scheme is that the solver can use the values of u, v, and P from a previous fluid solve as an initial starting point for the following solve. Since the biofilm grows slowly, the solution to these equations only changes a small

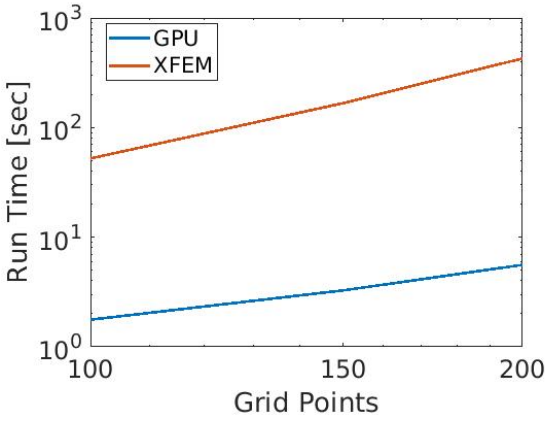

Figure 2.5. Comparison of runtimes of XFEM-based fluid solver and GPU-based fluid solver on a Linux-based computer with a NVIDIA Tesla K20c graphics card. The values on the x-axis of the figure are the number of grid points in the x-direction of the domain. There are half as many grid points in the y-direction.

amount as the biofilm grows. Using initial values that are close to the new solution allows the solver to converge quickly. In the XFEM-based solver, the program updates the basis functions near the biofilm interface each time it solves for the fluid, thereby changing the system of equations, which the program re-solves from scratch. Though the iterative scheme improves its speed by using previous values, the main speedup comes from our ability to parallelize the computations on a GPU.

We implemented the fluid solver using OpenCL, which we ran on two different machines: a Macbook Pro with a Radeon Pro 560 4 GB graphics card and a Linux-based computer with a NVIDIA Tesla K20c graphics card. The high performance fluid solver runs about 30 times faster on the NVIDIA graphics card than the finite element solver on the same machine. This speed provides significant improvement in the runtime of the entire simulation. A comparison between the runtimes of the GPU fluid solver and the XFEM fluid solver is presented in Figure 2.5.

The x-directional fluid velocity as computed by the high-performance solver is shown in Figure 2.6 along with errors for the computation. The relative error shows the difference between the GPU-based fluid solver and the XFEM-based solver. The two methods differ the most near the biofilm boundary. This error decreases as the number of grid points increase, but both solvers provide good estimates for the fluid velocities within the context of the biofilm simulation.

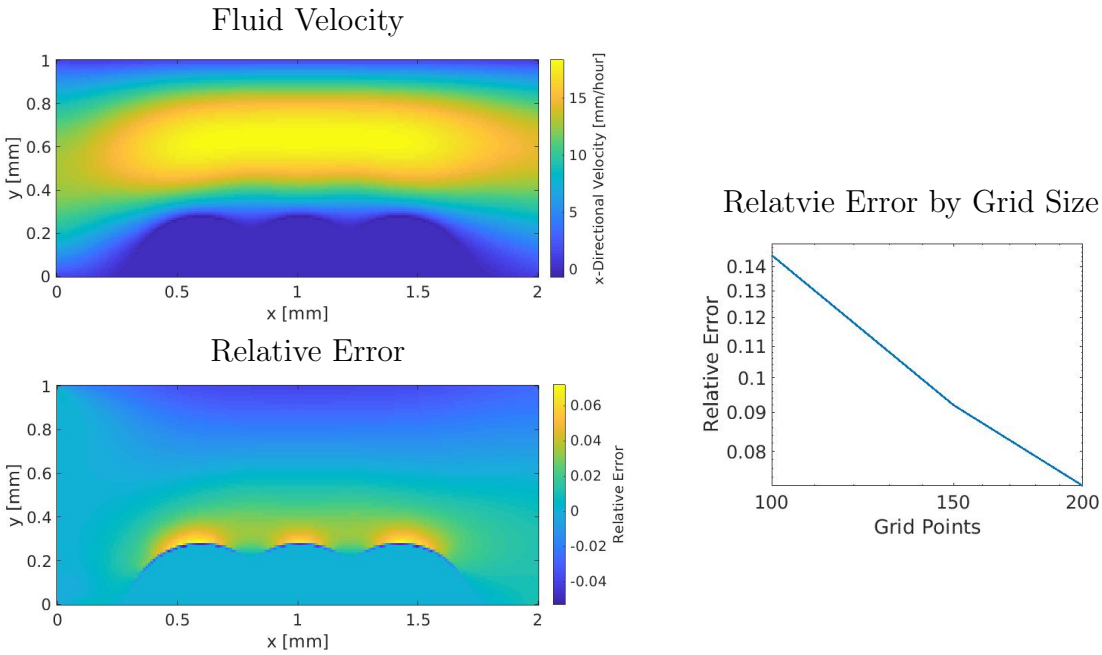

Figure 2.6. Comparison of the high-performance fluid solver to XFEM fluid solver. The fluid velocity and relative error are shown for a grid size of 200×100. The relative error on this grid is the difference between the two solvers relative to the inflow velocity. The plot on the right shows that the infinity-norm error between the GPU solver and the XFEM solver decreases with number of grid points.

In addition to creating a fluid solver on the GPU, we also parallelized the solute solver on the GPU. We found that while the solute computation ran five to ten times faster in the GPU version compared to the traditional, sparse-matrix solver, the quicker solver

did not significantly reduce the runtime of the whole simulation because the solute solve typically makes up less than 10% of the runtime of the entire simulation.

We gained a significant reduction in the full simulation runtime by parallelizing parts of the code that took the most amount of time. Parallelizing the fluid solver, which took up to 90% of the simulation time, reduced the simulation runtime significantly while parallelizing the solute solver, which accounted for around 10% of the simulation time, only provided a modest speedup. Though we did not see much speedup in the simulation from parallelizing the time-independent solute solver, it is possible that we could see a larger speedup from parallelizing the time-dependent solute solver that we discuss in the following section.

2.3. State and time-dependent variables

We use a modified version of the biofilm simulation system presented in [**5**] to model the oscillatory growth phenomenon observed in experiments of *B. subtilis* performed in [**8**]. To model this behavior within the simulation system, we add the ability to handle state variables that are internal quantities within the cells and the ability to solve for the state variables and the diffusive quantities as time dependent. The time dependence is necessary because the quantities experience fast fluctuations that occur at the same time-scale as diffusion. Variations in time and space are intrinsic to the physics of the biofilm behavior observed in [**8**], and we capture these affects within the state variables and the time-dependent solutions.

State variables are quantities that are attached to a particular cell, which include variables such as the cell's voltage differential, its internal potassium level, and its internal

glutamate level. These quantities are internal to a cell and do not directly affect the corresponding quantities within neighboring cells. We model these quantities using ordinary differential equations that we solve at each grid point on the spatial grid.

Since these state variables represent traits of specific cells, the values move with the cells as they are pushed outward by the overall biomass growth. Let Q be a state variable. Then the equation representing Q as the biofilm grows is

$$\frac{\partial Q}{\partial t} = F(Q) - \nabla \cdot (Q\vec{U}), \tag{2.14}$$

where F is the evolution equation for Q within a single cell, and $\vec{U}$ is the biomass velocity at that point. The movement of these state variables within the biomass growth is depicted in Figure 2.7. The values of the state variables are carried by the cellular movement in the direction of the growth vectors. Typically, we do not incorporate this advection term while solving for the diffusive quantities because diffusion occurs much more quickly than the growth, meaning that the growth has little impact on the distributions. As the diffusion coefficient limits to zero, the movement of the biomass growth becomes more influential in the quantity's distribution. We incorporate growth in computing the internal state variables, which experience no diffusion.

To add state variables to the biofilm simulation system, we allow the user to specify a zero diffusion rate for a quantity within the biofilm. This zero diffusion rate signifies that these quantities do not diffuse from cell to cell, but remain attached to cells as they grow. We ensure that the simulation only solves for these quantities within the biofilm, and they are solved at the same grid points at which the solutes are calculated.

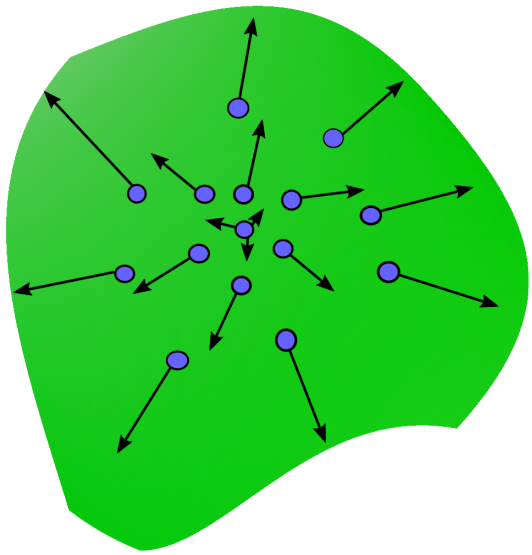

Figure 2.7. As the biofilm grows, the state variables move with the biomass velocity. The state variables are represented as blue dots, and they move along the nearby vectors.

The final change we made to the biofilm simulation is that we enable the system to solve for the state variables and the diffusive quantities as time dependent. Many biofilm models, including the model from [**5**], approximate diffusive quantities within the biofilm as though the system is at a quasi-steady state. This assumption is accurate in most systems because diffusion occurs quickly compared to the changes in the cellular uptake or release that would cause the solute profile to deviate from steady state. However, in the biofilm system in [**8**], particularly within the potassium concentration, the diffusive quantities can change quickly. Additionally, the state variables are highly affected by the diffusive quantities and can change at similar time scales. Because of the speed at which these quantities evolve, we solve for both the diffusive quantities and the state variables as time dependent. We discuss the biofilm system in [**8**] in Chapter 4.

To implement the time-dependent, solute solver, we use a Crank-Nicolson scheme for the diffusive term and a two-step, Adams-Bashforth scheme for the nonlinear, reaction terms. The Crank-Nicolson scheme is a semi-implicit algorithm that is second order in time and numerically stable. The Adams-Bashforth scheme is an explicit method that is also second order in time.

To solve the time-dependent problem, the simulation must perform more time steps than it performed in the quasi-steady-state-approximation because it closely tracks the small changes in the internal and diffusive quantities. Each step can be time consuming since it requires solving a matrix equation on a two-dimensional grid with 5-10 variables. Using a second-order scheme can reduce the number of solves required to achieve an acceptable solution.

Figure 2.8 shows the time-dependent, oxygen distribution in a biofilm flow cell that can accurately be modeled as quasi-steady-state, meaning that its growth and oxygen consumption are slow-changing relative to the diffusion rate. In this environment, the time-dependent solution and the quasi-stead-state solution should be approximately equal. Figure 2.8 shows a comparison of these two solutions. The largest errors occur near the boundary of the biofilm. This error, which we measure as the largest difference between the time-dependent and time-independent solution, shrinks with smaller time steps.

Updating the model from [**5**] enables us to explore new problems with greater speed. Creating the high-performance fluid solver that runs on a GPU greatly improves the run-time of the simulation, and we harness this speed in validating a reduced model of biofilm growth, discussed in Chapter 3. Furthermore, the added ability to handle state variables

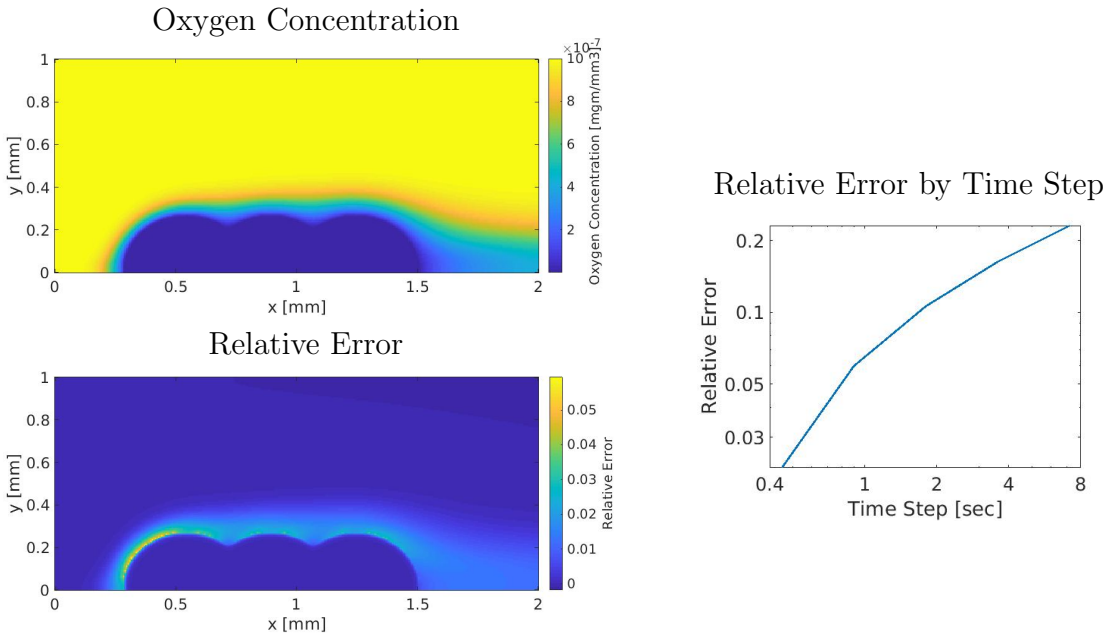

Figure 2.8. The top left plot shows the time-dependent solution of oxygen in a flow-cell for a 300×150 grid with a time step of 0.9 second. The bottom left plot shows the relative error, which is defined as the distance between the time-dependent solution and the quasi-stead-state solution relative to the inflow concentration. The right plot shows that the infinity norm error decreases as the time step decreases.

and time-dependent solutions allows us to model the novel, oscillatory phenomenon in *B. subtilis*, discussed in Chapter 4.

CHAPTER 3

A Dimensionally Reduced Model for Biofilm Growth

Adapted from [1] with permission from Springer Nature[1]

3.1. Introduction

Bacterial biofilms are colonies of bacteria attached to surfaces. They can be exploited in many beneficial ways such as in soil remediation, water filtration, and agriculture. Biofilms' presence can also be damaging to the host surface such as when biofilms foul machinery and infect humans and animals. Because of their critical importance in both enhancing as well as degrading human life, considerable effort is devoted to understanding, characterizing, and controlling them.

Biofilms are often studied experimentally using flow cells, which can take various forms such as linear or planar configurations as illustrated in Figure 3.1. While it is possible to image most of the surface area of the flow cell, typically only a small portion of the cell will be imaged in an experiment since a microscope can only image one small section at a time. For example, in [**4**] there are nine imaged regions each with a size of 0.375 mm by 0.375 mm out of the whole flow cell area 35 mm by 35 mm. These imaged regions together constitute less than 1% of the flow cell. Furthermore, the imaged regions are often located far from the inflow port due to the physical constraints imposed by the flow

[1]Adapted by permission from Springer Nature Customer Service Centre GmbH: Springer Nature Bulletin of Mathematical Biology, A Dimensionally Reduced Model of Biofilm Growth Within a Flow Cell, Noah Ford, David Chopp, Copyright 2020 Society for Mathematical Biology (2020) https://www.springer.com/journal/11538

cell and microscope structures. Estimating the local environmental conditions present at the point of observation is challenging because upstream bacteria consume substrates and produce waste and other byproducts that modify the conditions in the fluid as it moves from the inlet port to the observation point. The absence of accurate environmental data presents a challenge to understanding biofilm growth and quantitatively comparing observed growth to computational models.

It is theoretically possible to estimate local conditions by simulating the biofilm in the entire chamber using existing numerical methods, but this computation is expensive. The cost of simulating a small region containing a biofilm is large to begin with, and simulating the entire flow cell is prohibitive. In this chapter, we propose an alternative approach that uses asymptotic approximations to reduce the dimensionality of computing biofilm growth and the growth-limiting substrate concentration in the flow cell. We compare our results to those from existing numerical methods to demonstrate the utility of this approach in estimating the rate-limiting concentration of oxygen and subsequent biofilm growth. We also compare growth and outflow oxygen concentration to experimental data from [**4**] and [**7**]. These comparisons demonstrate that our reduced model can be used to estimate the environmental conditions inside the experimental flow cell at the location where experimental observations are made.

3.2. Derivation of One-Dimensional Model

Before introducing the asymptotic model, we will first consider a full continuum biofilm model upon which our simplified model is based. A full, multi-dimensional simulation involves tracking fluid flow, substrate outside and inside the biofilm, growth of the biofilm,

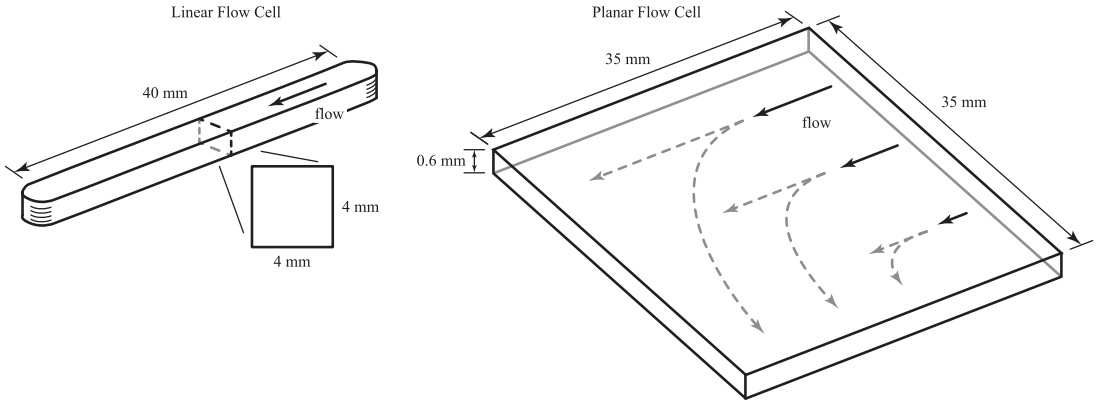

Figure 3.1. Illustration of typical flow cell configurations for biofilm experiments. (Left) Linear flow cell as described in [**3**]. (Right) Planar flow cell as described in [**4**]. Note that the outlet ports on the planar flow cell can be configured so that flow is straight through or turns the corner as indicated by the arrows, and a gradient in flow rate can also be created. Images using confocal microscopy from these flow cells are typically on the order of $250\mu m \times 250\mu m$ in the horizontal dimensions, in other words $< 1\%$ of the available surface area.

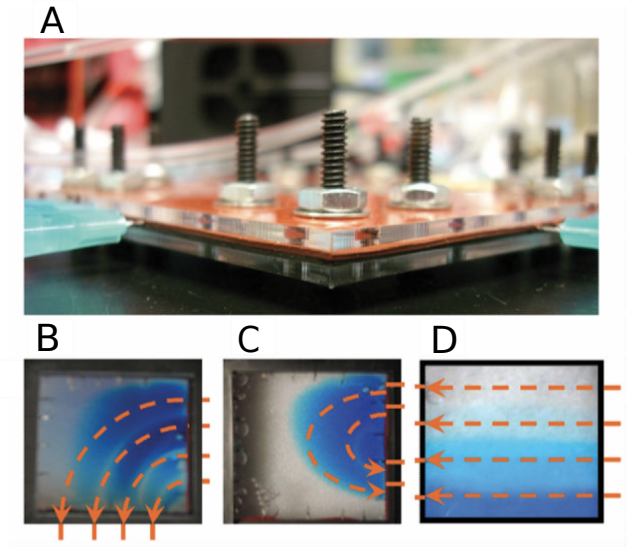

Figure 3.2. Flow cell developed in Aaron Packman's lab to create large variations in environmental conditions within a single experiment. Image reproduced from [**4**] with permission from Wiley Periodicals Inc (Copyright 2011 Wiley Periodicals, Inc.).

and the biofilm interface. Wanner and Gujer developed a general one-dimensional model for biofilms in [**35**], upon which most current models are based. For higher-dimensional models, the location of the biofilm/fluid interface must be tracked in a different manner than in the one-dimensional model. One common way to track the interface is through the Level Set Method introduced in [**48**], and developed further in [**50**], [**56**], and references therein. The Level Set Method was first used to track the interface of a biofilm in [**57**]. This method tracks and evolves the interface using the zero level set of the function ϕ. Let S_j be the j^{th} substrate with diffusion rate D_j and consumption rate η_j, U be the fluid velocity field, X_j be the j^{th} component of biomass, u be the biomass velocity, Φ be the biofilm growth potential function, F be the biomass growth velocity at the fluid/biofilm interface, n be the unit normal vector at the interface, and σ be detachment from sheer stress. By observing that the diffusion rate of substrate is much faster than the growth rate, we can assume substrate distribution does not depend on growth, which simplifies the equations by treating the substrate equations as quasi-steady state. The governing

equations are

Substrate Equations

$$D_j \nabla^2 S_j - \nabla(\vec{U} S_j) = 0 \qquad \text{Outside the biofilm} \tag{3.1}$$

$$D_j \nabla^2 S_j + \eta_j = 0 \qquad \text{Inside the biofilm} \tag{3.2}$$

Biomass Equations

$$\frac{\partial X_j}{\partial t} + \nabla \cdot (\vec{u} X_j) = \mu_j \tag{3.3}$$

$$\nabla^2 \Phi = \sum \mu_j \tag{3.4}$$

$$\vec{u} = \nabla \Phi \tag{3.5}$$

Boundary Growth Equations

$$\phi_t + F||\nabla \phi|| = 0 \tag{3.6}$$

$$F = \frac{\partial \Phi}{\partial n} + \sigma \tag{3.7}$$

$$\sigma = -F_{det} \tag{3.8}$$

Boundary Conditions

$$S_j = S_{j_{\text{Bulk}}} \qquad \text{At boundary with bulk fluid} \tag{3.9}$$

$$[S_j] = 0 \qquad \text{At top boundary of biofilm} \tag{3.10}$$

$$\left[D_j \frac{\partial S_j}{\partial n} \right] = 0 \qquad \text{At top boundary of biofilm} \tag{3.11}$$

$$\frac{\partial S_j}{\partial n} = 0 \qquad \text{At bottom boundary of biofilm} \tag{3.12}$$

These equations are represented visually in Figure 3.3. Substrate advects and diffuses through the fluid outside the biofilm. The substrate also diffuses into the biofilm where the bacteria consume it. The biomass uses the substrate to grow outward from the center. Growth, however, will be limited by the erosion rate, which depends on fluid velocity. The equations can track a rough and complex interface between the biofilm and the bulk flow and solve for the diffusive quantities in the resulting domain. However, the intricacies of the interface become less important when considering the biofilm from a large-scale perspective.

In considering the large-scale dynamics of the system, the first simplification we make is to view the biofilm as locally flat, and we assume substrate changes slowly in the upstream and downstream directions. This simplification allows us to model the substrate flux into the biofilm and its growth as a one-dimensional cross section. The presence of this one-dimensional cross section allows us to represent this dimension with a one-dimensional asymptotic expansion thereby reducing the computational complexity of the problem.

Table 3.1. Parameters Used in Reduced Model

Name	**Description**	**Value**	**Reference**
ρ_x	Biomass density	$1.0250\ \frac{\text{mg VS}}{\text{mm}^3}$	[**58**]
ρ_w	Inactive material density	$1.015\ \frac{\text{mg VS}}{\text{mm}^3}$	[**58**]
$Y_{x/o}$	Yield of active biomass due to substrate consumption	$0.583\ \frac{\text{mg VS}}{\text{mg O}_2}$	[**59**] and [**60**]
Continued on next page			

Table 3.1 – continued from previous page

Name	Description	Value	Reference
$Y_{w/o}$	Yield of EPS due to substrate consumption	$0.477\ \frac{\text{mg VS}}{\text{mg O}_2}$	[**59**] and [**60**]
$\hat{q}_o$	Maximum specific substrate utilization rate	$8\frac{\text{mg O}_2}{\text{mg VS day}}$	[**60**]
K_o	Half-maximum-rate concentration for utilization of substrate	$5 \times 10^{-}7\frac{\text{mg O}_2}{\text{mm}^3}$	[**60**]
d	Endogenous decay rate coefficient	0.3/day	[**60**]
D_o	Substrate diffusion coefficient in the biofilm	$146.88\frac{\text{mm}^2}{\text{day}}$	[**61**] and [**62**]
J_o	Substrate flux at biofilm surface	$10^3\frac{\text{mg O}_2}{\text{mm}^2\text{day}}$	Assumed
D_o^{fl}	Substrate diffusion coefficient in the fluid	$244.8\frac{\text{mm}^2}{\text{day}}$	[**61**] and [**62**]
f_D	Biodegradable fraction of biomass	0.8	[**60**]
γ	Chemical oxygen demand of VS	$1.42\frac{\text{mg O}_2}{\text{mm VS}}$	[**60**]
a_{det}	Shear stress multiplier	$0.1\text{mm}/(\text{N}/\text{m}^2)^{\text{b}}$	[**63**]
b_{det}	Shear stress exponent	0.58	[**63**]

3.2.1. One-Dimensional Model Definition

We begin with a one-dimensional biofilm model, following work from [**64**] and further developed in [**6**]. The authors assume that there are only two kinds of biomass in the

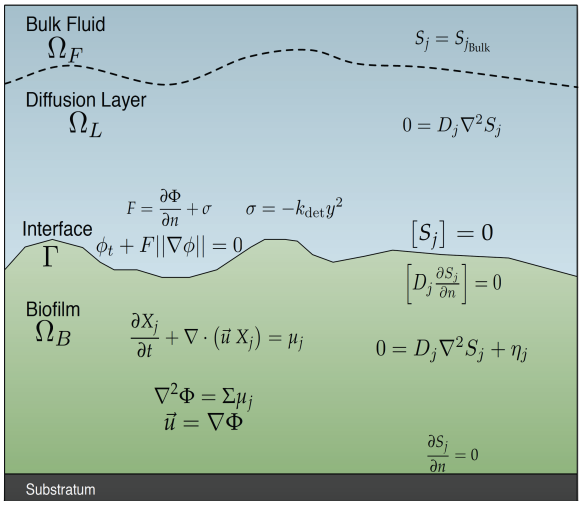

Figure 3.3. Visual representation of full simulation system of equations. Reproduced from [**5**] with permission for Elsevier Ltd. (Copyright 2009 Elsevier Ltd., https://www.sciencedirect.com/journal/journal-of-theoretical-biology)[2]

biofilm, active and inactive. Active biomass includes living cells that have the ability to replicate while inactive biomass is made up of dead cells and biological matter such as the extracellular matrix, which allows cells to attach to one another. The fraction of active biomass, f, evolves according to the equation

$$\frac{\partial f}{\partial t} = \mu_x f - \nabla(uf), \tag{3.13}$$

where $\mu_x \leq 1$ is a function of oxygen concentration and represents the fraction of active biomass created by the active cells, and the u term represents the biomass velocity that shifts f as the biofilm grows.

[2]Reprinted from Journal of Theoretical Biology, Volume 249 Issue 4, Brian V. Merkey, Bruce E. Rittmann, David L. Chopp, Modeling how soluble microbial products (SMP) support heterotrophic bacteria in autotroph-based biofilms, Page No. 3, Copyright (2009), with permission from Elsevier Ltd.

We also assume that in our case there is only one growth-limiting substrate in the system, which we assume to be dissolved oxygen in the fluid, but it could be a number of other diffusive substances. Oxygen is the limiting substrate for the experimental system to which we will compare. The demand for substrate, o, within the biofilm can be described with the equation $\eta_o = -\rho_x(\hat{q}_o + \gamma f_D d)\frac{o}{K_o+o}$. With this utilization term, the substrate equation is

$$D_o\nabla^2 o - \rho_x(\hat{q}_o + \gamma f_D d)\frac{o}{K_o + o} = 0, \tag{3.14}$$

where ρ_x is the biomass mass density, $\hat{q}_o$ is the maximum substrate utilization rate, γ is the chemical oxygen demand of the active biomass, f_D is the biodegradable fraction of active biomass, d is the endogenous decay rate, and K_o is the half-maximum-rate concentration for the utilization of substrate. The values for these and other parameters used in the model are given in Table 3.1. In this utilization-rate term, the $\hat{q}_o$ term represents growth while $\gamma f_D d$ represents maintenance of the inactive biomass.

To obtain a non-dimensionalized form, the authors in [**6**] use the rescaling technique introduced in [**35**] based on the variable $\zeta = z/L$, where z is the one-dimensional vertical direction, and L is the length of the biofilm so that $0 \leq \zeta \leq 1$ where $\zeta = 0$ at the base of the biofilm and $\zeta = 1$ at the fluid/biofilm interface. Since L is time dependent, the derivatives become

$$\frac{\partial}{\partial z} \to \frac{1}{L}\frac{\partial}{\partial \zeta}, \tag{3.15}$$

$$\frac{\partial}{\partial t} \to \frac{\partial}{\partial t} + \frac{\partial \zeta}{\partial t}\frac{\partial}{\partial \zeta} = \frac{\partial}{\partial t} - \frac{\zeta u(t,1)}{L}\frac{\partial}{\partial \zeta}, \tag{3.16}$$

where $u(t,1) = \frac{\partial L}{\partial t}$ is the velocity of the biofilm growth at the fluid/biofilm interface. Chopp et al. [**6**] non dimensionalize the length scale according to

$$L^* = L/\bar{L}, \quad \bar{L} = \left(\frac{K_o D_o}{\hat{q}_o \rho_x}\right)^{1/2}, \tag{3.17}$$

where D_o is the diffusion rate of oxygen in the biofilm. Similarly, to create nondimensionalized versions of t and o, the following conversions were used

$$t^* = t/\bar{t}, \quad \bar{t} = \frac{1}{Y_{x/o}\hat{q}_o - d}, \tag{3.18}$$

$$o^* = o/K_o, \tag{3.19}$$

where $Y_{x/o}$ is the yield of active biomass due to substrate consumption. In order for the scaling paramater $\bar{t}$ to be greater than zero, we have the constraint that $Y_{x/o}\hat{q}_o - d > 0$, which requires the biofilm to grow faster than it decays in the presence of sufficent oxygen. In the following equations, f is the active biomass fraction of total biomass, o^* nondimenionalized concentration, u^* nondimensionalized biomass velocity, and L^* nondimensionalized height.

Substrate Equation (3.20)

$$\frac{1}{L^{*2}}\frac{\partial^2 o^*}{\partial \zeta^2} = \tilde{B}\frac{o^*}{1+o^*}f,$$

Biomass Equations (3.21)

$$\frac{\partial f}{\partial t^*} = \frac{o^*}{1+o^*}f - \frac{1}{L^*}\frac{\partial u^*}{\partial \zeta}f + \frac{1}{L^*}(\zeta u^*(t^*,1) - u^*)\frac{\partial f}{\partial \zeta},$$

(3.22)

$$u^* = L^*\int_0^\zeta (1+W)\frac{o^*}{1+o^*}f\,d\zeta,$$

Boundary Growth Equation (3.23)

$$\frac{dL^*}{dt^*} = u^*(t,1) + \sigma,$$

where $\tilde{B} = 1 + \frac{\gamma f_D d}{\hat{q}_o}$, $W = \frac{\rho_w((1-f_D)d + Y_{w/o}\hat{q}_o)}{\rho_x(Y_{x/o}\hat{q}_o - d)}$, ρ_w is the inactive material density, and $Y_{w/o}$ is the yield of extracellular matrix due to substrate consumption. These equations have boundary conditions

$$\frac{\partial o^*}{\partial \zeta}(t^*, 1) = F_o L^*(o_M^* - o^*(t^*, 1)), \qquad \frac{\partial o^*}{\partial \zeta}(t^*, 0) = 0, \tag{3.24}$$

$$\frac{\partial f}{\partial t^*}(t^*, 0) = \frac{o^*}{1 + o^*} f(1 - (1 + W)f), \tag{3.25}$$

$$\frac{\partial f}{\partial t^*}(t^*, 1) = \frac{o^*}{1 + o^*} f(1 - (1 + W)f), \tag{3.26}$$

where the boundary condition for o^* at $\zeta = 1$ is a flux boundary with a boundary layer thickness defined by the constant $F_o = \bar{L}\frac{J_o}{D_o}$, and J_o is the substrate flux at the boundary. In this boundary equation o_M^* represents the maximum substrate concentration in the channel.

In the biofilms considered in [**6**], the fraction of active biomass to total biomass remains relatively constant for mature biofilms so they set f to be constant throughout the biomass. Solving for the steady-state volume-fraction of active biomass gives the following value for f:

$$\text{Biomass Equation} \qquad f \approx F = \frac{1}{1 + W}. \tag{3.27}$$

Using this constant mass fraction simplifies the substrate concentration equation, which becomes

$$\text{Substrate Equation} \qquad \epsilon \frac{\partial^2 o^*}{\partial \zeta^2} = \frac{o^*}{1 + o^*}, \tag{3.28}$$

where $\epsilon = 1/(FL^{*2}\tilde{B})$ with boundary conditions $\frac{\partial o^*}{\partial \zeta}(1) = L^* F_o(o_L^* - o^*(1))$ and $\frac{\partial o^*}{\partial \zeta}(0) = 0$. Through these simplifications, we now have an appropriate one-dimensional model that will allow us to solve for substrate flux into the biofilm and tie it directly to the biofilm growth asymptotically.

3.2.2. Asymptotic Substrate Profile

Though this new equation for substrate is quite simple, it does not have a closed-form solution. It is possible to solve the one-dimensional problem numerically, but this will be computationally expensive, particularly since we need to solve many one-dimensional problems simultaneously, as will be the case in a multidimensional flow cell. Instead, we will use an asymptotic representation proposed by [**6**] that takes advantage of the typically small boundary layer of nutrients for mature biofilms. We assume the depth of the biofilm is larger than the substrate penetration depth, and thus ϵ is small. The penetration thickness of a biofilm will remain constant once mature, as seen in Figure 3.4. This substrate penetration depth remains near $10 - 20\mu$m as found experimentally in [**65**].

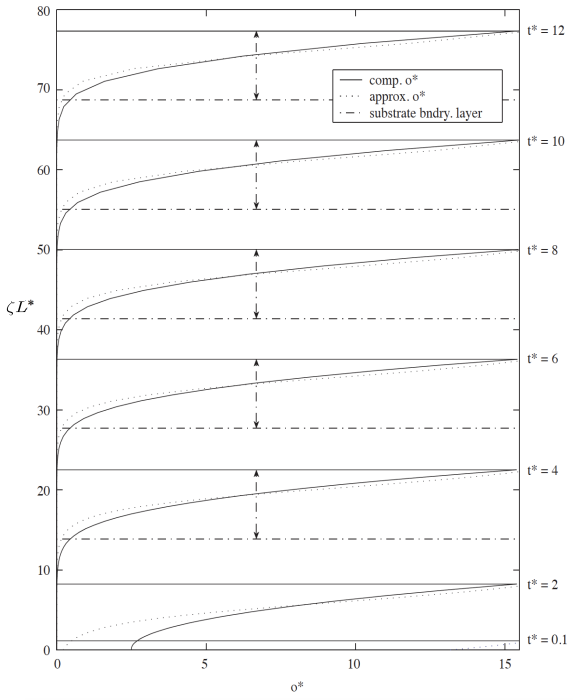

Figure 3.4. Asymptotic substrate profile of oxygen, o^*, at various biofilm thicknesses. Penetration depth remains constant once the biofilm has reached a critical thickness. Reproduced from [**6**] with permission from Springer Nature (Copyright 2003 Society for Mathematical Biology)[3]

The asymptotic profile provides the following equations for the interfacial concentration, concentration profile, flux into the biofilm, and change in length:

$$o^*_{int} \approx \frac{o^*_M - 3}{2} - \frac{3\sqrt{F\tilde{B}}}{2F_o} + \frac{1}{2}\sqrt{(o^*_M+3)^2 - \frac{6(o^*_M-3)\sqrt{F\tilde{B}}}{F_o} + \frac{9F\tilde{B}}{F_o^2}}, \tag{3.29}$$

$$o^*(\zeta) \approx o^*_{int}\frac{1+o^*_{int}/3}{1+(o^*_{int}/3)e^{(\zeta-1)/\sqrt{\epsilon}}}e^{(\zeta-1)/\sqrt{\epsilon}}, \tag{3.30}$$

$$F^*_{out} = -J^*_o(o^*_M - o^*_{int}), \tag{3.31}$$

$$\frac{dL^*}{dt^*} \approx (F\tilde{B})^{-1/2}\left(\frac{o^*_{int}+3}{o^*_{int}+4}\right)\ln((1+o^*_{int}/3)(1+o^*_{int})), \tag{3.32}$$

[3]Reprinted by permission from Springer Nature Customer Service Centre GmbH: Springer Nature Bulletin of Mathematical Biology, The dependence of quorum sensing on the depth of a growing biofilm, D.L. Chopp, M.J. Kirisits, B. Moran, M.R. Parsek, Copyright 2003 Society for Mathematical Biology (2003), https://www.springer.com/journal/11538

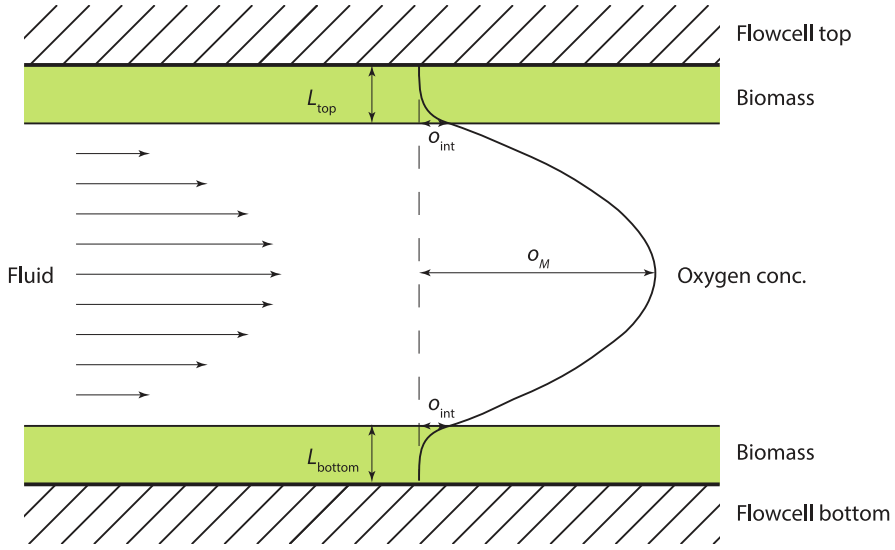

Figure 3.5. Illustration of parabolic flow and parabolic oxygen concentration with locations of o_M and o_{int} values

where o^*_{int} is the interface substrate concentration, o^*_M is the maximum substrate concentration in the channel, F_o is related to the diffusion rate, F is the fraction of active biomass, $J^*_o = J_o\bar{t}/\bar{L}$ is the nondimensionalized dispersal coefficient, and $\tilde{B}$ is related to the consumption rate. Equation (3.32) is derived in [**6**]. Since we are considering flow cells with biofilms growing on the top and bottom, we will adjust these asymptotic results to compute flux and growth using a parabolic instead of linear bulk substrate profile.

3.2.3. Calculating Flux and Growth using a Parabolic Bulk Substrate Profile

In this chapter, we expand on the model from [**6**] to allow for the presence of biofilms on both the top and bottom of a channel, and we use a parabolic profile for the substrate in the bulk flow as shown in Figure 3.5. The parabolic profile appears in flow cells such as the ones depicted in Figure 3.1 as a vertical slice at each point in the flow cell plane. The profile is consistent with substrate profiles seen in large-scale computations and with

lubrication theory, which we use to calculate flow, and the profile allows for substrate flux on both the top and bottom of the channel. The substrate profile has a maximum in the center of the channel and slopes down toward the biofilm interfaces on either side. Let ξ be the vertical coordinate in the channel, with $\xi = 0$ in the center of the channel. The substrate profile in the channel is

$$p(\xi) = -4(o_M^* - o_{int}^*)(\xi - B_w/2)(\xi + B_w/2)/B_w^2 + o_{int}^*, \tag{3.33}$$

where B_w is the width of the bulk flow. The maximum concentration, o_M^*, occurs in the middle of the flow channel at $\xi = 0$, and the minimum, o_{int}^*, occurs at the interface where $\xi = \pm B_w/2$. Assuming that we know o_{avg}^*, the average substrate concentration in the bulk fluid for a cross section, the parabolic profile assumption gives the following system of equations for substrate

$$o_{int}^* = \frac{o_M^* - 3}{2} - \frac{3\sqrt{F\tilde{B}}}{2F_o} + \frac{1}{2}\sqrt{(o_M^* + 3)^2 - \frac{6(o_M^* - 3)\sqrt{F\tilde{B}}}{F_o} + \frac{9F\tilde{B}}{F_o^2}}, \tag{3.34}$$

$$o_M^* = (3o_{avg}^* - o_{int}^*)/2. \tag{3.35}$$

Once we solve for o_{int}^* and o_M^*, we use these values and the boundary condition at the biofilm interface, $\partial o^*/\partial\zeta(1) = L^* F_o(o_M^* - o_{int}^*)$, to solve for the flux into the biofilm. Here F_o is redefined as $4D_o^{fl}/(D_o B_w/\bar{L})$ from the parabolic substrate assumption, D_o^{fl} is the diffusion rate of oxygen in the fluid and D_o is still the diffusion rate in the biofilm. Since flux out of the fluid is equal to $-D_o/L \times \partial o^*/\partial\zeta(1)$, the one-sided, nondimensionalized

flux out of the bulk is

$$F^*_{out} = -\frac{4D^{fl*}_o}{B^*_w}(o^*_M - o^*_{int}), \tag{3.36}$$

where $D^{fl*}_o = D^{fl}_o \bar{t}/\bar{L}^2$ is the nondimensionalized diffusion coefficent in the fluid, and $B^*_w = B_w/\bar{L}$ is the nondimensionalized channel width. The asymptotic growth is calculated as before using Equation (3.32).

As in Zhang et al. 2011 [**4**], we assume that fluid flow in the channel is parabolic with the maximum flow in the center and with a no-slip boundary condition at the biofilm interface. Under these conditions, stress, which we define as $\tau = \mu\frac{\partial u}{\partial \xi}$, where μ is viscosity and u is fluid flow, is calculated as

$$\tau = \frac{6\mu U_{avg}}{B_w}, \tag{3.37}$$

where U_{avg} is the average velocity above the biofilm and B_w is the width of the channel. This stress will erode bacteria at the surface of the biofilm. We calculate this erosion rate, dimensional and nondimensional, as

$$F_{det} = a_{det}\tau^{b_{det}}, \qquad F^*_{det} = F_{det}\frac{\bar{t}}{\bar{L}}, \tag{3.38}$$

where $b_{det} = 0.58$, and $a_{det} = 0.02$ and $a_{det} = 0.1$ for low and high growth limitation due to stress. These parameters are taken from [**63**] where they are fit to experimental data. This model for detachment is attractive because it is physically based on the shear stress that biofilms experience. Furthermore, the approximation has been used in the literature such as in [**66**]. However, its parameters can vary based on the experimental setup and

may need to be fitted to each biofilm system separately. In this chapter we use the original values from [**63**] unless otherwise specified. There are other detachment models that can be used such as a standard model where detachment is proportional to the square of the biofilm height, but these models are often less physically motivated than the shear stress model and are more difficult to use with the growth equation from this model.

Note that this stress-based erosion model does not include large-scale sloughing in which sections of the biofilm detach, which typically does not occur in slow flows and in the thin biofilms that we are discussing. For simplicity we also assume that the bacteria that detach do not reattach farther down the flow cell. This additional feature could be added to the model if desired. The asymptotic growth with shear detachment, which we label G_a, defines the growth of the biofilm length, L^*, for partially penetrated biofilm in the following equation

$$\frac{dL^*}{dt^*} = G_a = (F\tilde{B})^{-1/2}\left(\frac{o^*_{int}+3}{o^*_{int}+4}\right)\ln((1+o^*_{int}/3)(1+o^*_{int})) - F^*_{det}, \tag{3.39}$$

which is the same equation from [**6**] with an added detachment term. Using Equations (3.36) and (3.39), if we know o^*_{int} and o^*_M, we can solve for substrate flux and biofilm growth at that point for a partially penetrated biofilm. While these equations are accurate for most mature biofilms (biofilms that have grown for a day or so on the surface of interest), we want to expand our model to include thin and developing biofilms.

3.2.4. Approximating Growth and Flux for a Fully Penetrated Biofilm

The asymptotic substrate profile introduced by [**6**] and used in our analysis assumes that the substrate penetration layer in the biofilm is small compared to the biofilm depth.

We would like to extend the flux and growth calculations to a biofilm that is either newly developing or is limited in growth and is fully penetrated by the substrate. We approximate growth and flux in a thin biofilm as though the biofilm is fully penetrated with constant concentration, which simplifies the consumption and growth calculations. We set this constant concentration equal to the interfacial concentration. Because o^* is constant within the biofilm, our growth calculation becomes

$$\frac{dL^*}{dt^*} = L^* \int_0^1 \frac{1}{F} \frac{o^*}{1+o^*} f d\zeta \approx L^* \frac{o^*_{int}}{1+o^*_{int}}, \tag{3.40}$$

since $f \approx F$. Accounting for detachment due to shear stress gives the following growth equation for a fully penetrated biofilm, which we use to define the growth of the biofilm length, L^*, in our computation

$$\frac{dL^*}{dt^*} = G_p = L^* \frac{o^*_{int}}{1+o^*_{int}} - F^*_{det}, \tag{3.41}$$

where G_p is the estimate of growth of a fully penetrated biofilm. This expression will overestimate growth, but remains relatively accurate for a thin biofilm. We define the transition between the fully penetrated growth model and the partially penetrated growth model with a simple minimum function. Let

$$\text{Growth} = \frac{dL^*}{dt^*} = \min(G_p, G_a), \tag{3.42}$$

where G_a is the asymptotic growth approximation given in Equation (3.39). We do the same procedure for substrate flux into the biofilm, but since flux is negative (substrate is

leaving the fluid into the biofilm), we take the maximum.

$$\text{Flux} = \max\left(-\frac{4(D_o^{fl})^*}{B_w^*}(o_M^* - o_{int}^*), -FBL^*\frac{o_{int}^*}{1+o_{int}^*}\right), \tag{3.43}$$

where $B = \frac{\rho_x(\hat{q}_o+\gamma f_D d)}{K_o(Y_{x/o}\hat{q}_o - d)}$. Figure 3.6 shows the error in growth and flux from these approximations. The approximations overestimate the flux and growth near the transition between fully penetrated to partially penetrated, but otherwise reproduce the trend reasonably well. As shown in Figure 3.6, the biofilm typically passes through this transition point within a few hours in both experiments and in the model, so this larger transitional error will have a small affect on the overall computation. This approximation is similar to that in [**67**], but we use a lower-order approximation, which has a similar accuracy for this problem. Now that we have approximations for flux and growth at each longitudinal point in a partially and fully penetrated biofilm, we can use these equations to solve for the flux and the growth throughout a multi-dimensional flow cell.

3.3. The 1+1 Dimensional Model

In the $1 + 1$ Dimensional Model, we solve for substrate concentration in a two-dimensional domain using finite differences in the horizontal direction and using the asymptotic approximation in the vertical direction. Using this model, we solve for fluid flow, solute concentration, and biofilm growth in a two-dimensional channel with a biofilm growing on the top and the bottom of the channel. Figure 3.7 provides a visual representation of the setup for this system.

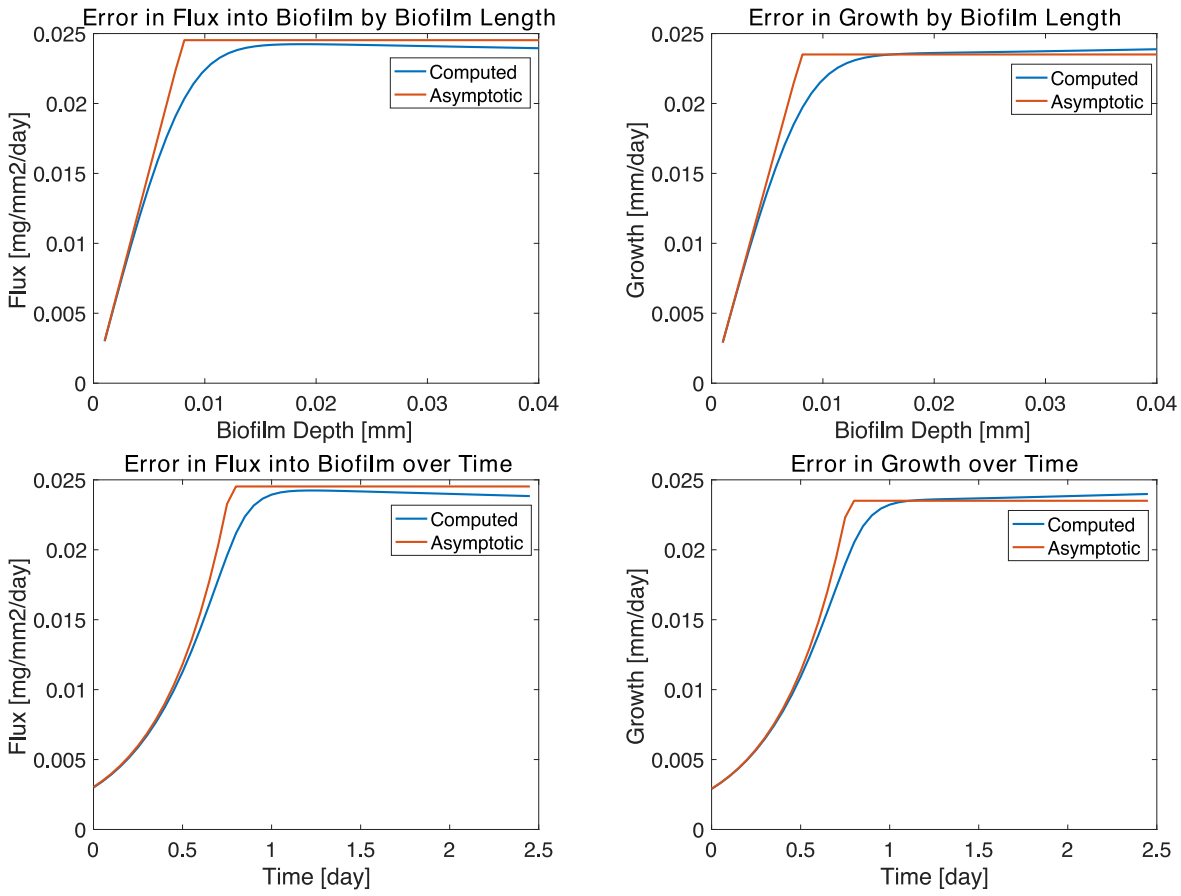

Figure 3.6. Asymptotic versus numerically computed flux and growth at various biofilm heights and at various times in growth. Calculations use an interfacial oxygen concentration of 1×10^{-6} mg/mm^3

We solve for fluid velocity using Lubrication Theory as detailed in [**68**], which provides the leading-order term of an asymptotic expansion calculating flow through a channel. This approximation is accurate when the channel's height is small compared to its longitudinal direction, which is true for most flow cells. With $\epsilon = H/L$ the ratio of

characteristic height to length, the zeroth order equations are the following

$$\frac{\partial u}{\partial x^*} + \frac{\partial v}{\partial \xi^*} = 0, \tag{3.44}$$

$$\frac{\partial^2 u}{\partial (\xi^*)^2} = \frac{\partial P}{\partial x^*}, \tag{3.45}$$

$$\frac{\partial P}{\partial \xi^*} = O(\epsilon^2), \tag{3.46}$$

where u is the zeroth order velocity term in the horizontal and scaled x^* direction, v is the zeroth order velocity term in the vertical and scaled ξ^* direction, and P is the zeroth order pressure term. Solving these equations gives

$$u = \frac{1}{2}\left(\frac{dP}{dx^*}(\xi^* + B_w^*/2)(\xi^* - B_w^*/2)\right), \tag{3.47}$$

$$v = \frac{1}{2}\frac{dP}{dx^*}\frac{dB_w^*}{dx^*}\left(\frac{(\xi^* + B_w^*/2)^2}{2}\right) - \frac{1}{2}\frac{d^2P}{d(x^*)^2}\left(\frac{(\xi^* + B_w^*/2)^3}{3} - \frac{(\xi^* + B_w^*/2)^2 B_w^*}{2}\right), \tag{3.48}$$

$$0 = \frac{d}{dx}\left((B_w^*)^3\frac{dP}{dx^*}\right). \tag{3.49}$$

In calculating the advection of the substrate within the fluid flow, we are primarily concerned with the horizontal, or x^*-directional, movement. The horizontal advection is much larger than the vertical, or ξ^*-directional, advection, which is essentially zero for laminar flow across a smooth surface. We simplify the equations above by ignoring vertical flow, v, and take the average of the horizontal flow, u, leading to the following equation

$$U_{avg}^* = -\frac{(B_w^*)^2}{12}\frac{dP^*}{dx^*}. \tag{3.50}$$

Equations (3.49) and (3.50) are the fluid equations for the $1+1$ Dimensional Model. In two-dimensions the lubrication theory approximation is equal to the fluid velocity calculated by conservation of mass.

Using this fluid velocity, we calculate substrate concentration at each vertical section of the flow cell. The parabolic profile assumption of substrate gives the following equation for average substrate in a column $o^*_{avg} = (2o^*_M + o^*_{int})/3$. The following set of equations represent solute concentration, biofilm growth, and flow in the flow cell.

$$(D_o^{fl})^* \frac{d}{dx^*}\left(B^*_w \frac{do^*_{avg}}{dx^*}\right) - \frac{d}{dx^*}\left(o^*_{avg} B^*_w U^*_{avg}\right) + 2F^*_{out} = 0 \tag{3.51}$$

$$o^*_{int} = \frac{o^*_M - 3}{2} - \frac{3\sqrt{F\tilde{B}}}{2F_o} + \frac{1}{2}\sqrt{(o^*_M+3)^2 - \frac{6(o^*_M-3)\sqrt{F\tilde{B}}}{F_o} + \frac{9F\tilde{B}}{F_o^2}}, \tag{3.52}$$

$$o^*_M = (3o^*_{avg} - o^*_{int})/2, \tag{3.53}$$

$$F^*_{out} = \max\left(-\frac{4(D_o^{fl})^*}{B^*_w}(o^*_M - o^*_{int}), -FBL^* \frac{o^*_{int}}{1+o^*_{int}}\right), \tag{3.54}$$

$$\frac{d}{dx^*}\left((B^*_w)^3 \frac{dP^*}{dx^*}\right) = 0, \quad U^*_{avg} = -\frac{(B^*_w)^2}{12}\frac{dP^*}{dx^*}, \tag{3.55}$$

$$\text{shear stress} = \tau = \frac{6\mu U^*_{avg}}{B^*_w \bar{t}}, \quad \text{detachment force} = F^*_{det} = a_{det}\tau^{b_{det}}\frac{\bar{t}}{\bar{L}}, \tag{3.56}$$

$$G_a = (F\tilde{B})^{-1/2}\left(\frac{o^*_{int}+3}{o^*_{int}+4}\right)\ln((1+o^*_{int}/3)(1+o^*_{int})) - F^*_{det}, \tag{3.57}$$

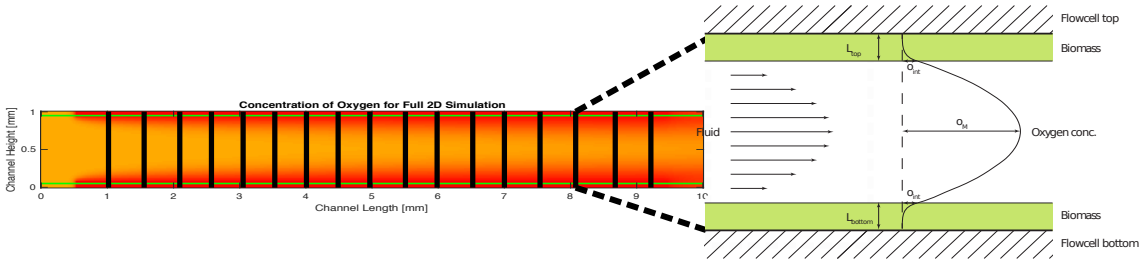

Figure 3.7. 1+1 Dimensional Model with asymptotic profile calculated in vertical direction

$$G_p = L^* \frac{o^*_{int}}{1 + o^*_{int}} - F^*_{det}, \tag{3.58}$$

$$\text{Growth} = \frac{dL^*}{dt^*} = \min(G_p, G_a), \tag{3.59}$$

where U^*_{avg} is the nondimensionalized mean velocity, and F^*_{out} is the flux of substrate out of the channel at the top and bottom. The boundary conditions for substrate are $o^*_{avg}(0) = C_I$ and $\partial o^*(0)_{avg}/\partial x^*(L^*_y) = 0$ where C_I is the inflow concentration and L^*_y is the length of the flow cell. The boundary conditions for pressure are $\frac{\partial P^*}{\partial x^*} = \frac{-12U^*_{in}}{(B^*_w)^2}$ at the inlet, and $P^*(L^*_y) = 0$ at the outlet. Since F^*_{out} is a function of o^*_M and o^*_{int}, which are only defined through $o^*_{avg}(x^*)$, we must iterate to solve for the substrate concentration. We use a successive over-relation (SOR) step in the iteration to solve this advection-diffusion equation.

3.3.1. SOR Iteration for Substrate Concentration

We must iterate to solve for substrate concentration. There are three concentrations that we must track: the maximum, the interfacial concentration (the minimum), and the average. It is only necessary to know two of the concentrations since the parabolic profile

determines the third, $o^*_{avg} = (2o^*_M + o^*_{int})/3$. We first initialize the maximum concentration to be the initial condition, and then loop over the following steps until convergence:

(1) Calculate the interfacial concentration using the maximum concentration:

$$o^*_{int} = \frac{o^*_M - 3}{2} - \frac{3\sqrt{F\tilde{B}}}{2F_o} + \frac{1}{2}\sqrt{(o^*_M + 3)^2 - \frac{6(o^*_M - 3)\sqrt{F\tilde{B}}}{F_o} + \frac{9F\tilde{B}}{F_o^2}} \tag{3.60}$$

(2) Calculate the flux into biofilm with maximum and interface concentrations:

$$F^*_{out} = \max\left(-\frac{4(D_o^{fl})^*}{B^*_w}(o^*_M - o^*_{int}), -FBL^*\frac{o^*_{int}}{1 + o^*_{int}}\right) \tag{3.61}$$

(3) Update the average substrate concentration, o^*_{avg} using an SOR method:

$$(D_o^{fl})^*\frac{d}{dx^*}\left(B^*_w\frac{do^*_{avg}}{dx^*}\right) - \frac{d}{dx^*}\left(o^*_{avg}B^*_wU^*_{avg}\right) + 2F^*_{out} = 0 \tag{3.62}$$

(4) Update the maximum concentration using the average concentration:

$$o^*_M = (3o^*_{avg} - o^*_{int})/2 \tag{3.63}$$

Since the flux equations depend nonlinearly on concentration, we choose a relaxation parameter $\omega < 1$ for the SOR step. However, for most problems, $\omega \approx 1$ exhibits fast convergence.

3.3.2. Validation

In [**6**], the one-dimensional, asymptotic concentration profile is compared to the computed profile and good agreement was found between the two profiles once the biofilm is mature enough to be only partially penetrated by the substrate. A linear boundary layer in the

fluid was used in the fluid for the comparisons. In this chapter, we validate the asymptotic profile with the parabolic substrate concentration in the bulk flow. We compare the asymptotic profile of a two-sided biofilm (top and bottom of the channel) to cross sections of concentration from the full two-dimensional simulation based on the method developed in [**5**]. This two-dimensional model is a continuum model based on the Wanner-Gujer model from Section 3.2. This model solves for fluid flow in the channel, advection and diffusion of the substrates, and tracks biomass growth using a level-set method. Figure 3.8 shows the full channel distribution of the substrate concentration for a flow cell (1 mm width and 10 mm length) using both models. Both models were initialized with a constant height of biofilm for all points. The distribution of substrates match poorly near the inflow of the channel because the substrate in the full two-dimensional simulation has not yet developed the parabolic profile. However, as the fluid moves farther into the flow cell, the substrate profile in the flow quickly resembles the parabolic profile. Despite this mismatch in distribution near the inlet of the flow cell, the asymptotic model matches the average concentration value at each cross section quite well. Though the asymptotic model assumes that the biofilm surface is locally flat and cannot capture the small-scale detail of the biofilm interface, it can also be used to model biofilms that have surfaces with large-scale variation, as shown in Figure 3.9. We initialize the biofilm's surface to be constant within sections that are 1 mm in length with a variation in height of .025 mm between sections. In addition to the error near the inlet, there are smaller errors near the edges of the bumps, but the overall substrate distribution still matches well.

We further compare the one-dimensional profiles in Figure 3.10. This figure represents a comparison between an asymptotic substrate profile in the biofilm, a numerically

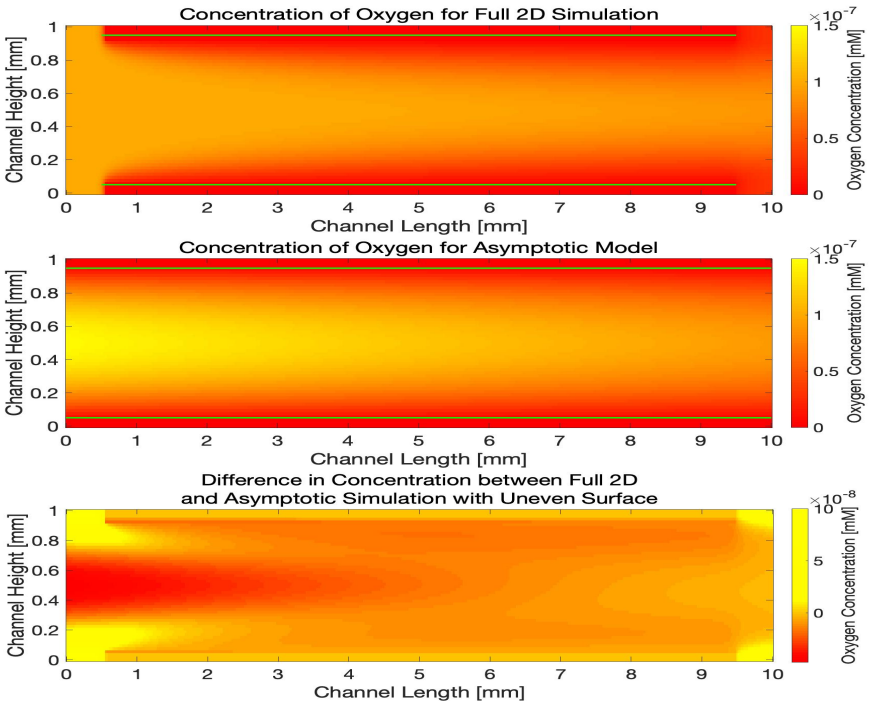

Figure 3.8. Comparison of substrate distribution of full 2D simulation to asymptotic model. The green lines in the image represent the location of the biofilms, which has a height of .05mm on the top and bottom of the channel. The full 2D simulation does not have biomass in the 0.5mm section next to the inlet and outlet.

computed, one-dimensional profile within the biofilm with a parabolic substrate profile in bulk, and a cross section from the full two-dimensional model for a channel of width 0.1mm. This small channel size was chosen for viewing purposes because the substrate profile within the biofilm is quite shallow. The three profiles have similar shapes with comparable fluxes and growth rates.

Since the shapes of the profiles look qualitatively similar, we quantitatively compare the flux and growth from the asymptotic flow cell to the full two-dimensional biofilm model. In the comparison, we consider a flow cell with a height of 0.6mm, which is a common height for flow cells. We find good agreement between our asymptotic model and

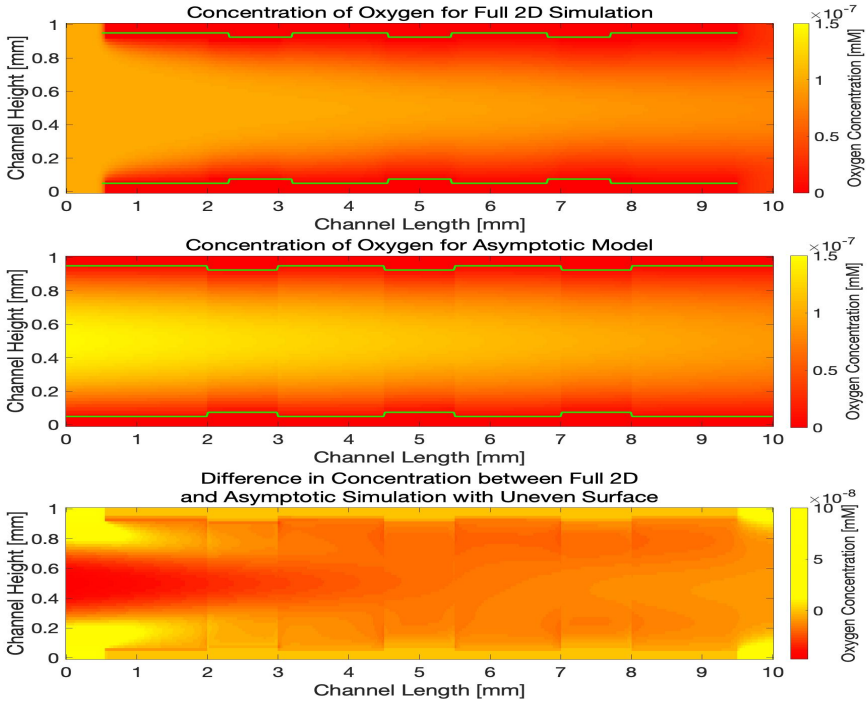

Figure 3.9. Comparison of substrate distribution of full 2D simulation to asymptotic model with uneven biofilm surface. This surface is piecewise constant in 1mm-wide regions. The protruding regions are 50% larger than the surrounding regions of height .05mm. The green lines in the image represent the location of the biofilms. The full 2D simulation does not have biomass in the 0.5mm section next to the inlet and outlet.

the two-dimensional model for substrate flux, biofilm growth, and interfacial concentration at low substrate concentrations as shown in Figure 3.11.

For high concentrations, the flux and growth in the asymptotic model begin to deviate from the full two-dimensional model. However, the error at these concentrations is minimally important because these concentrations are far above the saturation level of oxygen in water at 20 degrees Celsius at sea level, which is approximately 9mg/L. We find that the $1+1$ Dimensional Model predicts growth and flux with similar accuracy to the full, two-dimensional simulation while running orders of magnitude faster.

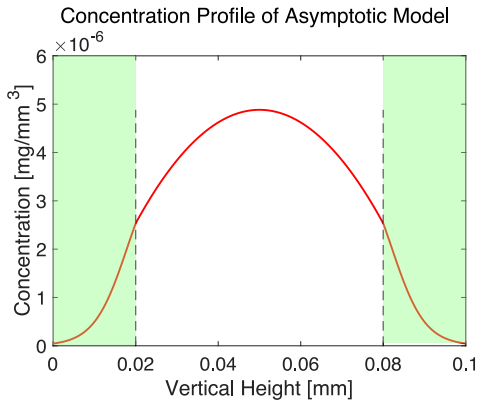

Asymptotic profile. Growth is 0.0381 mm/day and flux into the biofilm is 0.0368 mg/mm^2/day.

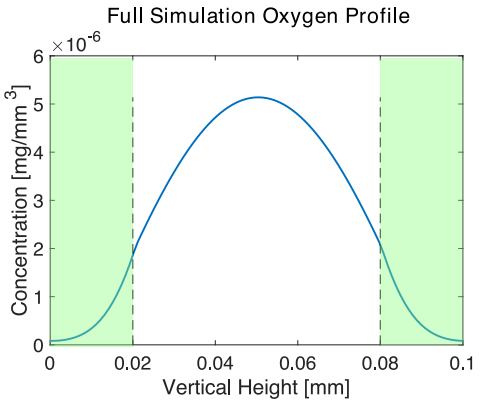

Profile from full 2D simulation. Growth is 0.0285 mm/day and flux into the biofilm is 0.0335 mg/mm^2/day.

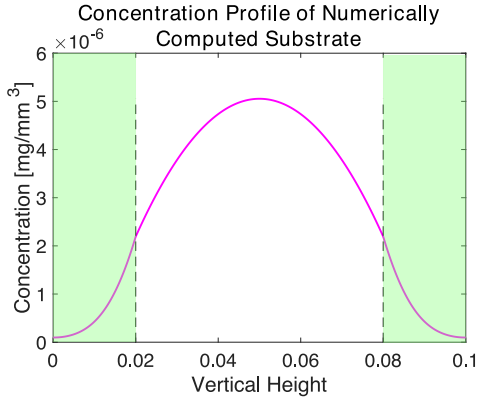

Computed biofilm profile with parabolic bulk concentration profile. Growth is 0.0357 mm/day and flux into the biofilm is 0.0367 mg/mm^2/day.

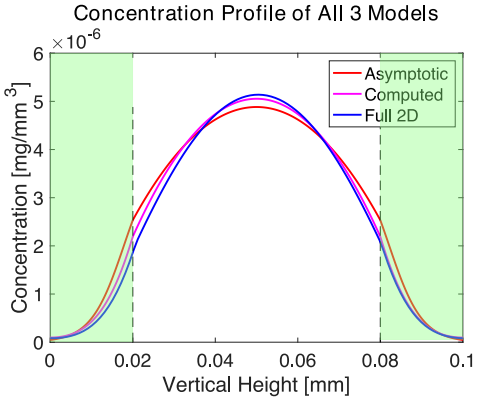

Comparison of the three concentration profiles.

Figure 3.10. Computed and asymptotic concentration profiles compared to cross section of a full 2D simulation for mean substrate concentration 3.47×10^{-6} mg/mm^3 in bulk channel. The biofilm height is set to .02mm at the top and bottom of channel in all three simulations. The computed concentration profile has an error of 2.07×10^{-6} mg/mm^3 and of 1.08×10^{-6} mg/mm^3 in L^∞ and L^2 respectively compared to full 2D cross section. The asymptotic profile has an error of 2.26×10^{-6} mg/mm^3 and of 1.18×10^{-6} mg/mm^3 in L^∞ and L^2 respectively compared to full 2D cross section.

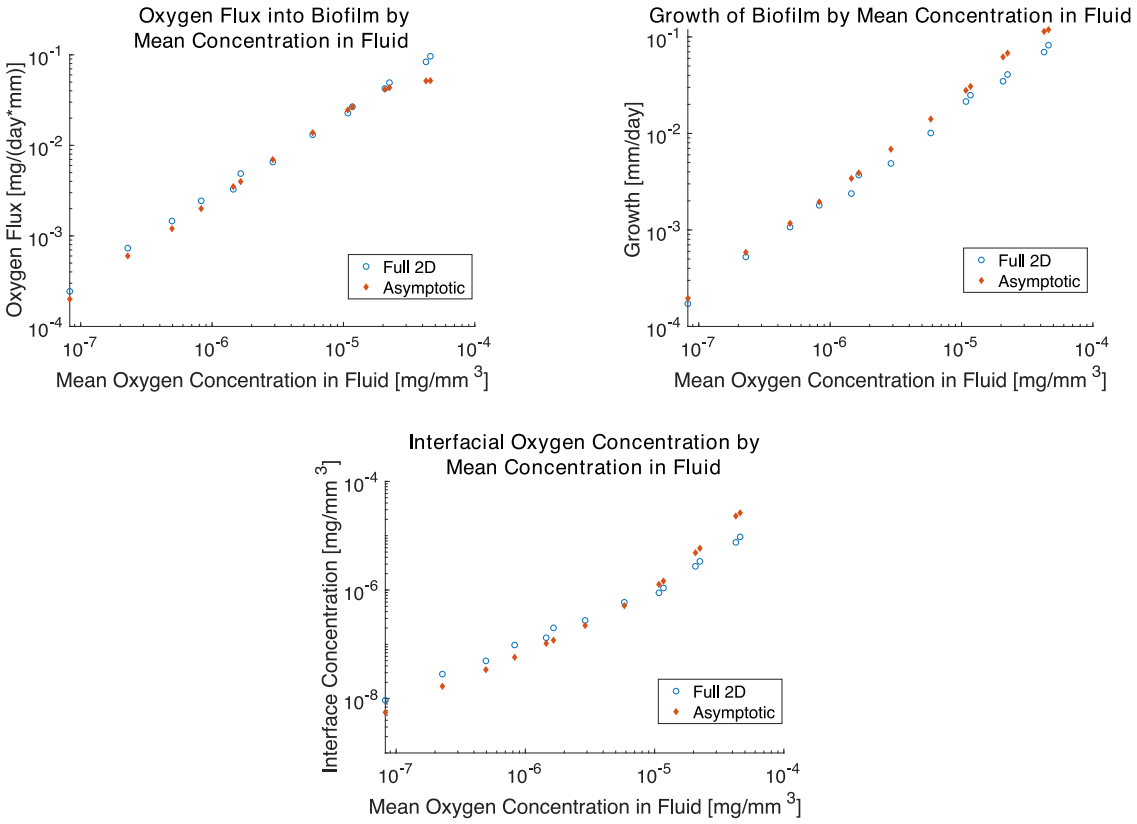

Figure 3.11. Comparison of flux, growth, and interfacial concentration between asymptotic simulation and full two-dimensional simulation for varying mean oxygen concentrations within the channel cross section

As previously discussed, the main benefit of the asymptotic model is that it runs much faster than the full two-dimensional simulation, and we show this comparison in Figure 3.12. For the simulation conditions tested the asymptotic model runs about 100 times faster. This speed difference is most noticeable for highly resolved computations because the asymptotic model's run time is proportional to the number of x grid points while the full two-dimensional model's run time scales more closely with the square of the number of x grid points. An additional benefit is that the asymptotic solver is computationally much simpler. The full two-dimensional model uses the Intel MKL Pardiso sparse matrix

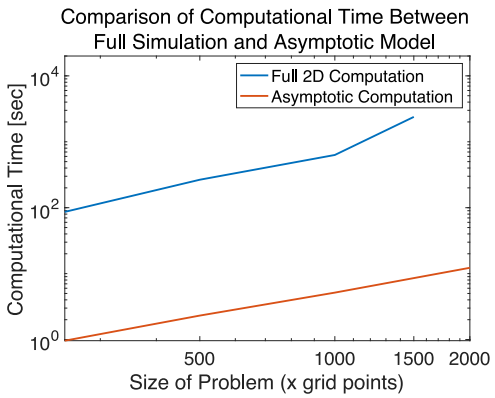

Figure 3.12. Comparison of computation times for full two-dimensional system and asymptotic model. The size of the computation follows the number of x grid points. For the full simulation the number of y grid points scales with the number of grid points in the x direction. The machine's CPU is an Intel Xeon E5-2667v3. The GPU is an NVIDIA Tesla K20c.

solver [**69, 70, 71**], a parallelized fluid solver that runs on a GPU, and a complex level-set library to track the biofilm-fluid interface. In comparison, the asymptotic simulation consists of just a few hundred lines of code and the Pardiso matrix solver. Even with the high-performance fluid solver, the full model runs much slower than the asymptotic model.

3.4. The 2+1 Dimensional Model

The $2+1$ Dimensional Model is designed to simulate three-dimensional flow through a planar flow cell by solving the substrate equation using finite differences in two longitudinal dimensions and using the asymptotic approximation in the vertical dimension. This setup is shown visually in Figure 3.13. The $2+1$ Dimensional Model equations are

$$(D_o^{fl})^* \nabla \left(B_w^* \nabla o_{avg}^* \right) - \nabla \cdot (o_{avg}^* B_w^* \langle U_{avg}^*, V_{avg}^* \rangle) + 2F_{out}^* = 0, \tag{3.64}$$

$$\frac{\partial}{\partial x^*}\left((B_w^*)^3\frac{\partial P^*}{\partial x^*}\right)+\frac{\partial}{\partial y^*}\left((B_w^*)^3\frac{\partial P^*}{\partial y^*}\right)=0, \tag{3.65}$$

$$U_{avg}^*=-\frac{(B_w^*)^2}{12}\frac{\partial P^*}{\partial x^*},\quad V_{avg}^*=-\frac{(B_w^*)^2}{12}\frac{\partial P^*}{\partial y^*}, \tag{3.66}$$

$$\text{shear stress}=\tau=\frac{6\mu\sqrt{(U^*)_{avg}^2+(V^*)_{avg}^2}}{B_w^*\bar{t}},$$

$$\text{detachment force}=F_{det}^*=a_{det}\tau^{b_{det}}\frac{\bar{t}}{\bar{L}}, \tag{3.67}$$

with equations for oxygen concentration, flux, and biofilm growth the same as in the $1+1$ Dimensional Model, Equations (3.52, 3.53, 3.54, 3.57, 3.58, 3.59). For the substrate equations, we use the boundary condition, $o_{avg}^*=C_I$ where C_I is the inflow oxygen concentration at the inlet and the boundary condition $\frac{\partial o_{avg}^*}{\partial n}=0$, at outlets and at the interior walls of the flow cell. For pressure, we let $\frac{\partial P^*}{\partial n}=\frac{-12U_{in}^*}{(B_w^*)^2}$ at the inlet, $P^*=0$ at the outlet, and $\frac{\partial P^*}{\partial n}=0$ at the interior walls. We solve the equations using the same SOR method described in the $1+1$ Dimensional Model, Equations (3.60, 3.61, 3.62, 3.63), but now we use a two-dimensional grid.

3.4.1. Validation

We compare our results to the turning flow cell experiment designed by Zhang et al. [**4**] from Figure 3.2. The cell is 35 mm by 35 mm with a thickness of 0.6 mm and has a turning flow that is designed to exhibit a large variety of flow speeds and substrate concentrations within a single experiment. The flow arcs from the inlets on the right side to the outlets at bottom of the image. We initialized the biofilm to be a constant height throughout the

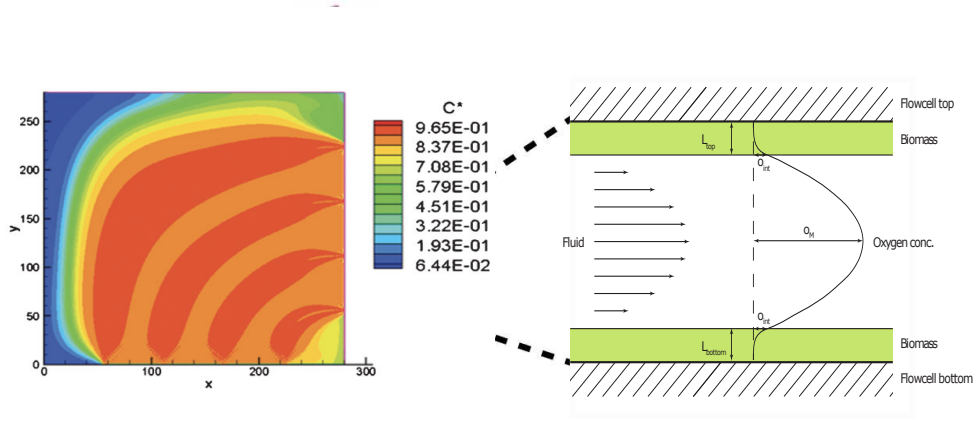

Figure 3.13. 2+1 Dimensional Model with asymptotic profile calculated in vertical direction. Flow cell image reproduced from [**4**] with permission from Wiley Periodicals Inc. (Copyright 2011 Wiley Periodicals, Inc.)

flow cell and simulate the flow cell for seven days. Computed concentration and biomass quantity are plotted for low flow (0.16 ml/min) in Figure 3.14. Growth occurs mainly near the inlet since the biofilm consumes most of the substrate before the flow reaches the middle. Concentration and biomass quantity are plotted for high flow (0.8 ml/min) in Figure 3.15. The growth mainly occurs in quiescent regions of the cell like in the region far from the inflow and outlet and in the spaces between the inlets and between the outlets. This variation in biomass between the inlet and the points of observation is precisely why this model is needed.

We would ideally validate our model by comparing the oxygen concentrations between the experiment and the simulation. However, we do not have access to oxygen concentrations in the interior of experimental flow cells, which is why we developed this model to estimate these quantities. Without oxygen concentration data, we compare regional biomass growth between the experiment and the simulations as a proxy. We fit our model

to six data points from [**4**] by hand using a flat biofilm as the initial conditions. At the seven-day mark, we find that the simulation reproduces the same trend in growth as the experiment. In Figure 3.16 we see low growth in regions that experience low fluid velocity because oxygen, the growth-limiting nutrient in the system, flows too slowly from the inlet to reach the region. Regions that experience high speeds also have low growth because they experience high shear stress. The highest biomass growth occurs in regions that experience moderate speeds so that the bacteria receive enough nutrients without experiencing high levels of shear stress. The estimated flow speeds are lower than the estimates from [**4**] which may be due to the difference in estimation techniques since the experiment did not measure flow speed directly. These computed results are sensitive to the growth rate, shear rate, and initial conditions, and the parameters must be fitted to individual experiments. We initialize a bumpy biofilm surface and show the resulting biofilm height on the seventh day in Figure 3.17. Though after seven days the biofilm has more biomass in regions that began with more biomass, the variation decreases in relative size with time to converge to a similar spatial pattern as the biofilm from the simulations with constant initial biofilm height.

We also compare oxygen concentration seen experimentally in the outflow of the linear flow cell in [**7**] to the concentration predicted by our model. The authors measure oxygen concentration in the outflow of a flow cell that is 35mm long by 4mm wide by 1mm high. In the simulation, we find that the outflow concentrations change similarly with time. The decrease in outflow concentration begins slowly as the bacteria form a thin covering of the flow-cell walls as plotted in Figure 3.18. As the biofilm becomes thicker, the growth rate and the change in consumption increase. As a result, the concentration decreases at an

accelerated pace until most of the biofilm is partially penetrated leading to an asymptote in outflow oxygen concentration. The simulations for all three growth rates, $\hat{q} = 8, 16, 32$, reach a similar asymptote, as shown in Figure 3.18. However, the experimental outflow concentration is lower than the concentration seen in the simulation. One reason that the model underestimates the biofilm's oxygen consumption is that the parabolic substrate profile underestimates the flux near the inlet before the profile relaxes to parabolic. A second reason for the underestimation of consumption is that the model assumes that only bacteria on the top and the bottom of the flow cell consume oxygen and does not account for the consumption by bacteria on the side walls. For certain flow cells, such as the linear flow cell from Figure 3.1, these side walls can make up a large proportion of the total surface area of the flow cell. A final contributing factor to the underestimated consumption is that the asymptotic model does not account for the presence of detached bacteria in the bulk flow. In the experimental flow cell, detached bacteria will enter the bulk flow and consume some of the oxygen in the fluid. While there are some discrepancies between the asymptotic model and experimental results, the $2 + 1$ Dimensional Model does a good job of capturing the trend in the data.

The computational cost of the $2 + 1$ Dimensional Model is quite reasonable as shown in Figure 3.19. Because of the complexity of implementation, we do not have a fully-resolved, three-dimensional biofilm model to which we can compare these run times. We can estimate the computational time by multiplying the two-dimensional computational time by the number of points in the added third dimension. With an x grid size of 250, the full two-dimensional model has a run time of 86 seconds. Multiplying by the added 250 grid points in the added direction, the full three-dimensional run time could be near

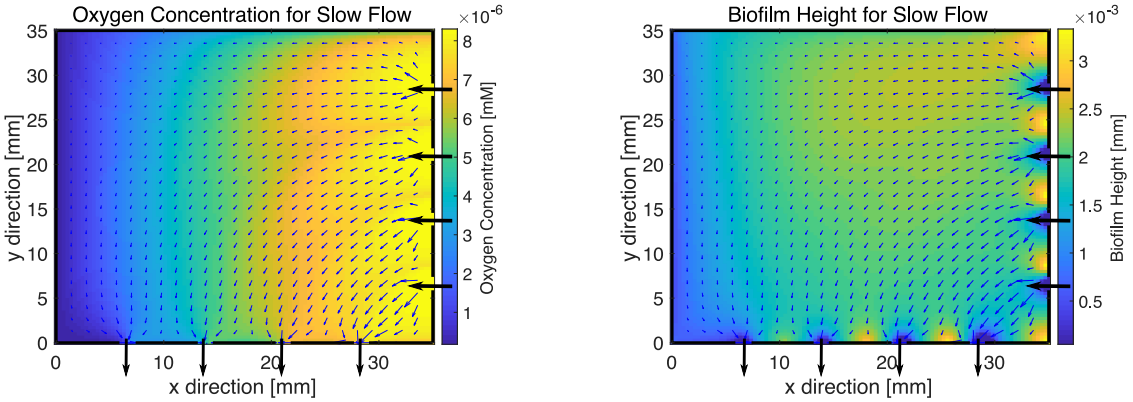

Figure 3.14. Concentration and growth after seven days in turning flow cell with flow of .16 ml/min (slow flow)

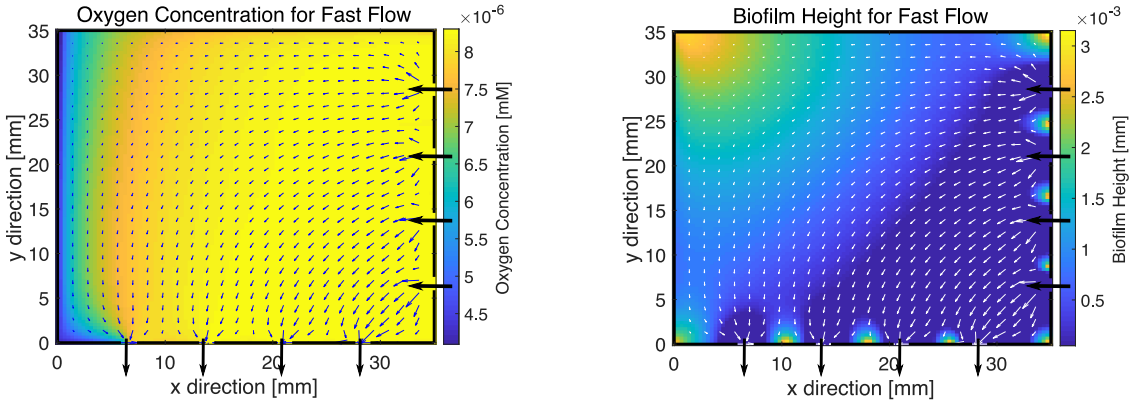

Figure 3.15. Concentration and growth after seven days in turning flow cell with flow of .8 ml/min (fast flow)

21,500 seconds, or about 6 hours, compared to the $2+1$ Dimensional Model's run time of 70 seconds. Even if researchers have easy access to a full three-dimensional model, they may still prefer to run the asymptotic model because of its comparative speed.

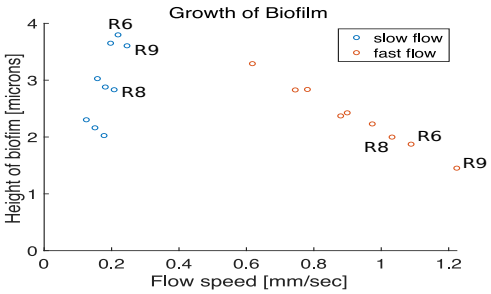

Simulated biofilm height

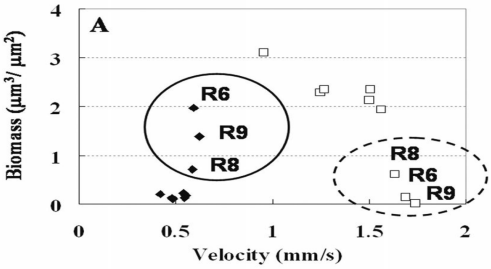

Experimental biofilm height

Figure 3.16. Speed and growth comparison after seven days between simulated and experimental data. Growth rate and detachment strength were fit by hand to data points labeled R6, R8, and R9 for both slow flow and fast flow producing the values $\hat{q} = 2.15$ and $a_{det} = .07$ with an L^2 error of 1.8 μm. Experimental data is given as regional biomass per surface area, which is equivalent to average height for the region. The filled diamonds in experimental data represent measurements from low flow conditions. The empty squares represent data from high flow conditions. R6, R8, and R9 are measurements are taken from the lower right region of the flow cell. Experimental biofilm height is reproduced from [**4**] with permission from Wiley Periodicals Inc. (Copyright 2011 Wiley Periodicals, Inc.)

3.5. Outward Growth

To this point, we have assumed that growth only occurs upward. In particular, if a grid point begins with no biofilm height, there is no way for it to transition to containing biomass even if it is next to a grid point that has a nonzero biofilm height. We address this outward growth and lateral movement of biofilm by adjusting the growth calculation. First, we calculate normal-directional growth for a fully penetrated biofilm using an updated height. Instead of using the biofilm's vertical height to calculate growth, we use the depth of the biofilm in the direction orthogonal to the surface,

$$G_p = \max\left(L^*\sqrt{1+||\nabla L^*||^2}\frac{o^*_{int}}{1+o^*_{int}} - F^*_{det}, 0\right), \tag{3.68}$$

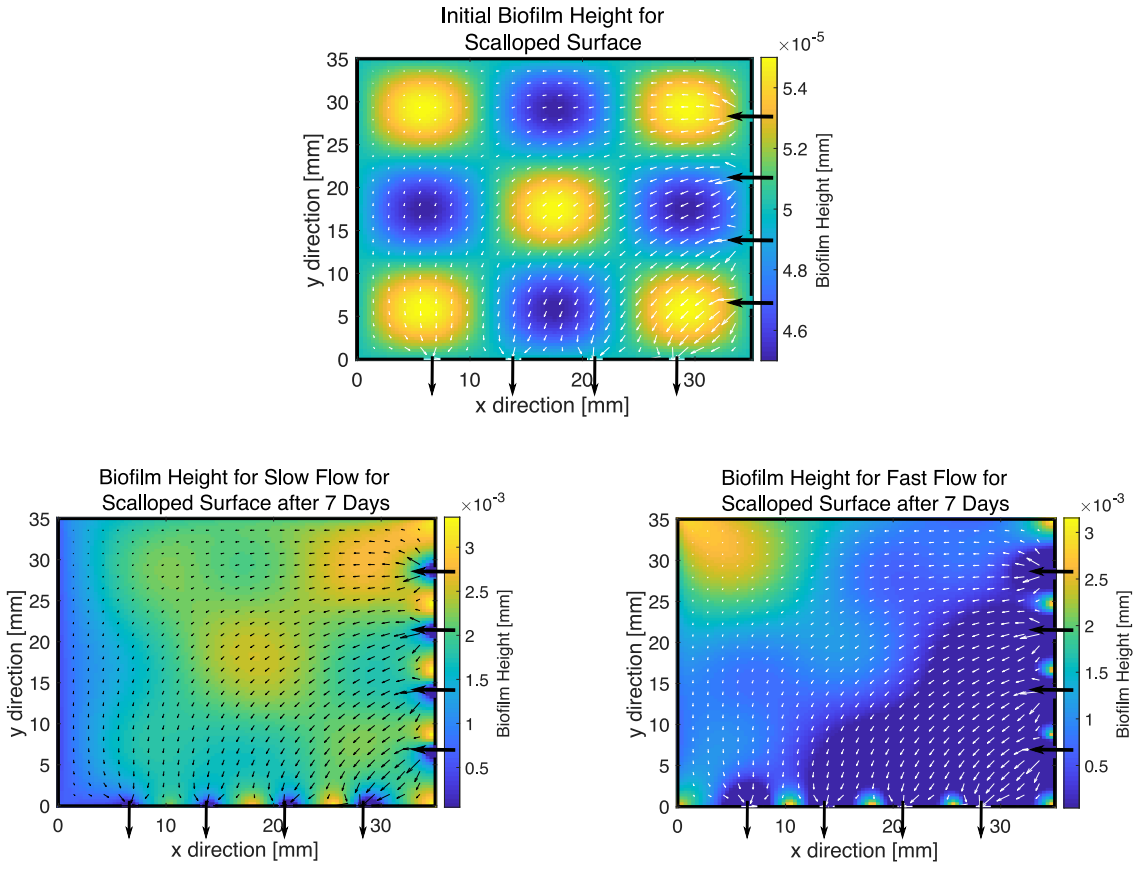

Figure 3.17. Biofilm height calculation for turning flow with scalloped initial conditions.

where $\sqrt{1+||\nabla L^*||^2}$ adjusts the growth speed to reflect the slope of the biofilm. We do not need to adjust the growth for the asymptotic growth calculation because this calculation does not depend on biofilm height. Now that we have the normal-directional growth of the biofilm, we use the factor $\sqrt{1+||\nabla L^*||^2}$ to transform orthogonal growth to vertical growth at each grid point,

$$L^*_{t+1} = L^*_t + G\sqrt{1+||\nabla L^*||^2} \times dt, \tag{3.69}$$

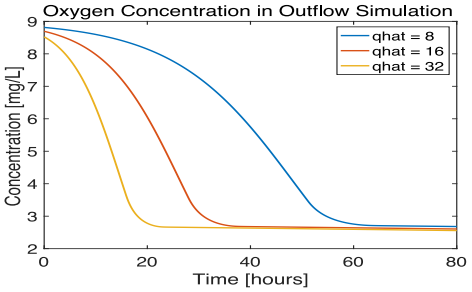

Simulated outflow concentration

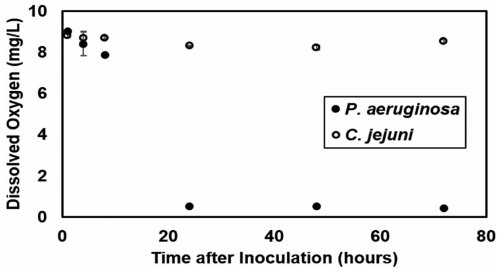

Experimental outflow concentration

Figure 3.18. Outflow oxygen concentration comparison between simulated and experimental data. The experimental data we consider are the points for *P. aeruginosa*. The L^2 error between the model and data for growth rate $\hat{q} = 8$ is 3.4 mg/L. The error for $\hat{q} = 16$ is 2.1 mg/L. The error for $\hat{q} = 32$ is 1.5 mg/L. Experimental outflow concentration is reproduced from [**7**] with permission from Oxford University Press. (Copyright FEMS 2015)[4]

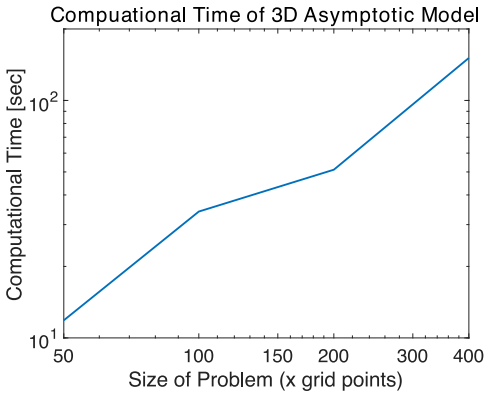

Figure 3.19. Plot of computational time for asymptotic three-dimensional model. The computations were performed over a square grid.

where $G = \max(G_a, G_p)$ as before. These geometric adjustments are shown for the two-dimensional case in Figure 3.20.

[4]Alessandro Culotti, Aaron I. Packman, Pseudomonas aeruginosa facilitates Campylobacter jejuni growth in biofilms under oxic flow conditions, FEMS Microbiology Ecology, 2015 Volume 91, Issue 12, page 6, by permission of Oxford University Press, Copyright FEMS 2015

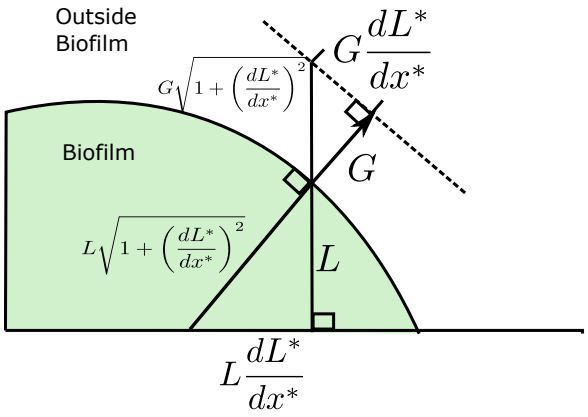

Figure 3.20. Outward growth adjustments of 2D biofilm

To allow the biofilm to grow horizontally, we linearly extrapolate the height of the biofilm to regions without biomass (in which the extrapolated height will be negative). We use linear extrapolation to ensure the edge of the biofilm grows horizontally at the rate of $G\sqrt{1+1/||\nabla L^*||^2}$. When we update the biofilm height within the region that already has biomass, we also grow the biofilm height in the regions of "negative" biofilm height using the growth speed from its nearest neighbor with biomass. This procedure allows for outward biofilm growth and the spread of biomass to new regions. It also allows for two non-connected colonies to grow together.

For the 1+1 Dimensional Model, the process of linear extrapolation is simple. However, the bilinear extrapolation required by the $2+1$ Model is more complicated since the biofilm's slope varies along its edge. We solve this problem by using a method developed in [**72**] to extend surfaces when the rate of extension, defined here by the slope of the biofilm at its edge, changes along the interface. However, this extension can become unstable the farther one extrapolates from the biofilm's edge. In this simulation, we only extrapolate to grid points that are directly adjacent to the region with biomass, which

limits the outward growth of the biofilm possible in one time step to less than two times the spacing between adjacent grid points.

In Figure 3.21 we show the outward growth of a small semicircle of biofilm in a flow cell of height 0.5 mm. The biofilm then grows outward and preferentially toward the inlet. We see the creation of fins in the downstream direction, which represent regions of the flow cell that experience a higher substrate concentration than the region that is directly downstream from the biomass. This low-growth zone on the downstream side of the biomass appears in other biofilm models such as in [**73**]. The outward growth toward regions of higher substrate concentration demonstrates our model's more realistic representation of biofilm growth compared to having solely upward growth.

This growth calculation also allows for colonies to combine and for biomass to spread to regions of high shear within the turning flow cell studied in Section 3.4.1. First, we show that isolated biofilm colonies can merge into a single mass in Figure 3.22, which is another property of biofilms seen in experiments. Second, we show that including outward growth increases biofilm growth near the inlets and outlets of the flow cell from Figure 3.15 for both the biofilm initialized to be flat and the biofilm initialized to be scalloped. The difference between the biofilm height in the model with outward growth and the model with no outward growth is shown in Figure 3.23. The biofilm spreads from the quiescent regions between the inlets and outlets toward areas closer the openings that experience higher stress. This spreading to parts of the flow cell with high nutrient concentrations and high shear stress is sometimes seen in experiments when biomass clogs the inlet ports. We do not see much difference in biofilm height within the center of the flow cell because the slope of the surface of the biofilm is relatively small. The smooth surface does not

encourage much spreading. This spreading of biomass from regions with higher quantities of biomass suggests that this updated model could be more realistic.

3.6. Discussion and Conclusion

In this chapter we developed a fast model of large-scale dynamics in biofilm flow cells using a one-dimensional asymptotic profile. We created a $1 + 1$ Dimensional Model to simulate two-dimensional dynamics and a $2 + 1$ Dimensional Model to simulate three-dimensional dynamics. The simulations have similar accuracy to the high-resolution, non-simplified models for large-scale behavior. We also showed that the predictions from the simulations agree qualitatively with experiments in both the growth speed and the substrate concentration.

The largest benefit of this model compared to prior methods is that it is computationally much simpler. Because of its simplicity, it runs orders of magnitude faster than other methods. Also, the model non-dimensionalizes the equations which hides much of the parametric complexity from the experimentalists. Most variation in behavior of the model can be controlled by the parameters of growth rate, erosion rate, and initial biofilm height, which allows users to better conceptualize the system and minimizes the work required to fit to data.

This model has a few limitations that arise from the assumptions used in the derivation. First, we only track the growth-limiting substrate and assume other nutrients are saturating, which means that the model cannot be used for systems that have more complex substrate interactions. Second, the model does not track sloughing events or reattachment of eroded cells, though this could be easily added, nor does it track biomass on

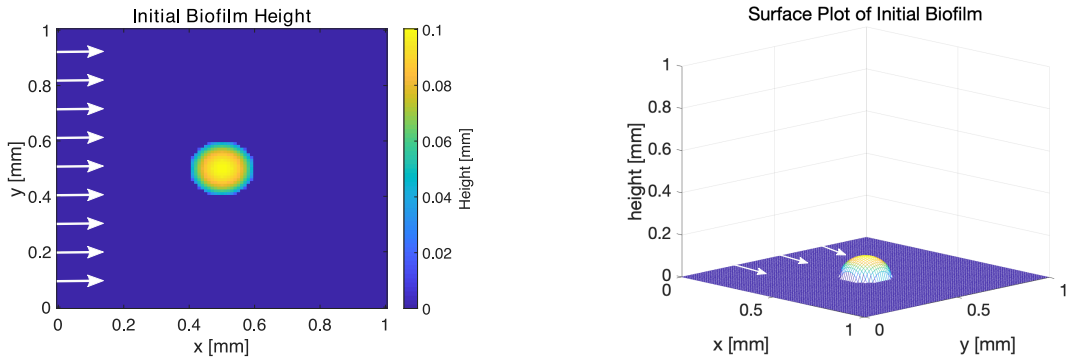

Initial location of biomass in flow cell

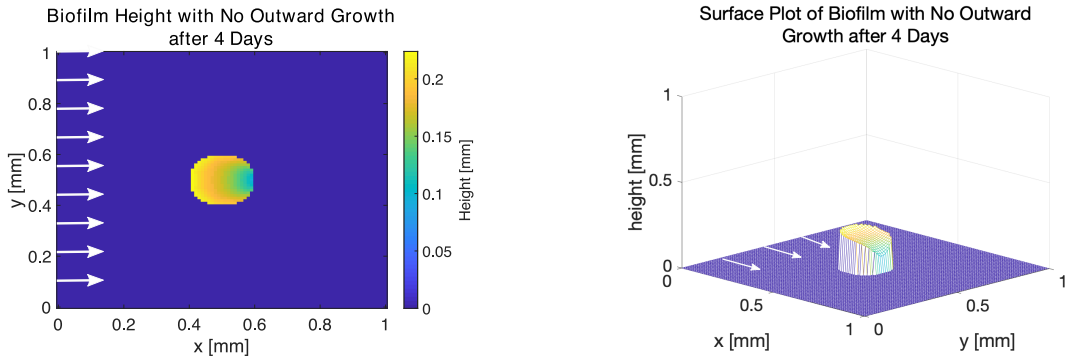

Biomass distribution after 4 days without outward growth

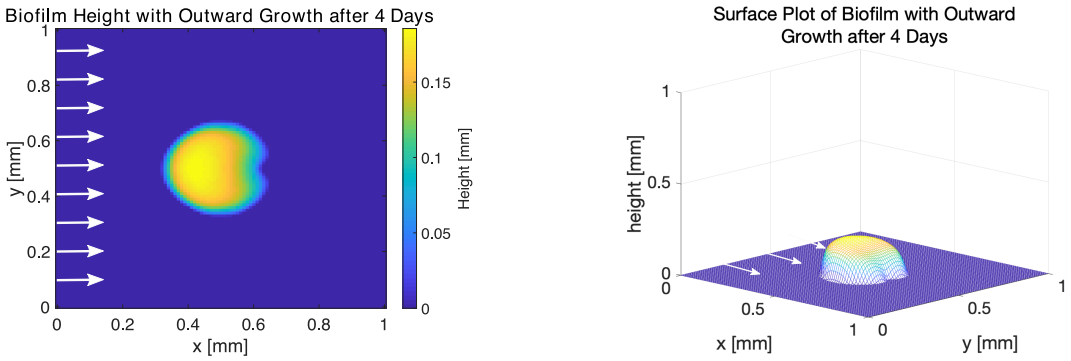

Biomass distribution after 4 days with outward growth

Figure 3.21. Outward growth of biomass in a flow cell of height .5mm with flow moving from left to right

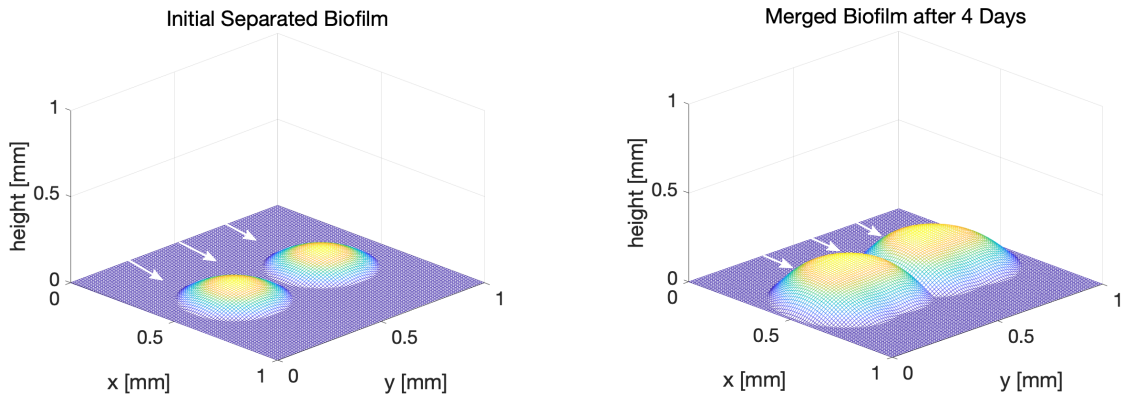

Figure 3.22. Outward growth adjustment allows two separate colonies to merge into a single colony.

the sides of the flow cell, which could underestimate biomass and substrate consumption near the side walls. Also, the parabolic substrate profile assumption will underestimate substrate consumption before the concentration relaxes to parabolic. If the flow in the channel is very fast, the profile may not relax to parabolic within the flow cell leading to a larger discrepancy in the outflow concentration when compared to data. Adjusting the model for these faster-flow conditions will be considered in future work. The model's representation of the biomass distribution is limited to large-scale features. Since the system only models large-scale behavior it cannot capture the small-scale variation in a biofilm's surface even if the user increases the grid resolution. The model assumes that the biofilm surface varies smoothly and slowly and will not be able to accurately solve for substrate concentration and growth for a biofilm in which nearby regions exhibit large variations in biomass. Despite these limitations, the model can be usefully applied to a large number of experimental systems.

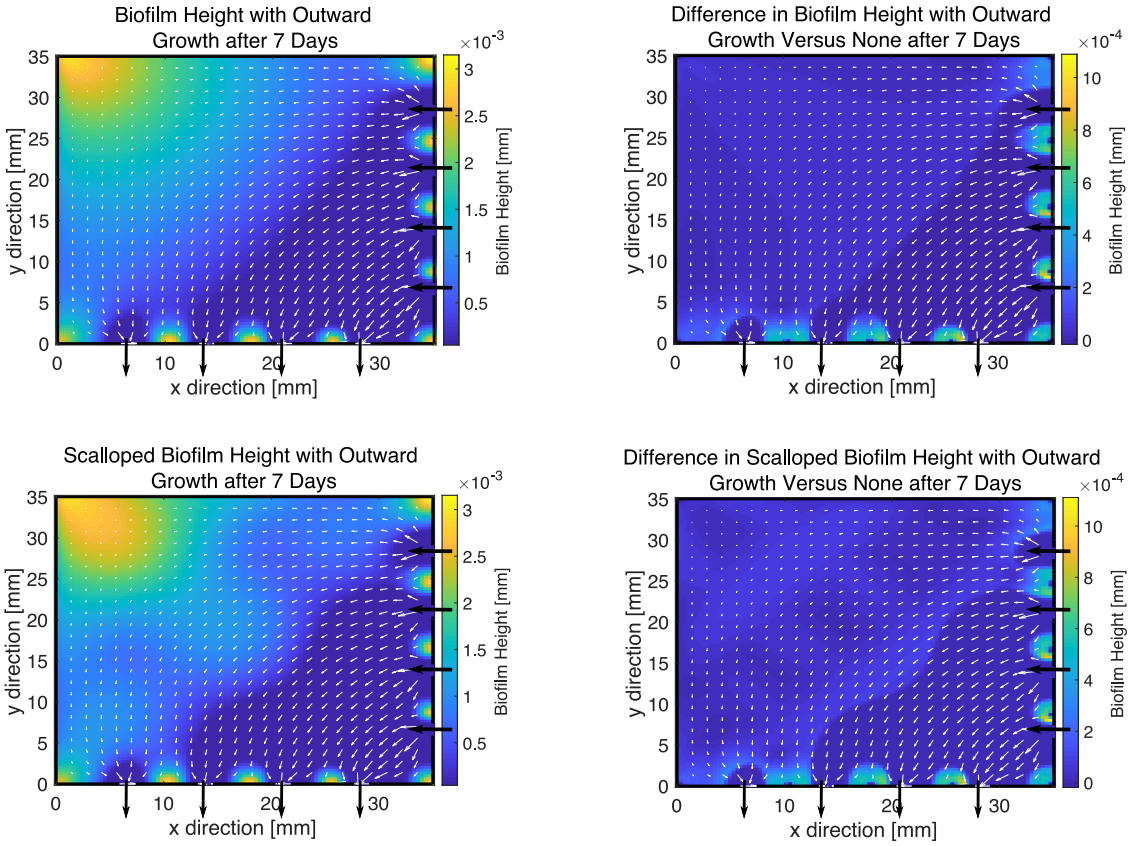

Figure 3.23. Computed biofilm height of system from Figure 3.15 with outward growth and the difference between this computed biofilm height and previous height computed with no outward growth. The model with outward growth has higher growth between the inlets and outlets due to the spreading of biomass from the center of these sheltered regions.

This model bridges the gap between bacterial colonies and large-scale flow cell dynamics. It will be useful to experimentalists interested in predicting environmental conditions in the small, imaged regions of the flow cell. The model can also provide boundary conditions to be used in more detailed biofilm simulations representing these imaged regions. Using this model, biofilm researchers can also begin to understand the biomass distribution and substrate concentration in parts of flow cells that are not directly observable,

which often constitute a large portion of the flow cell. This asymptotic model will help facilitate research into biofilms, improving our understanding of these widespread and complex bacterial communities.

CHAPTER 4

Modeling Electrical Communication in Biofilm

4.1. Introduction

Biofilms are collections of bacteria that grow on surfaces, and they can exhibit many unique, collective behaviors that allow them to survive in a variety of environments. Some known, collective behaviors include symbiotic relationships between multiple species within a biofilm and the development of physical channels between cells to facilitate nutrient penetration and distribution. More information on these well-studied, collective behaviors can be found in [**2**]. In this chapter we explore *Bacillus subtilis'* oscillatory growth pattern that emerges from potassium signaling, which was introduced in [**10**] and in [**8**] as another mechanism for cooperation within a biofilm.

Cells within a biofilm depend on nutrients from the surrounding fluid to survive, and these nutrients must diffuse into the biomass to reach bacteria throughout the biofilm. As a biofilm grows larger, cells near the interior often become starved for nutrients that must travel farther through active biomass to reach the interior. In the experiments in [**8**] the primary nutrient is glutamate, which is a nitrogen source that cells use for both growth and maintenance. This conflict between the growth of cells near the biofilm interface and the maintenance of the interior cells is discussed in [**10**]. As shown in [**8**], the electrochemical signaling is driven by the cellular release and uptake of potassium, a positive ion that the cells use to regulate their voltage differential. When cells become

metabolically stressed, they release potassium and hyperpolarize as shown in [**8**]. This release of potassium causes neighboring cells to uptake potassium and briefly depolarize, which interferes with their metabolic processes. Once these neighboring cells become stressed, they also release potassium and hyperpolarize, as shown experimentally in [**8**]. Collectively the cells generate a potassium wave that travels from the nutrient-starved interior to the exterior of the biofilm. This wave disrupts the entire biofilm's nutrient consumption. The disruption in consumption allows nutrients to diffuse deeper into the biofilm toward the starving interior cells. This mechanism enables the biofilm to continue to grow while avoiding a destabilizing level of cell death in its interior, as explained in [**10**].

Previous work using one-dimensional models also suggests that the oscillations arise from metabolic stress and propagate through changes in potassium, as demonstrated by the model introduced in [**9**]. In this chapter, we build on this metabolic propagation mechanism by introducing a new method of cell-to-cell communication in which the cells react to changing potassium levels instead of the absolute potassium level. This model is consistent with the observation that bacteria can adjust to living in environments that possess a range of potassium concentrations. The mechanisms through which *B. subtilis* adapts to these environments are discussed in [**74**]. We then use this set of equations to develop a two-dimensional model to more accurately represent the experiments in [**8**] and to study variations in the oscillation patterns seen in these experiments. This model is useful in studying multi-dimensional phenomena that appear within biofilm systems such as the communication between separated colonies.

4.2. One-Dimensional Model

We first develop a one-dimensional model that represents a cross section of the biofilm, and it is based on the continuum model developed in [**35**]. The model relies on cellular metabolism to initiate and propagate the signal. These oscillations have been linked to metabolism in previous research, such as in [**10**] and in [**75**]. A biofilm begins to oscillate at a smaller size in environments with lower ambient glutamate as shown in [**9**]. This result suggests that there is a glutamate threshold under which the cells become stressed and hyperpolarize. The timescale of the oscillation, which has a period near two to three hours, is also consistent with the timescale of nutrient consumption. Metabolism also plays an important role in the model we develop in this chapter.

In developing our model we consider a model proposed by [**9**] that is able to replicate much of the behavior that we see in experiments. The main differences between the model from [**9**] and the model introduced here is that we change the cells' response to extracellular potassium, we simplify the boundary condition, and we account for the decrease in extracellular potassium as potassium molecules leak into the cell. We find that this updated model better captures the inverse relationship between the voltage and the extracellular potassium seen in experiments from [**8**].

We first consider how a rise in the external potassium concentration can affect the metabolism of a cell. We assume that a rise in environmental potassium causes potassium to leak into the bacteria, thereby depolarizing the cell and affecting its glutamate consumption. While there are a few ways through which voltage changes can affect consumption, [**9**] assumes that a bacterium cannot uptake glutamate if it is depolarized away from its homeostatic voltage even if glutamate is environmentally available. It is possible that the

voltage change affects other cellular processes and molecules such as ammonium within the cell instead of the glutamate intake, which would in turn affect the usage of glutamate. The role of ammonium in these oscillations is examined in [**10**]. A model based on changes to other metabolic processes would lead to a similar decrease in the cellular metabolism of depolarized cells as the model that is based on a diminished glutamate uptake. While the biological processes that lead to the stressed response are worthy of further study, we cannot fully address them in this modeling study. The important effect for the purposes of this model is that depolarized cells metabolize glutamate more slowly, and they become stressed and hyperpolarize to recover. The mechanism for the reduced glutamate metabolism that we use in this model is the same as that used in [**9**], which assumes that depolarized cells cannot uptake glutamate.

In our model we introduce a diffusive-flux boundary condition at the biofilm interface. The model in [**9**] uses an artificial approximation to calculate the glutamate and potassium influx. It defines the exchange of these molecules at a point within the biofilm as a function of that point's distance to the exterior interface. In this model we replace this boundary calculation with a traditional Neumann flux boundary condition because the Neumann boundary condition is simpler to implement for two-dimensional biofilms with irregular shapes.

Potassium, a positively charged ion, is the main signaling molecule in this model, and it diffuses in the spaces between the cells. We do not have experimental results that allow us to directly measure this diffusion process. Instead, we fit the model's potassium distribution to the potassium distribution observed in experiments. In the experiments we see high concentrations of potassium throughout the biofilm for an extended period

after the cells hyperpolarize. Many biofilm models assume that the diffusion rate inside the biofilm is around 60% of the diffusion rate in the fluid, and we use this assumption here to set the glutamate diffusion rate. We find that a model with a potassium diffusion rate in the biofilm that is less than 60% of the fluid diffusion rate better matches the higher experimental potassium concentrations. A high diffusion rate leads the potassium to diffuse too quickly out of the biofilm and into the flow. Our usage of a lower diffusion rate corresponds with the results from [**76**] in which the potassium diffusion is modeled as a percolation process where potassium released from one cell can only affect the cell's direct neighbors. The authors find that the percentage of cells that participate in the voltage oscillations reflects the percentage required for efficient transmission in percolation theory. This result suggests that potassium cannot diffuse far from the cell from which it originates. We model this confined movement by setting the diffusion coefficient for potassium within the biofilm to be significantly smaller than the coefficient within the fluid.

The equations for the external glutamate and potassium concentrations, G and K respectively, within the biofilm are defined below:

$$\frac{\partial G}{\partial t} = D_G \frac{\partial^2 G}{\partial x^2} - \frac{\delta_G}{(1+\exp(V - V_{th}))} G(G_{max} - G_{in}), \tag{4.1}$$

$$\frac{\partial K}{\partial t} = D_K \frac{\partial^2 K}{\partial x^2} + F g_K n^4 (V - V_K) + F g_L (V - V_L) - \max(\gamma_K K(K_{max} - K_{in}), 0). \tag{4.2}$$

Glutamate and potassium diffuse through the biofilm in the spaces between the cells, and this diffusion is represented by the first terms of Equations (4.1) and (4.2). Their

diffusion rates are defined as D_G and D_K respectively. The values used for these and other parameters in the simulations are listed in Table 4.1.

The second term in Equation (4.1) models the glutamate uptake by the bacteria. The bacteria uptake glutamate if they are sufficiently polarized, there is glutamate in the environment, and the cells' internal glutamate level is below their maximum concentration. The cells uptake glutamate using transporters powered by the proton motive force, which is explained in [**9**]. The cells must maintain a certain level of polarization to uptake glutamate, which is examined in [**77**]. We use the same function for the dependence of glutamate uptake on voltage as [**9**]. The exponential term in this expression corresponds to the quick halting of glutamate uptake if the cells' voltage differential, V, moves above their homeostatic voltage differential, V_{th}, thereby decreasing the magnitude of their voltage differential. This exponential relationship reflects the sensitivity of the glutamate transporters. Glutamate uptake is also dependent on the glutamate availability in the environment and on the cells' need for glutamate, which we define as the difference between the maximum interior glutamate level, G_{max}, and the cells' internal glutamate level, G_{in}.

Equation (4.2) represents the external potassium concentration as the molecules diffuse through the biofilm and move through the cellular membrane both passively and actively. Potassium moves passively through the potassium gates and through the leak gates. The potassium gates are channels that the cell can open and close to allow potassium to enter or leave the cell. The leak gates represent the permeability of the cell membrane, which allows potassium to enter or leave the cell through small holes. In the model, the potassium and leak gate are controlled by the openness of the potassium gates, n, and the corresponding reversal potentials for the potassium and leak gates, V_K and V_L. Here,

F is a factor converting the voltage change to a potassium change. We approximate the potassium uptake and release through the potassium and leak gates using terms from the Hodgkins-Huxley model introduced in [**78**]. Allowing the extracellular potassium to move into the cells through the leak gates and decrease the external potassium concentration is a new feature of this model that reflects the mechanism through which the extracellular potassium depolarizes a cell. A higher concentration of extracellular potassium increases the potassium uptake due to an increased osmotic pressure. Previous models focused on how this potassium movement through the leak gates affects the voltage differential but did not account for the effects within the potassium concentration itself. Including this uptake in the model ensures that the increase in extracellular potassium during a depolarization event is moderated by the potassium uptake of the depolarizing cells. The final term in Equation (4.2) represents the cells' potassium pumps through which they can actively uptake nearby potassium if their internal potassium concentration, K_{in}, falls below a threshold, K_{max}. The max function in this potassium pump term ensures that the cells only use this pathway to uptake potassium and not to release potassium.

The boundary conditions for glutamate and potassium at the biofilm's exterior interface require that the concentrations are continuous across the boundary and that the fluxes are continuous as well, which are described by the Neumann flux conditions below:

$$D_G \frac{\partial G}{\partial x} = D_G^{fl}(G_0 - G_{int})/B_L, \tag{4.3}$$

$$D_K \frac{\partial K}{\partial x} = D_K^{fl}(K_0 - K_{int})/B_L, \tag{4.4}$$

where D_G^{fl} and D_K^{fl} are the diffusion rates of glutamate and potassium in the fluid, G_0 and K_0 are the long-range glutamate and potassium concentrations, G_{int} and K_{int} are

the interfacial glutamate and potassium concentrations, and B_L is the boundary layer width. At the interior interface at $x = 0$ the boundary conditions are no-flux in which, $\partial G/\partial x = \partial K/\partial x = 0$.

The corresponding equations for the glutamate and potassium concentrations in the interior of the cell, G_{in} and K_{in} respectively, are as follows:

$$\begin{aligned}\frac{dG_{in}}{dt} &= \frac{\delta_G}{(1+\exp(V-V_{th}))}G(G_{max}-G_{in}) - \gamma_G G_{in}(M_{grow}+r_b) \\ &\quad - \frac{\partial}{\partial x}(UG_{in}),\end{aligned} \tag{4.5}$$

$$\begin{aligned}\frac{dK_{in}}{dt} &= -Fg_K n^4(V-V_K) - Fg_L(V-V_L) + \max(\gamma_K K(K_{max}-K_{in}),0) \\ &\quad - \frac{\partial}{\partial x}(UK_{in}).\end{aligned} \tag{4.6}$$

Equation (4.5) models the glutamate concentration inside the bacteria. The first term represents the cells' glutamate intake. This term balances the external glutamate concentration in Equation (4.1), but with an opposite sign to represent the transport of glutamate across the cell membrane. The second term represents the cells' glutamate consumption for both its base metabolism and growth, where γ_G is the glutamate consumption rate. The cells require glutamate to perform their base metabolic functions, and this need is represented as r_b in the equation. The cells also use glutamate to grow, and their growth propensity is represented by the variable M_{grow}. Growth can only occur when the bacteria are in "Grow Mode," or when M_{grow} is high. When the bacteria are stressed, M_{grow} is low, which slows the glutamate consumption of the bacteria and allows for the glutamate to penetrate the biofilm more deeply. A prominent feature of the model in [**9**] is that the cells uptake more glutamate when they have a higher internal glutamate

level. This property creates a delay in the glutamate uptake that prevents the bacteria from reaching a steady state, which allows for sustained oscillations. In this model we use M_{grow} as a variant of this consumption delay where the biofilm cannot be hyperpolarized and grow. We discuss the variable M_{grow} in more detail below.

Equation (4.6) represents the cells internal potassium concentration. The first three terms of this equation are also found in Equation (4.2) to represent the transport of potassium across the cell membrane.

The advection terms within Equations (4.5) and (4.6) reflect that G_{in} and K_{in} are quantities within an individual cell that are pushed outward as the biofilm grows. Here, U is the biofilm growth velocity defined throughout the biofilm. The growth velocity at each point in a one-dimensional cross section of a biofilm is the sum of the biomass growth between that point and the wall. As bacteria reproduce, they push the biomass above them farther into the fluid flow, which is discussed in [**35**]. All non-diffusive quantities in this system move with the cellular growth and have a corresponding advection term in their equations.

The following equations define M_{grow} and the corresponding growth equations:

$$M_{grow} = \frac{G_{in}}{G_{in}+G_u}/ \left(\frac{G_{in}}{(G_{in}+G_u)} + (\eta_V \tanh(\gamma_V(-V/V_{low}-1))+1)\right), \tag{4.7}$$

$$U(x) = \delta_{grow}\int_0^x G_{in}M_{grow}dx, \tag{4.8}$$

$$\frac{dL}{dt} = \delta_{grow}\int_0^L G_{in}M_{grow}dx. \tag{4.9}$$

Equation (4.7) defines the variable M_{grow}, which reflects the growth propensity of the cells. The variable M_{grow} varies between zero and one where the cells grow faster if M_{grow} is close to one. Let $T_G = \frac{G_{in}}{G_{in}+G_u}$ and $T_V = (\eta_V \tanh(\gamma_V(-V/V_{low} - 1)) + 1)$. Then T_G is a Hill activation function that is large when G_{in} is higher than the lower bound G_u, and T_V is a hyperbolic tangent activation function that is large when V is above the bound V_{low}. The parameters η_V and γ_V are shape parameters for the hyperbolic tangent activation function. Equation (4.7) is the steady-state solution of the differential equation $\frac{\partial M_{grow}}{\partial t} = (1 - M_{grow})T_G - M_{grow}T_V$. Then M_{grow} will be close to 1 and the bacteria will grow if T_G is much larger than T_V. The variable M_{grow} ensures that the cells only grow when both their internal glutamate is high, making T_G large, and they are not hyperpolarized, making T_V small. Since cells consume glutamate at a much lower rate when hyperpolarized, the nutrients can penetrate deeper into the biofilm and arrive at the starving cells near the interior. The requirement that the cells be near their homeostatic voltage differential in order to grow reflects what we see in experimental data from [**76**].

As developed in [**35**], Equations (4.8) and (4.9) represents the biofilm's growth, where δ_{grow} is the growth rate. Equation (4.8) computes the growth at any point within the biofilm as an integral of the biomass growth between that point and the base of the biofilm. Equation (4.9) represents the growth of the biofilm's length, L, which is the distance between the base and the edge of the biofilm.

The most important difference in this model compared to previous ones relates to how the cells react to potassium. In our model cells respond to changes in potassium instead of the absolute potassium level as represented in Figure 4.1. We assume that only the newly arriving potassium molecules affect the cells' voltages. We base this

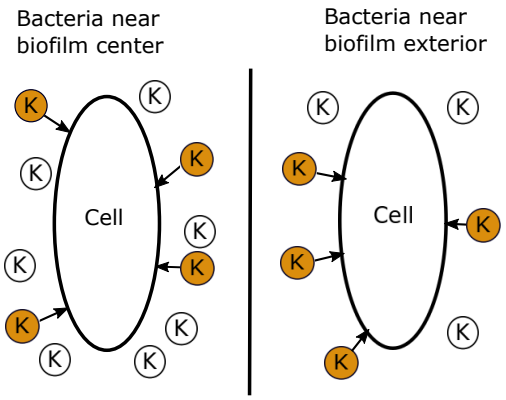

Figure 4.1. Depolarization of cells due to the influx of potassium near the center of the biofilm versus near the exterior. The potassium colored orange are newly arrived molecules, and we assume that they have same depolarizing effect on both cells despite differing ambient potassium concentrations.

assumption on the evidence that bacteria can adjust to a range of potassium levels over time. For example, *Escherichia coli* have mechanisms to adjust their internal potassium level to reach a homeostasis [**79, 80**]. Furthermore, *E. coli* can grow under a range of external potassium levels [**81**]. *B. subtilis* has similar mechanisms to adapt to a variety of environmental potassium concentrations, which are discussed in [**74**]. A change in environmental potassium is likely a better indicator of cellular stress since the change in potassium forces bacteria out of their equilibrium state. We create the variable $K_{acclimated}$ to represent the potassium level to which the cells are accustomed. This variable then follows K linearly at a rate of η_K in the following equation:

$$\frac{dK_{acclimated}}{dt} = \eta_K(K - K_{acclimated}) - \frac{\partial}{\partial x}(UK_{acclimated}). \tag{4.10}$$

The voltage is affected by the difference between the environmental potassium level, K, and the level to which it is accustomed, $K_{acclimated}$, which is incorporated into the

reversal potential for the leak gates V_L. The following set of equations describe the voltage differential within the biofilm:

$$\frac{dV}{dt} = -g_k n^4 (V - V_K) - g_L (V - V_L) - \frac{\partial}{\partial x}(UV), \tag{4.11}$$

$$\frac{dn}{dt} = \alpha \frac{(G_{max} - G_{in})^m}{(G_{max} - G_l)^m + (G_{max} - G_{in})^m}(1 - n) - \beta n - \frac{\partial}{\partial x}(Un), \tag{4.12}$$

$$V_K = V_{K0} + \delta_K K, \tag{4.13}$$

$$V_L = V_{L0} + \delta_L (K - K_{acclimated}). \tag{4.14}$$

Equation (4.11) represents the voltage differential across the cells' membranes, V. In this model, the cells use potassium to modify this voltage differential. The terms in this equation are from the Hodkin-Huxley model, and they correspond to the potassium and leak gate terms from the potassium equations, Equations (4.2) and (4.6).

Equation (4.12) represents the openness of the cells' potassium gates, n. The gates open with the opening rate α according to the expression

$$\frac{(G_{max} - G_{in})^m}{(G_{max} - G_l)^m + (G_{max} - G_{in})^m},$$

which is similar to a Hill function with m as the Hill coefficient. However, this expression is large when $G_{in} < G_l$ and small when $G_{in} > G_l$. This expression activates the starving response in the bacteria when their internal glutamate level is low. With low internal glutamate, the bacteria open their potassium gates to release potassium and hyperpolarize. The decay term in Equation (4.12) represents that bacteria close their potassium gates at a decay rate of β if they are not experiencing stress.

The reversal potentials V_K and V_L are defined in Equations (4.13) and (4.14). The reversal potential for the potassium gates, defined in Equation (4.13), has a base value of V_{K0} and is affected by the external potassium concentration with an influence strength of δ_K. The reversal potential for the leak gates, defined in Equation (4.14), has a base value of V_{L0} and is affected by the difference between the environmental potassium level, K, and the level to which it is accustomed, $K_{acclimated}$. The parameter δ_L defines the strength of this influence. A rise in the external potassium leads the potassium to leak into the bacteria causing the cells to depolarize.

Most experimental data from these systems is reported as the fluorescence of molecular indicators. We convert both the voltage and potassium concentrations to their corresponding fluorescent indicators, thioflavin T (ThT) and asante potassium green (APG), named T and A respectively in the equations below:

$$\frac{dT}{dt} = \frac{\alpha_T}{1 + \exp(g_T(V - V_{0T}))} - \gamma_T T - \frac{\partial}{\partial x}(UT), \tag{4.15}$$

$$\frac{dA}{dt} = \alpha_A K - \gamma_A A - \frac{\partial}{\partial x}(UA). \tag{4.16}$$

Equation (4.15) is the same equation for ThT fluorescence used in [**9**]. The indicator ThT fluoresces if the voltage falls below the threshold V_{0T}. The exponential term produces a strong transition point for ThT fluorescence if the voltage differential drops below V_{0T}. The parameter g_T adjusts ThT's sensitivity to this transition point, and γ_T is the decay rate of the indicator. Equation (4.16) uses a linear model to represent the fluorescence of APG where α_A is the activation strength of APG, and γ_A is the decay rate of the indicator.

Together these equations form an oscillatory system for both the growth and the voltage differential. The starving cells release potassium, which disrupts the metabolism of neighboring cells, causing them to become stressed and stop growing. The cells release potassium to hyperpolarize when stressed which creates the potassium wave that moves from the center of the biofilm to the exterior. The hyperpolarized bacteria refrain from growing while recovering, allowing glutamate to diffuse deeper into the biofilm. This one-dimensional model reproduces prominent features from experiments as discussed in the following sections.

Table 4.1. Parameters Used in Oscillatory Model

Name	**Description**	**Value**	**Reference**
D_G	Glutamate diffusion coefficient in biofilm	0.540 $\frac{\text{mm}^2}{\text{day}}$	Assumed
D_K	Potassium diffusion coefficient in biofilm	0.497 $\frac{\text{mm}^2}{\text{day}}$	Fitted
D_G^{fl}	Glutamate diffusion coefficient in fluid	0.900 $\frac{\text{mm}^2}{\text{day}}$	Known
D_K^{fl}	Potassium diffusion coefficient in fluid	4.97 $\frac{\text{mm}^2}{\text{day}}$	Known
G_0	Glutamate concentration at inlet	30 mM	[**8**]
K_0	Potassium concentration at inlet	8 mM	[**8**]
δ_G	Glutamate uptake rate	10 $\frac{1}{\text{hour}}$	Fitted
V_{th}	Voltage above which cells cannot uptake glutamate	-150 mV	[**8**]

Continued on next page

Table 4.1 – continued from previous page

Name	Description	Value	Reference
G_{max}	Maximum glutamate concentration in cell	20 mM	Fitted
F	Voltage to potassium conversion factor	$5.6\frac{\text{mM K}}{\text{mV}}$	[**8**]
g_K	Potassium gate strength	180/hour	Fitted
g_L	Leak gate strength	1.2/hour	Fitted
γ_K	Potassium pump strength	2/(hour × mM K)	Fitted
B_L	Boundary layer length	0.5 mm	Fitted
γ_G	Glutamate consumption rate	.75/hour	Fitted
r_b	Glutamate basal consumptions rate	0.1 (dimensionless)	Fitted
G_u	Glutamate bound below which the cells do not grow	18 mM Glutamate	Fitted
η_V	Voltage influence in M_{grow}	20 (dimensionless)	Fitted
γ_V	Voltage transition speed in M_{grow}	20 (dimensionless)	Fitted
V_{low}	Voltage below which cells do not grow	180 mV	Fitted
δ_{grow}	Biomass produced in growth	$\frac{0.005\text{mm}}{\text{mM Glutamate}\times\text{hour}}$	Fitted
η_K	Cells' acclimation rate to potassium change	30/hour	Fitted
α	Potassium gate opening rate	5/hour	Fitted
β	Potassium gate closing rate	2.5/hour	Fitted
m	Potassium gate exponent	2 (dimensionless)	Fitted

Continued on next page

Table 4.1 – continued from previous page

Name	Description	Value	Reference
G_l	Glutamate level below which cells hyperpolarize	10 mM Glutamate	Fitted
V_{K0}	Basal potassium gate reversal potential	-380 mV	[**8**]
V_{L0}	Basal leak gate reversal potential	-156 mV	[**8**]
δ_K	Potassium gate reversal change	$1\frac{\text{mV}}{\text{mM}}$	[**8**]
δ_L	Leak gate reversal change	$60\frac{\text{mV}}{\text{mM}}$	Fitted
α_T	ThT fluorescence strength	$20\ \frac{\text{mM}}{\text{hour}}$	[**9**]
g_T	ThT relation to voltage	0.3 mV	[**9**]
V_{0T}	Voltage level below which ThT fluoresces	-170 mV	Fitted
γ_T	ThT decay rate	10/hour	[**9**]
α_A	APG fluorescence strength	0.5/hour	Fitted
γ_A	APG decay rate	1/hour	Fitted

4.2.1. Comparing Voltage, Growth, and Potassium to Experiments

To validate the set of equations introduced in the previous section, we compare important quantities from the model to the experimental data such as the relationship between voltage oscillations, the growth, and the potassium concentration. Experiments show that a biofilm typically grows when its cells are not hyperpolarized. Hyperpolarized cells are in the process of recovering from a disruption in their metabolism. Data demonstrating

the trade-off between growth and hyperpolarization is shown in [**76**]. The model prevents bacteria from growing while hyperpolarized through the M_{grow} variable. This effect can be seen in Figure 4.2, which shows that the biofilm grows faster when its average voltage is higher. We compare this relationship to experimental data from [**8**] in Figure 4.3. We see that in both the experimental data and the simulation that growth is high when the fluorescence indicating hyperpolarization is low, and the growth is low when the fluorescence is high.

We see that in experiments from [**8**] the average external potassium increases within the biofilm as the average voltage differential decreases. This property is integral to the system because it reflects how the signal is propagated within the biofilm. If a cell releases potassium, its voltage differential becomes more negative as it is losing a positive ion. A newly released potassium ion may enter a neighboring cell, but the voltage change from this uptake cannot more than offset the voltage change in the biofilm caused by the ion leaving its previous cell. This property has not been adequately reflected in previous models, such as in [**9**]. We implemented the model from this paper, and while voltage and potassium are inversely related in the model's original form, this relationship changes when we update the flux boundary at the biofilm interface to a Neumann boundary so that we can use the model in a multi-dimensional simulation. When we make this change and set the interior diffusion rate to be constant, the potassium and voltage are no longer inversely related. We show the data from our implementation of this model in Figure 4.5. We see that the voltage and potassium are inversely related in the original form, but the modified model shows an increase in the voltage during a period when cells are releasing potassium, which appears to be nonphysical. In Figure 4.2, we see that our model correctly

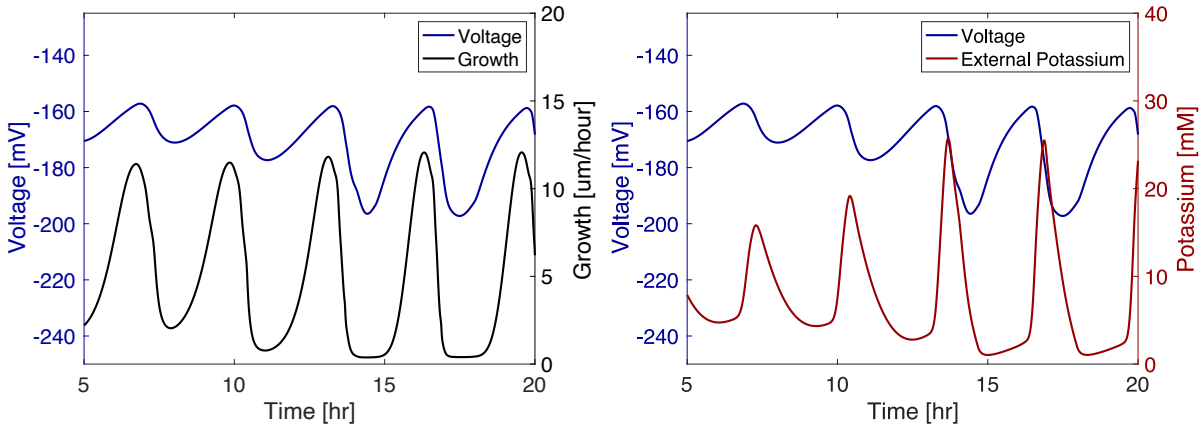

Figure 4.2. (Left) Mean voltage and growth over time from the model. Voltage is positively related to growth. The oscillations become stronger over time. Growth occurs when the biofilm is not hyperpolarized. (Right) Mean voltage and mean potassium over time from model. Voltage is negatively related to potassium. Potassium is at its highest when the biofilm is depolarizing as the cells release potassium. Potassium begins to fall before the voltage increases because some of the potassium diffuses into the bulk flow.

indicates that the voltage falls as the external potassium increases. Potassium and voltage are not strictly inversely related because the potassium diffuses out of the biofilm causing the potassium levels to drop before the rise in the voltage. We compare these quantities to data from [**8**] in Figure 4.4 where the fluorescence indicating hyperpolarization and the fluorescence indicating external potassium rise and fall in relative synchronicity for both the experimental and the model data. The initial conditions used in the one-dimensional simulations are $G = 30$, $K = 8$, $G_{in} = 20$, $K_{in} = 200$, $K_{acclimated} = 8$, $V = -156$, and $n = 0.1$.

4.2.2. Size at Oscillation Onset and Period Length

The size at which the biofilm initiates its first oscillation depends on the nutrient availability and the cellular consumption rate of the glutamate within the biofilm. We fit the

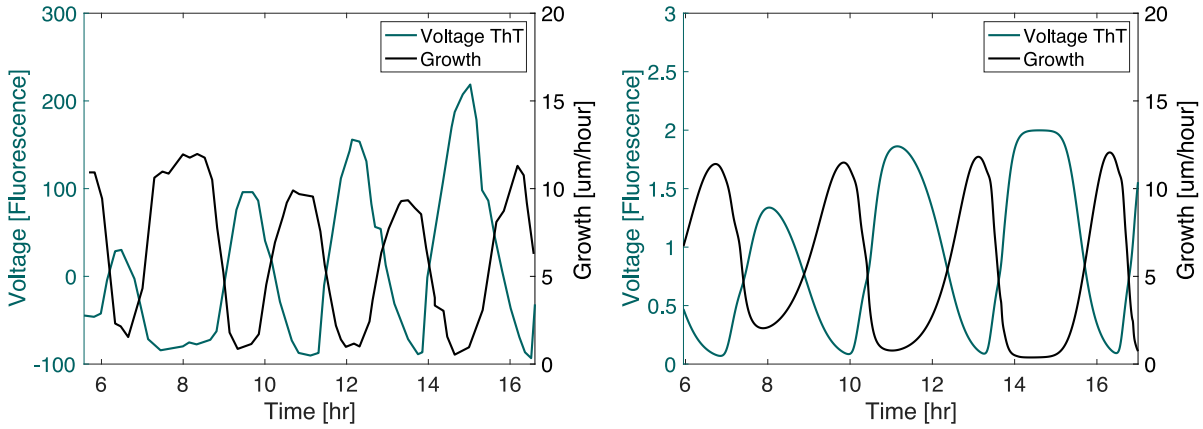

Figure 4.3. (Left) Experimental mean voltage fluorescence and growth adapted from [**8**][1]. Voltage is measured as its fluorescent indicator, ThT, which exhibits higher fluorescence when the cell is more polarized meaning that the voltage differential is more negative. The voltage fluorescence and the growth are inversely related. (Right) Mean voltage fluorescence and growth from the model. The quantities from the model demonstrate a similar pattern to those from the experiment. Note that the fluorescence data from the experiment are scaled differently than the model data.

growth rate of the model so that the biofilm initiates its oscillatory behavior at the same size seen in experimental biofilms in 30 millimolar glutamate solutions. In Figure 4.6 we see that in both the experiments and the model the mean size at which the biofilms begin to oscillate is near 500 microns in diameter. The experiments have a larger variability around the mean than the model, which is typical of the natural variability inherent in physical systems.

In both the model and the experiments, we see that the period of oscillation increases as the biofilm size increases, as shown in Figure 4.7. This effect could make strategic sense as a larger biofilm may need to halt growth for a longer time to allow nutrients to

[1]Adapted by permission from Springer Nature Customer Service Centre GmbH: Springer Nature, Nature, Ion channels enable electrical communication in bacterial communities, Prindle et al. Copyright 2015 Macmillan Publishers Limited. (2015), https://www.nature.com

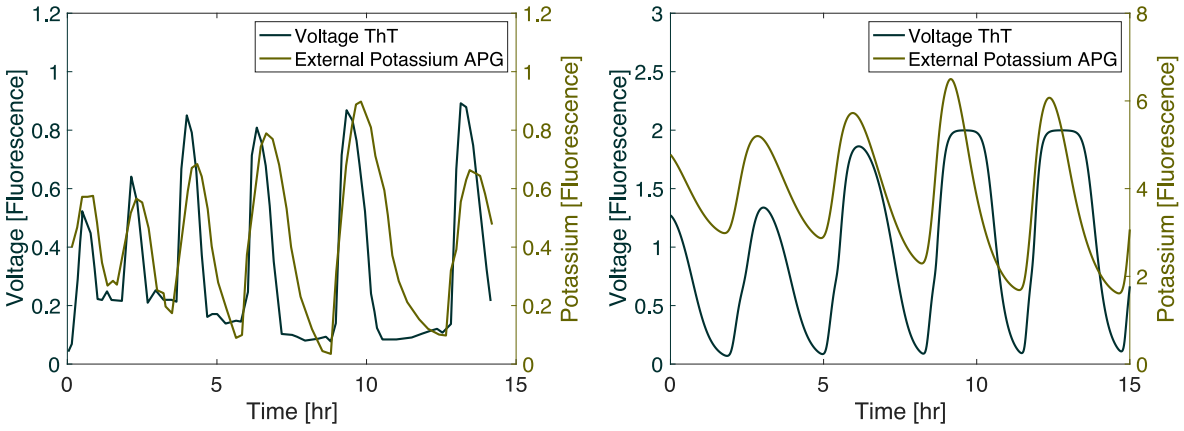

Figure 4.4. (Left) Experimental mean voltage and potassium fluorescence adapted from [8][2]. The fluorescence of the voltage indicator, ThT, is higher when the cell is more polarized, and the fluorescence of the potassium indicator, APG, is higher when the extracellular potassium concentration is higher. The fluorescence for voltage and potassium are highly correlated. (Right) Mean voltage and potassium fluorescence from the model. The quantities from the model show a similar pattern to those in the experiment. Note that the fluorescence data from the experiment are scaled differently than the model data.

penetrate more deeply to under-served regions. In the model, the biofilm takes longer to recover from a hyperpolarization event because the biofilm is slower to rid itself of the excess extracellular potassium. In the model data, we also see a convergence to a longer period of oscillation in Figure 4.7. This convergence occurs because only a portion of the biofilm participates in the oscillations. The depth of this participatory portion near the fluid interface reaches a limit as the biofilm grows larger. The center of the biofilm remains constantly hyperpolarized and has little effect on the oscillations.

[2]Adapted by permission from Springer Nature Customer Service Centre GmbH: Springer Nature, Nature, Ion channels enable electrical communication in bacterial communities, Prindle et al. Copyright 2015 Macmillan Publishers Limited. (2015), https://www.nature.com

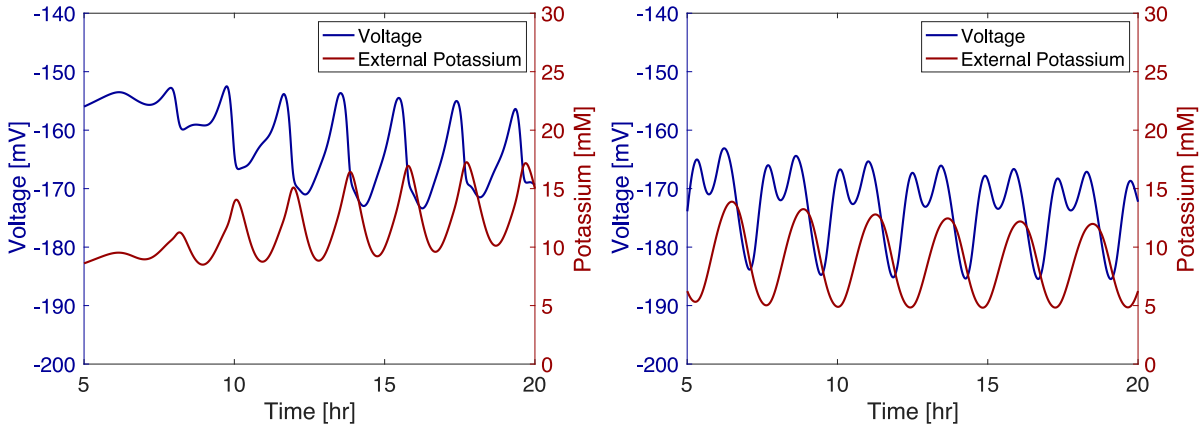

Figure 4.5. (Left) Mean voltage and potassium from an implementation of the model from [**9**]. In this model, voltage and potassium appear to be inversely related. (Right) Mean voltage and potassium from an implementation of the same model but with a Neumann flux boundary condition and a constant internal diffusion rate. Here, we see that extracellular potassium is increasing while mean voltage initially rises, which appears to be nonphysical.

Having validated our one-dimensional model by comparing the quantities of mean voltage differential, mean potassium concentration, and oscillation period, we use this set of equations to create a two-dimensional model in the following section.

4.3. Two-Dimensional Model

In this section we introduce a two-dimensional model to represent the data from the experiments performed in [**8**]. The flow cell in their experiment is about 3mm long and 3mm wide but only about 5-7 microns in depth. The narrow depth only allows the biofilm to grow about 5-7 cells deep, which confines the colony to a natural two-dimensional cross section. This cross section allows the experimentalists to visualize properties within the biofilm that would typically not be visible from the exterior of a three-dimensional colony. By imaging an interior slice of a colony, we can track how the electrical impulse moves

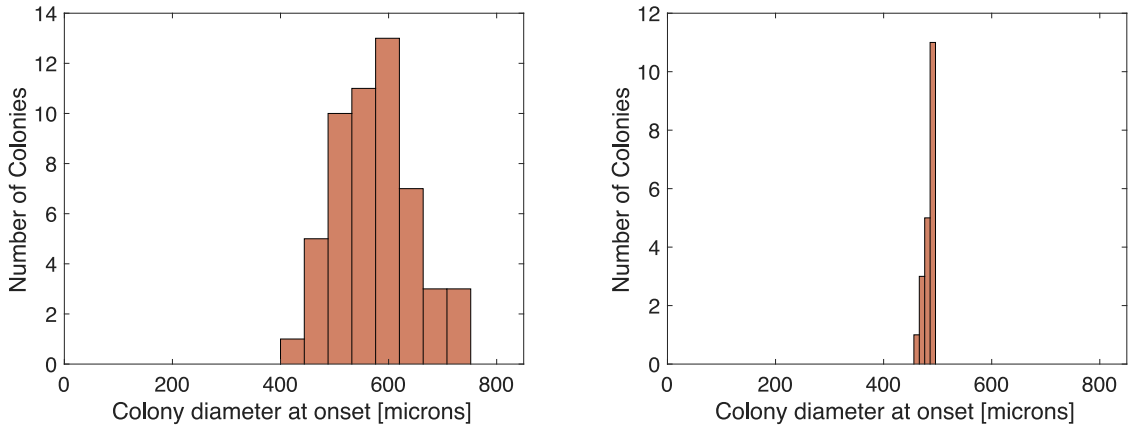

Figure 4.6. (Left) Experimental colony size at the onset of oscillations in 30 millimolar solution of glutamate, adapted from [**10**][3]. The plot has 53 observations. The mean diameter at oscillation onset is about 500 μm. (Right) Onset size of oscillations for model biofilm under the same glutamate concentration. The size is calculated as the mean of the biofilm's size at the start and at the end of the oscillation. The plot has 20 observations. The model also shows a mean onset size of about 500 μm. The small variation seen in the model is due to randomly initiating the biofilm's size at the start of the simulation. The experiment has a higher standard deviation, which is common in physical systems.

from the interior to the exterior of the colony. We model the propagation of this signal using a two-dimensional model based on the continuum model developed in [**5**]. This system uses a Stokes-flow approximation to solve for the fluid velocity through the flow cell. Let u and v be the $x-$ and $y-$directional fluid velocities, μ be the fluid viscosity,

[3]Adapted by permission from Springer Nature Customer Service Centre GmbH: Springer Nature, Nature, Metabolic co-dependence gives rise to collective oscillations within biofilms, Jintao Liu et Al. Copyright 2015 Macmillan Publishers Limited. (2015), https://www.nature.com

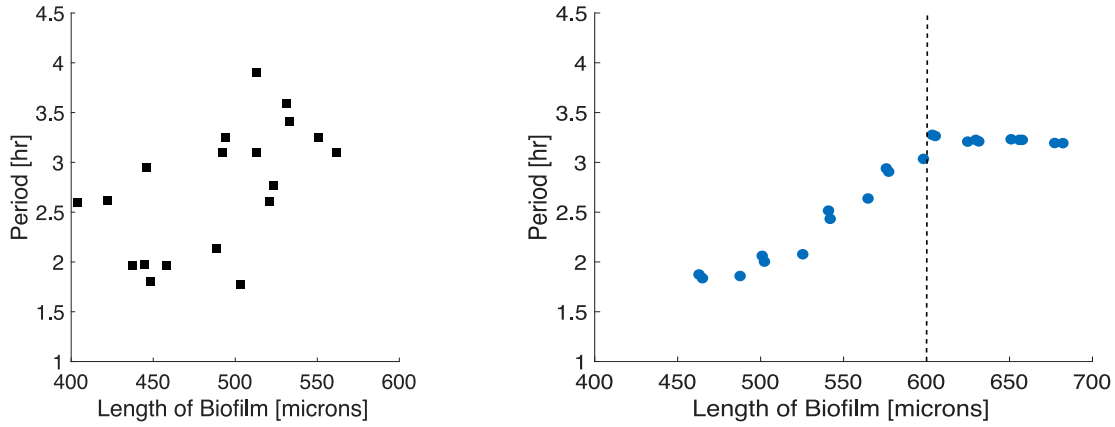

Figure 4.7. (Left) Experimental period of oscillation by biofilm size adapted from [**11**] with permission from Rosa Martinez-Corral. The oscillation period lengthens as the biofilm grows. (Right) Period of oscillation by biofilm size from the model. The size is calculated as the mean of the biofilm's size at the start and at the end of the oscillation. To the left of the dashed line is model data from the same domain as the experimental data. To the right of the dashed line is predicted data. The model also shows that the period lengthens as the biofilm grows, and it predicts that the biofilm will reach a maximum oscillation period as it grows larger.

and P be the pressure field. Then the reduced equations for the fluid flow are

$$\begin{aligned} \mu\nabla^2 u &= \frac{\partial P}{\partial x}, \\ \mu\nabla^2 v &= \frac{\partial P}{\partial y}, \\ \nabla^2 P &= 0. \end{aligned}$$

The flow cell has a rectangular shape defined by an inlet on the left side, an outlet on the right side, and walls on the top and the bottom of the domain. The boundary condition for the fluid at the interior walls and at the biofilm boundary is a no-slip and no-penetration boundary condition where $u = 0$, $v = 0$, and $\nabla P \cdot \vec{n} = 0$, where $\vec{n}$ in the outward normal.

At the inlet we use the boundary conditions $u = u_0$, $v = 0$, and $\partial u/\partial x = 0$, where u_0 is the initial speed. At the outlet we approximate a far-field boundary with the conditions $\partial u/\partial x = 0$, $v = 0$, and $P = 0$.

We then solve for the concentrations of the diffusive quantities glutamate and potassium in both the fluid and the biofilm. In the fluid these equations are

$$D_G^{fl}\nabla^2 G - \nabla \cdot (G\langle u, v\rangle) = 0, \tag{4.17}$$

$$D_K^{fl}\nabla^2 K - \nabla \cdot (K\langle u, v\rangle) = 0, \tag{4.18}$$

with the boundary conditions $G = G_0$ and $K = K_0$ at the inlet, no-flux conditions at the interior walls in which $\nabla G \cdot \vec{n} = \nabla K \cdot \vec{n} = 0$, and far-field conditions at the outlet in which $\nabla G \cdot \vec{n} = \nabla K \cdot \vec{n} = 0$ where $\vec{n}$ represents the outward normal at the boundary. At the biofilm interface, the boundary conditions for G and K require that the concentrations and the fluxes are continuous across the interface, which lead to the following equations:

$$D_G \nabla G_{int} \cdot \vec{n} = D_G^{fl}\nabla G_{ext} \cdot \vec{n}, \tag{4.19}$$

$$G_{int} = G_{ext}, \tag{4.20}$$

$$D_K \nabla K_{int} \cdot \vec{n} = D_K^{fl}\nabla K_{ext} \cdot \vec{n}, \tag{4.21}$$

$$K_{int} = K_{ext}, \tag{4.22}$$

where G_{int}, G_{ext}, K_{int}, K_{ext} refer to the glutamate and potassium concentrations inside and outside the biofilm at the interface respectively, and $\vec{n}$ is the outward normal.

We solve the same equations as in the one-dimensional model for the diffusive quantities glutamate and potassium within the biofilm using Equations (4.1) and (4.2). We solve

the non-diffusive quantities, or the cellular state variables, only within the biofilm and not in the surrounding fluid. For the cellular state variables we use Equations (4.5-4.7) and (4.10-4.16) where the advection component of the equations uses the multidimensional biomass velocity and the multidimensional ∇ operator. We solve these equations on a two-dimensional grid that covers the flow-cell domain.

In the two dimensional model the growth equations, which replace Equations (4.8) and (4.9), use a potential function to approximate the viscous flow induced by the cellular growth throughout the biofilm

$$\Omega = \delta_{grow}\nabla^2 \left(M_{grow} \times G_{in}\right), \tag{4.23}$$

$$\vec{U} = \nabla\Omega, \tag{4.24}$$

where $\vec{U}$ evaluated at the boundary of the biofilm gives the directional growth of the boundary. We track the biofilm growth and the moving biofilm-fluid interface using the level-set method. The level-set method was introduced in [**48**] and discussed further in [**50**], [**56**], and references therein. Following work from [**5**], we use the zero level-set function of ϕ to track the biofilm interface, where ϕ solves the following equation:

$$\frac{\partial\phi}{\partial t} = \vec{U} \cdot \vec{n}||\nabla\phi||, \tag{4.25}$$

where $\vec{n}$ is the outward normal evaluated at the points along the biofilm boundary where $\phi = 0$. The level-set method ensures that the boundary grows at the rate determined by Equation (4.24). After implementing this set of equations within a two-dimensional simulation, we compare the model results to experiments.

4.3.1. Comparing the Two-Dimensional Model to Experiments

The true benefit of the two-dimensional model is that we can directly model the behavior of a biofilm from an experiment by inputting the colony's complex shape into the simulation. In this paper, we initialize a biofilm colony to be the same shape as a colony from the experiments in [**8**] with fluid flowing from left to right around the biofilm. The fluid velocity at the inlet is parabolic with a maximum velocity of 100 millimeters per hour in the center and 0 at the top and bottom of the flow cell. The velocity at the inlet was chosen to be fast enough so that both the leading and trailing edges of the colony participate in the oscillations, and it is not equal to the experimental velocity. Bacteria that are located farther from the fluid interface become stressed due to nutrient limitation, and they release potassium to hyperpolarize. This voltage change travels from the interior of the biofilm near the flow-cell wall to the exterior interface. In this process the whole biofilm hyperpolarizes.

The results of this model are shown in Figure 4.8 in which we can see the hyperpolarization and the potassium wave spread throughout the simulated biofilm. As the biofilm expands, the center of the biomass becomes consistently hyperpolarized because the biofilm is too large for these regions to receive sufficient nutrients even with the higher nutrient penetration resulting from the growth oscillations. As the biofilm grows, the regions that surround this hyperpolarized core also become stressed, and these bacteria hyperpolarize and initiate the potassium wave.

The spreading of this hyperpolarization can be seen in Figure 4.8 which shows the voltage and potassium within the biofilm during a hyperpolarization event. The voltage

plots show that the hyperpolarization moves from the center of the biomass to the fluid interface. The regions of the biofilm that are next to the fluid interface do not hyperpolarize as much as the center, but they still experience a significant level of hyperpolarization.

The potassium plots in Figure 4.8 show that the potassium pulse is initiated by bacteria at the edge of the hyperpolarized region. The initiating region forms a curve inside the biofilm that roughly follows the same shape as the biofilm boundary. Regions that are thicker, in this case the left and right side of the biofilm, experience a higher level of initial potassium release and hyperpolarization. After the initial potassium pulse, the potassium wave moves through the rest of the biofilm. The waves from the left and right side meet in the center of the colony, which causes this thinner region to hyperpolarize as well. The wave speed of the potassium signal in the model is about 10 microns per minute, which is similar to the wave speed seen in experiments. The experimental wave speed is demonstrated in [**9**] in which the authors show an example of a spreading potassium wave that travels at approximately 10 microns per minute. Each oscillation period lasts between two and three hours, which matches the oscillation period from experiments.

Potassium is not confined to the interior of the biofilm, and it diffuses out of the biofilm and flows downstream. The release of potassium affects other bacteria within the flow cell. We take a closer look at the effects of potassium within the fluid in the following section in which we model multiple biofilm colonies within the same flow cell.

We also model ThT fluorescence within the biofilm and compare these distributions to experimental data in Figure 4.9. The modeled ThT fluorescence does not match the experiment at every point, but the hyperpolarization pattern is qualitatively similar. In both the experiment and the model the fluorescence is high near the interior wall of the

flow cell, away from the fluid interface. We also see the spread of high fluorescence from the interior to the exterior, which indicates the spread of hyperpolarization.

Another spatial feature present in the data is the depolarization wave, which we see in the ThT fluorescence data from both the experiment and the model. In the experimental fluorescence data at Minute 20, we see a depolarization wave near the boundary of the region that is highly polarized and is fluorescing. The wave appears as a thin layer that is less fluorescent than the region above and below it, meaning that the area is less polarized. This wave front corresponds to bacteria that are experiencing a rise in the external potassium concentration and depolarize briefly before hyperpolarizing. We see a similar wave in the model data at Minute 20 just above the highly hyperpolarized center. The model can capture these important spatial components of this phenomenon, which allows for further study of these behaviors. Now that we have compared the simulated behavior of a single colony to the experimental data, we demonstrate the full utility of this two-dimensional model in modeling an entire flow cell in the following section.

4.3.2. Modeling Multiple Biofilm Colonies within a Flow Cell

One-dimensional models are not able to capture the interactions between multiple colonies within a single flow cell. However, many of the experiments performed on this biofilm system are implemented within flow cells with multiple colonies of biofilm. The flow cells often have multiple cell traps that catch bacteria in the fluid and provide the base for distinct colonies. These colonies grow and influence their neighbors both by consuming glutamate and by releasing potassium. We demonstrate that this simulation developed here is capable of modeling flow cells with multiple colonies.

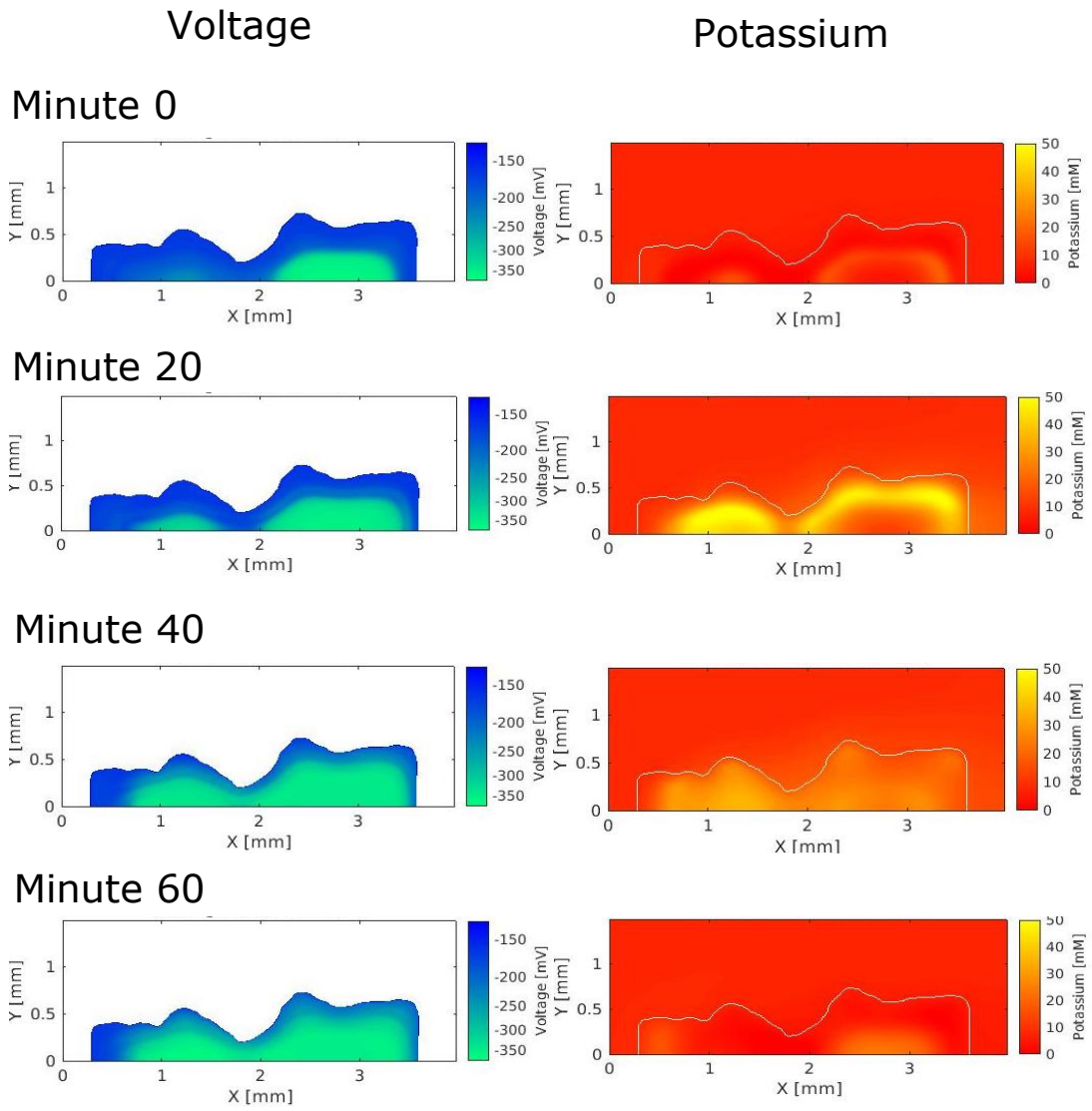

Figure 4.8. Voltage and potassium within a two-dimensional biofilm simulation during one oscillation. In the plots of the potassium concentration, particularly at Minute 20, you can clearly observe the potassium wave.

We use our two-dimensional simulation to model multiple colonies in a two-dimensional flow cell that is 3 millimeters by 3 millimeters. The fluid velocity at the inlet is parabolic with a maximum velocity of 10 millimeters per hour in the center and 0 at the top and bottom of the flow cell. The velocity at the inlet was chosen so that each colony oscillates

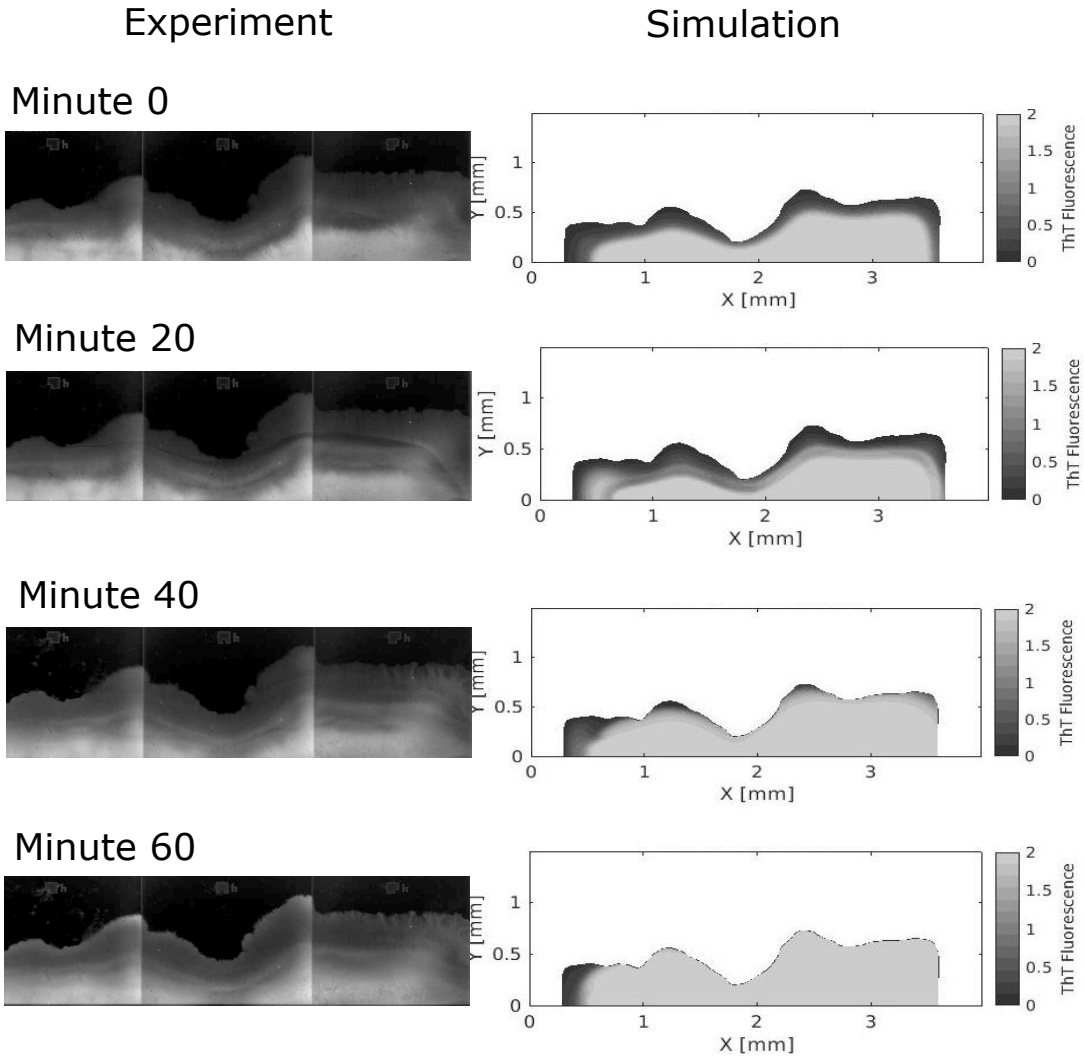

Figure 4.9. ThT fluorescence from an experiment compared to a simulation during one oscillation. The imaged region in the experimental data has a length of 3mm and a height of 1mm. The two vertical lines in the experimental fluorescence data correspond to slight changes in the flow-cell depth.

at its initial size, and it is not equal to the experimental velocity. We calculate the voltage, potassium, and ThT from the experimental setup in [**8**], and we show the results in Figure 4.10. We simulate three colonies in the flow cell: a large colony on the bottom

and two smaller colonies above the larger one. The large colony begins to oscillate first because its size leads the bacteria at its center to become nutrient starved at an earlier time than the bacteria in the other colonies. We see that the oscillations in voltage, potassium, and ThT of each colony in the model are synchronized since they are driven by the hyperpolarization of the largest biofilm at the bottom wall. In the experimental ThT fluorescence in Figure 4.10 we also see the synchronization of the oscillations that are driven by the larger biofilm at the bottom of the flow cell. We will explore properties of this synchronization in future work.

4.4. Conclusion

In this chapter we introduced and discussed a new model for electrical communication in *B. subtilis*. We updated the propagation mechanism to depend on the change in potassium level instead of the absolute potassium level, which incorporates bacteria's ability to adjust to environmental changes and creates more robust oscillations. We also updated the boundary condition at the biofilm interface and the potassium leak mechanism so that the potassium and the voltage oscillations are more synchronized.

Using this new model, we explored the relationship between voltage, growth, and potassium, showing that the voltage and the growth follow a similar pattern to each other while the voltage differential and the extracellular potassium are closer to inversely related. We also examined the diffusive properties of the system including the size of the biofilm at its initial oscillation and the how a colony's size relates to its oscillation period.

We then turned this model into a two-dimensional system using the level-set method to track the boundary. The ability to simulate a two-dimensional biofilm allows us to

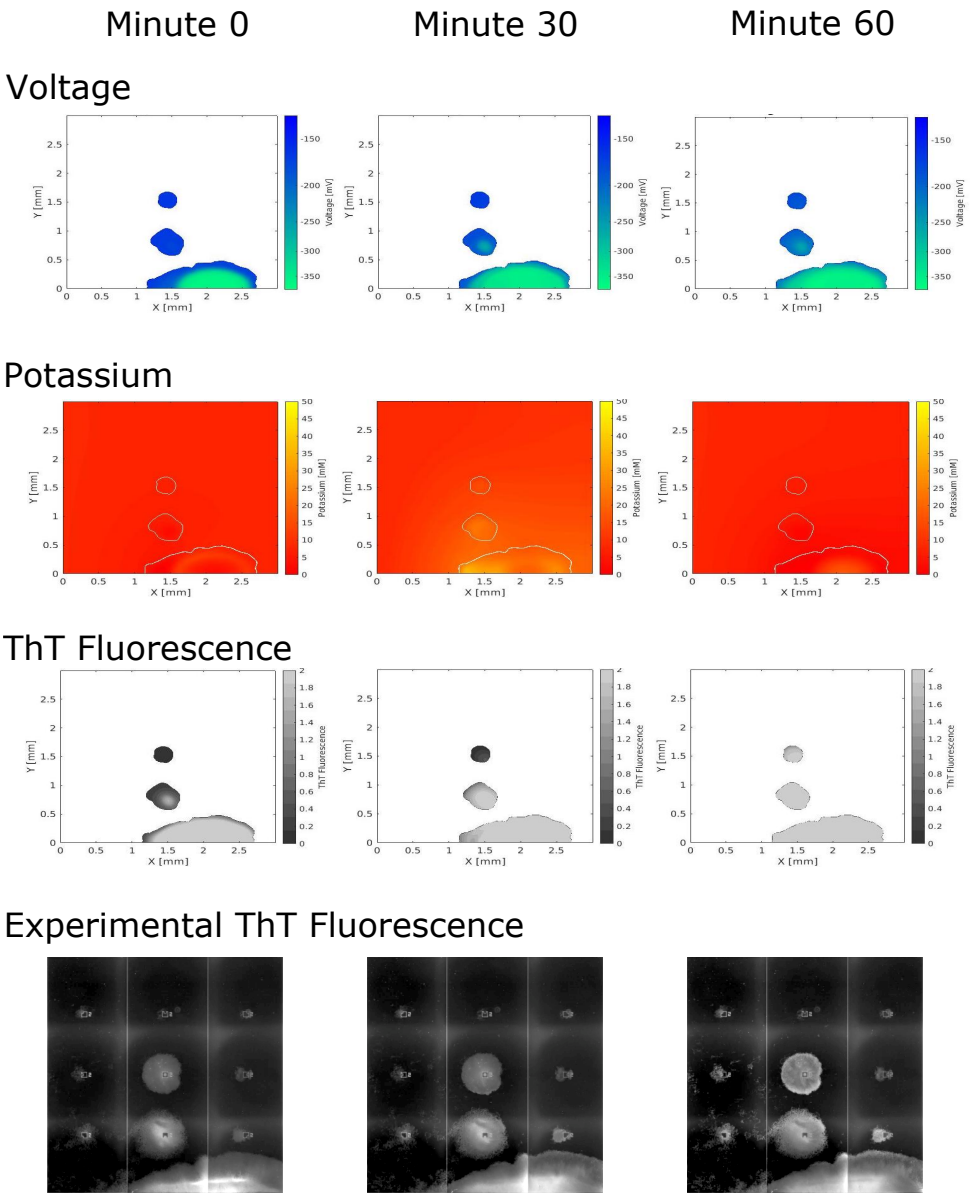

Figure 4.10. Voltage, potassium, and ThT fluorescence of multiple colonies within a single flow cell. We compare the data to experimental ThT fluorescence. The depolarization spreads between separated colonies as potassium diffuses within the fluid. The depolarization wave begins in the large colony on the bottom of the cell and spreads to the other colonies. The imaged region in the experimental data has a length of 3mm and a height of 3mm. The vertical line in the experimental fluorescence of the biofilm on the bottom wall corresponds to a slight change in the flow-cell depth.

copy a biofilm's shape from an experiment and closely compare the model to the physical system. We examined the voltage, the potassium, and the ThT and APG fluorescence within the model. We are also able to examine multiple colonies within a single flow cell and observe how separated colonies synchronize by releasing potassium into the flow. The model demonstrates synchronization patterns much like what we see in experiments.

This model can enable researchers to computationally explore this biofilm system in connection with their experiments. This model can be used to test hypotheses about the bacteria such as those relating to the growth speed, the affect of potassium on cells, and how collective oscillations can arise or fail to arise based on the individual behavior of the cells. The greatest benefit of this model is that we can directly compare the model's results to experiments by copying the shapes of the biofilms, which allows researchers to study the two-dimensional properties of the system. For example, researchers can study the wave speed of the potassium signal through spatially segregated cells of differing phenotypes. We can also explore properties such as the emergence of oscillations within a single colony and the synchronization between separated colonies within a single flow cell. Understanding the spatial properties of the system can help scientists find methods to control the biofilm's growth and dispersal in more realistic environments, potentially leading to new ways to treat biofilm growth and any associated infections.

In future research, we would like to further explore cellular metabolism and the synchronization of oscillations within a colony. First we would like to understand how a rise in external potassium disrupts cellular consumption. We believe that this study could provide a better understanding of the cellular mechanisms that create colony-wide oscillations. In particular, studying metabolism could give us further insight into the recovery

process of a cell and how it regulates growth. We would then like to explore how metabolism and changes in growth rates either lead to synchronicity within the colony or allow for regional divergence in oscillations within large biofilms.

This oscillatory behavior of *Bacillus subtilis* involves many complex processes, and we are just beginning to put the pieces together. Understanding the components of the oscillations could inspire new methods to influence and even control certain biofilms' behavior such as the attachment and growth of the colony. For example, scientists could discover a method to modify a biofilm's growth by solely changing the environmental potassium. These new control methods would not rely on harsh treatments such as antibiotics but on adjusting the biofilm's environmental conditions to influence its oscillatory behavior.

CHAPTER 5

Conclusion

Biofilms are communities of bacteria that exhibit complex behaviors enabling them to survive and even thrive in a range of environments. In the work presented here, we developed two models that capture several important aspects of biofilm behavior: a model that quantifies the large-scale dynamics of a biofilm flow cell and a model that explores a novel oscillatory phenomenon observed in *B. subtilis* as presented in [**8**].

We based these studies on the biofilm simulation system from [**5**] with a few important modifications. First, we replaced the fluid solver, which was based on an XFEM formulation, with a high-performance fluid solver that runs on a GPU. By replacing the fluid solver, the entire simulation's runtime decreased by around 80%. This significant gain in speed greatly improved our ability to perform quick simulations within the two projects. In addition to replacing the fluid solver, we modified the simulation so that it can track cellular state variables and solve for the state variables and the solutes as time dependent. These modifications in solving for the state and solute variables were necessary to simulate the oscillatory behavior observed in [**8**]. We used the modified simulation system to develop two novel models of biofilms' behavior.

In Chapter 3, we introduced a reduced model to approximate the nutrient concentrations and the biofilm growth throughout an experimental flow cell. Flow cells often have heterogeneous nutrient concentrations and fluid velocities within a single experiment that lead to varying biofilm growth patterns. To understand these growth patterns, we can

quantify the important elements of the flow cell using a model. Simulating an entire flow cell using previously available models is computationally expensive, particularly in three dimensions. In the reduced model, we used an asymptotic approximation to reduce the dimensionality of the problem and simplify the calculations. With this simplification, the model runs nearly 100 times faster than previous models for many grid sizes. The relative speed allows experimentalists to use this model to better understand the experimental environment. The model can quantify the distribution of quantities, such as oxygen, which are difficult to measure within the confines of the experiment, and it can predict the bacterial growth in parts of the flow cell that may not be directly observable. This model connects biofilms' growth to the heterogeneous environment in the flow cell. The environmental heterogeneity seen in flow cells is often present in real-world settings such as in water pipes and in catheters. By studying the biofilm growth in these flow cells, scientists can better understand the formation of biofilms in many other environments.

In Chapter 4, we developed a modified model of an oscillatory growth pattern observed in experiments from [**8**], and we used this model to create a two-dimensional simulation. The model describes a biofilm in which starving cells at the center of the biofilm initiate each oscillation using a potassium signal. The potassium wave travels through the biofilm and interrupts the cellular consumption of the entire biofilm, allowing nutrients to diffuse deeper into the biofilm. Though a few scientists have developed models to describe this system, we presented a modified model with a modified cellular communication mechanism, and the modified model better matches the potassium dynamics of the experimental data. We used this modified model to develop a two-dimensional simulation that replicates the multidimensional wave patterns observed in experiments. This two-dimensional

model can be used to further explore the spatial dynamics of the two-dimensional oscillations. The oscillatory growth has primarily been studied in colonies formed by *B. subtilis*, but there is evidence that other species of bacteria, such as *P. aeruginosa*, may also react to potassium signaling [**82**]. This signaling could allow scientists to influence bacterial movement and biofilm growth through changes in potassium concentrations, which could lead to new, low-impact control strategies for biofilms in a variety of natural settings.

These two models provide a better understanding of biofilms' complex behaviors, notably as they grow in heterogeneous environments and as certain colonies exhibit oscillatory growth. A large portion of current research on biofilms focuses on mitigating certain biofilms' deleterious effects within the human body. In particular, scientists study biofilms on medical devices because they can lead to serious infections and even sepsis. Mitigating these infections requires examining and understanding the various complex behaviors of biofilms that allow colonies to survive. Experimentalists and modelers must work together to address these challenges.

In future research, we would like to improve the accuracy of the reduced model of a biofilm flow cell. In particular, the asymptotic model assumes that the oxygen concentration profile has a parabolic shape in the flow. However, the oxygen profile may not relax to parabolic quickly enough to be accurately modeled as parabolic near the inlet or in fast flow. Approximating the profile as parabolic at locations where the assumption does not hold underestimates the oxygen usage and the growth of the biofilm at that location. One idea for improving this approximation is to use some piecewise-defined function that can capture the steep gradient of the oxygen profile near the biofilm interface.

In the oscillatory model, future work should examine oscillations in heterogeneous biofilm and the possible desynchronization of a biofilm's oscillations. Biofilms can exhibit spatial heterogeneity in which certain cell types cluster in different regions. We would like to explore how these variations in the biomass affect the emergence and the spread of oscillations. Future work should also address the possibility of desynchronization in biofilms' oscillations. We can consider a variety of variables that could lead to a potential desychronization, such as a biofilm's size or the environmental nutrient concentration. In certain cases, the regions of the biofilm could experience localized oscillations that do not influence the other parts of the biofilm. There are a large number of possible two-dimensional properties that can be explored using the two-dimensional model.

In future work, we would also like to develop a detailed, three-dimensional biofilm model. This three-dimensional model would allow us to study the intricate, higher-dimensional structures of biofilms. Most experimental data of biofilm growth is three-dimensional, and the ability to model the precise shapes of the biofilm would allow scientists to explore the properties inherent in these multi-dimensional structures.

Mathematical modeling provides a way to quantitatively study a variety of biological phenomena. Experimental biologists continue to discover and document a range of interesting phenomona that modelers can quantitatively explore. The unique behaviors of biofilms make up only a small subset of these novel, biological properties. While the methods used for modeling continue to evolve, modeling and simulation remain important tools that will lead to transformative discoveries in biology.

References

[1] Noah Ford and David Chopp. A dimensionally reduced model of biofilm growth within a flow cell. *Bulletin of mathematical biology*, 82(3):40, 2020.

[2] J. W Costerton. *The biofilm primer*. Springer series on biofilms, 1. Springer, Berlin ; New York, 2007.

[3] S. A. Crusz, R. Popat, M. T. Rybtke, Miguel M. Cámara, M. Givskov, T. Tolker-Nielsen, S. P. Diggle, and P. Williams. Bursting the bubble on bacterial biofilms: a flow cell methodology. *Biofouling*, 28(8):835–842, 2012.

[4] Wei Zhang, Tadas S. Sileika, Cheng Chen, Yang Liu, Jisun Lee, and Aaron I. Packman. A novel planar flow cell for studies of biofilm heterogeneity and flow–biofilm interactions. *Biotechnology and Bioengineering*, 108(11):2571–2582, 2011.

[5] Brian V Merkey, Bruce E Rittmann, and David L Chopp. Modeling how soluble microbial products (smp) support heterotrophic bacteria in autotroph-based biofilms. *Journal of Theoretical Biology*, 259(4):670–683, 2009.

[6] D. Chopp, M. Kirisits, B. Moran, and M. Parsek. The dependence of quorum sensing on the depth of a growing biofilm. *Bulletin of Mathematical Biology*, 65(6):1053–1079, 2003.

[7] Alessandro Culotti, Aaron I. Packman, and Kornelia Smalla. Pseudomonas aeruginosa facilitates campylobacter jejuni growth in biofilms under oxic flow conditions. *FEMS Microbiology Ecology*, 91(12), 2015.

[8] Arthur Prindle, Jintao Liu, Munehiro Asally, San Ly, Jordi Garcia-Ojalvo, and Gürol M Süel. Ion channels enable electrical communication in bacterial communities. *Nature*, 527(7576):59, 2015.

[9] Rosa Martinez-Corral, Jintao Liu, Arthur Prindle, Gürol M Süel, and Jordi Garcia-Ojalvo. Metabolic basis of brain-like electrical signalling in bacterial communities. *Philosophical transactions of the Royal Society of London. Series B, Biological sciences*, 374(1774):20180382, 2019.

[10] Jintao Liu, Arthur Prindle, Jacqueline Humphries, Marçal Gabalda-Sagarra, Munehiro Asally, Dong-Yeon D. Lee, San Ly, Jordi Garcia-Ojalvo, and Gürol M. Süel. Metabolic co-dependence gives rise to collective oscillations within biofilms. *Nature*, 523(7562):550, 2015.

[11] Rosa Martinez-Corral, Jintao Liu, Gürol M Süel, and Jordi Garcia-Ojalvo. Bistable emergence of oscillations in growing biofilms. *Proceedings of the National Academy of Sciences of the United States of America*, 115(36):E8333, 2018.

[12] Willem M De Vos. Microbial biofilms and the human intestinal microbiome. *npj Biofilms and Microbiomes*, 1(1), 2015.

[13] Michael Brandwein, Doron Steinberg, and Shiri Meshner. Microbial biofilms and the human skin microbiome. *npj Biofilms and Microbiomes*, 2(1):1, 2016.

[14] Philip D Marsh. Dental plaque as a biofilm and a microbial community – implications for health and disease. *BMC Oral Health*, 6(Suppl 1):S14–S14, 2006.

[15] Tom J. Battin, Katharina Besemer, Mia M. Bengtsson, Anna M. Romani, and Aaron I. Packmann. The ecology and biogeochemistry of stream biofilms.(report). *Nature Reviews Microbiology*, 14(4):251, 2016.

[16] Pablo C Bogino, María de Las Mercedes Oliva, Fernando G Sorroche, and Walter Giordano. The role of bacterial biofilms and surface components in plant-bacterial associations. *International journal of molecular sciences*, 14(8):15838, 2013.

[17] D. Dhanasekaran, N. Thajuddin, M. Rashmi, T. Deepika, and M. Gunasekaran. Screening of biofouling activity in marine bacterial isolate from ship hull. *International Journal of Environmental Science and Technology*, 6(2):197–202, 2009.

[18] J W Costerton, K J Cheng, G G Geesey, T I Ladd, J C Nickel, M Dasgupta, and T J Marrie. Bacterial biofilms in nature and disease. *Annual Reviews in Microbiology*, 41(1):435–464, 1987.

[19] Maria Kostakioti, Maria Hadjifrangiskou, and Scott J Hultgren. Bacterial biofilms: development, dispersal, and therapeutic strategies in the dawn of the postantibiotic era. *Cold Spring Harbor perspectives in medicine*, 3(4):a010306, 2013.

[20] Wei Hu, Zhe Yang, Renate Lux, Minglei Zhao, Jing Wang, Xuesong He, and Wenyuan Shi. Direct visualization of the interaction between pilin and exopolysaccharides of myxococcus xanthus with egfp-fused pila protein. *FEMS Microbiology Letters*, 326(1):23–30, 2012.

[21] Jean-Marc Ghigo. Natural conjugative plasmids induce bacterial biofilm development. *Nature*, 412(6845):442, 2001.

[22] Philip S Stewart and J William Costerton. Antibiotic resistance of bacteria in biofilms. *The Lancet*, 358(9276):135–138, 2001.

[23] C.A. Fux, S. Wilson, and P. Stoodley. Detachment characteristics and oxacillin resistance of staphyloccocus aureus biofilm emboli in an in vitro catheter infection model. *Journal of Bacteriology*, 186(14):4486–4491, 2004.

[24] Thien-Fah Mah, Betsey Pitts, Brett Pellock, Graham C. Walker, Philip S. Stewart, and George A. O'Toole. A genetic basis for pseudomonas aeruginosa biofilm antibiotic resistance. *Nature*, 426(6964):306, 2003.

[25] Wen Ma, Magdalena Panecka, Nathalie Tufenkji, and Md. Saifur Rahaman. Bacteriophage-based strategies for biofouling control in ultrafiltration: In situ biofouling mitigation, biocidal additives and biofilm cleanser. *Journal of Colloid And Interface Science*, 523:254–265, 2018.

[26] Whonchee Lee, Zbigniew Lewandowski, Per H Nielsen, and W Allan Hamilton. Role of sulfate-reducing bacteria in corrosion of mild steel: A review. *Biofouling*, 8(3):165–194, 1995.

[27] Chee Meng Pang and Wen-Tso Liu. Biological filtration limits carbon availability and affects downstream biofilm formation and community structure. *Applied and Environmental Microbiology*, 72(9):5702, 2006.

[28] R W Bernard, W M Stahl, and R M Chase. Subclavian vein catheterizations: a prospective study. ii. infectious complications. *Annals of surgery*, 173(2):191, 1971.

[29] J W Costerton, P S Stewart, and E P Greenberg. Bacterial biofilms: a common cause of persistent infections. *Science (New York, N.Y.)*, 284(5418):1318, 1999.

[30] Matthew R. Parsek and Pradeep K. Singh. Bacterial biofilms: an emerging link to disease pathogenesis. *Annual Review of Microbiology*, 57:677, 2003.

[31] Hong Wu, Claus Moser, Heng-Zhuang Wang, Niels Høiby, and Zhi-Jun Song. Strategies for combating bacterial biofilm infections. *International Journal of Oral Science*, 7(1), 2014.

[32] PS Stewart. A review of experimental measurements of effective diffusive permeabilities and effective diffusion coefficients in biofilms. *Biotechnology And Bioengineering*, 59(3):261–272, 1998.

[33] Julian W.T Wimpenny and Ric Colasanti. A unifying hypothesis for the structure of microbial biofilms based on cellular automaton models. *FEMS Microbiology Ecology*, 22(1):1–16, 1997.

[34] Jan-Ulrich Kreft, Ginger Booth, and Julian W.T. Wimpenny. Bacsim, a simulator for individual-based modelling of bacterial colony growth. *Microbiology*, 144(12):3275, 1998.

[35] O. Wanner and W. Gujer. A multispecies biofilm model. *Biotechnology and Bioengineering*, 28(3):314–328, 1986.

[36] I. Klapper and J. Dockery. Finger formation in biofilm layers. *SIAM Journal on Applied Mathematics*, 62(3):853, 2002.

[37] C Picioreanu, M C van Loosdrecht, and J J Heijnen. A new combined differential-discrete cellular automaton approach for biofilm modeling: application for growth in gel beads. *Biotechnology and bioengineering*, 57(6):718, 1998.

[38] C Picioreanu, M C van Loosdrecht, and J J Heijnen. Mathematical modeling of biofilm structure with a hybrid differential-discrete cellular automaton approach. *Biotechnology and bioengineering*, 58(1):101, 1998.

[39] Chrysi S Laspidou and Bruce E Rittmann. Evaluating trends in biofilm density using the umcca model. *Water Research*, 38(14-15):3362–3372, 2004.

[40] Ju Kreft, C Picioreanu, Jwt Wimpenny, and Mcm van Loosdrecht. Individual-based modelling of biofilms. *Microbiology-Sgm*, 147:2897–2912, 2001.

[41] Cristian Picioreanu, Jan-Ulrich Kreft, and Mark C. M van Loosdrecht. Particle-based multidimensional multispecies biofilm model. *Applied and Environmental Microbiology*, 70(5):3024, 2004.

[42] Joao B. Xavier, Cristian Picioreanu, and Mark C. M. Van Loosdrecht. A framework for multidimensional modelling of activity and structure of multispecies biofilms. *Environmental Microbiology*, 7(8):1085–1103, 2005.

[43] Erik Alpkvist and Isaac Klapper. A multidimensional multispecies continuum model for heterogeneous biofilm development. *Bulletin of Mathematical Biology*, 69(7):2445–2445, 2007.

[44] Brian Merkey. Biofilm modeling for wastewater treatment: Multiple species and multiple components, 2008.

[45] Brian Merkey and David Chopp. The performance of a microbial fuel cell depends strongly on anode geometry: A multidimensional modeling study. *Bulletin of Mathematical Biology*, 74(4):834–857, 2012.

[46] Brian Merkey and David Chopp. Modeling the impact of interspecies competition on performance of a microbial fuel cell. *Bulletin of Mathematical Biology*, 76(6):1429–1453, 2014.

[47] Bryan Smith, Benjamin Vaughan, and David Chopp. The extended finite element method for boundary layer problems in biofilm growth. *Communications in Applied Mathematics and Computational Science*, 2(1):35–56, 2007.

[48] Stanley Osher and James A Sethian. Fronts propagating with curvature-dependent speed: Algorithms based on hamilton-jacobi formulations. *Journal of Computational Physics*, 79(1):12–49, 1988.

[49] J A Sethian. A fast marching level set method for monotonically advancing fronts. *Proceedings of the National Academy of Sciences of the United States of America*, 93(4):1591, 1996.

[50] J.A. Sethian. *Level Set Methods and Fast Marching Methods: Evolving Interfaces in Computational Geometry, Fluid Mechanics, Computer Vision, and Materials Science*. Cambridge Monographs on Applied and Computational Mathematics. Cambridge University Press, 1999.

[51] Stanley Osher. *Level set methods and dynamic implicit surfaces*. Applied mathematical sciences (Springer-Verlag New York Inc.) ; v. 153. Springer, New York, 2002.

[52] D Adalsteinsson and J.A Sethian. The fast construction of extension velocities in level set methods. *Journal of Computational Physics*, 148(1):2–22, 1999.

[53] David L Chopp. Computing minimal surfaces via level set curvature flow. *Journal of Computational Physics*, 106(1):77–91, 1993.

[54] Mark Sussman, Peter Smereka, and Stanley Osher. A level set approach for computing solutions to incompressible two-phase flow. *Journal of Computational Physics*, 114(1):146–159, 1994.

[55] David L. Chopp. Some improvements of the fast marching method. *SIAM Journal on Scientific Computing*, 23(1):230–244, 2001.

[56] S. Osher and R. Fedkiw. *Level Set Methods and Dynamic Implicit Surfaces*. Springer Verlag, 2003.

[57] J. Dockery and I. Klapper. Finger formation in biofilm layers. *SIAM J. Appl. Math.*, 62(3):853–869, 2001.

[58] B. E. Rittmann. Communication. personal communication, 2002.

[59] R. Bakke, W. G. Characklis, M. H. Turakhia, and A. Yeh. *Biofilms*, chapter Modeling a Monopopulation Biofilm System: *Pseudomonas aeruginosa*. John Wiley and Sons, New York, 1990.

[60] B. E. Rittmann and P. McCarty. *Environmental Biotechnology*. McGraw Hill, New York, 2001.

[61] David R. Lide, editor. *CRC Handbook of Chemistry and Physics*. Cleveland, Ohio : CRC Press, Boca Raton, FL, 71 edition, 1990.

[62] K. J. Williamson and P. L. McCarty. Verification studies of the biofilm model for bacterial substrate utilization. *J. Water Pol. Cont. Fed.*, 48:281–289, 1976.

[63] Bruce E. Rittman. The effect of shear stress on biofilm loss rate. *Biotechnology and Bioengineering*, 24(2):501–506, 1982.

[64] D L Chopp, M J Kirisits, B Moran, and M R Parsek. A mathematical model of quorum sensing in a growing bacterial biofilm. *Journal of Industrial Microbiology and Biotechnology*, 29(6):339–346, 2002.

[65] Karen D. Xu, Philip S. Stewart, Fuhu Xia, Ching-Tsan Huang, and Gordon A McFeters. Spatial physiological heterogeneity in pseudomonas aeruginosa biofilm is determined by oxygen availability. *Applied and Environmental Microbiology*, 64(10), 1998.

[66] Ravindra Duddu, David L. Chopp, and Brian Moran. A two-dimensional continuum model of biofilm growth incorporating fluid flow and shear stress based detachment. *Biotechnology and Bioengineering*, 103(1):92–104, 2009.

[67] Isaac Klapper. Productivity and equilibrium in simple biofilm models. *Bulletin of Mathematical Biology*, 74(12):2917–2934, 2012.

[68] L. Gary Leal. *Laminar flow and convective transport processes : scaling principles and asymptotic analysis*. Butterworth-Heinemann series in chemical engineering. Butterworth-Heinemann, Boston, 1992.

[69] Arne De Coninck, Bernard De Baets, Drosos Kourounis, Fabio Verbosio, Olaf Schenk, Steven Maenhout, and Jan Fostier. Needles: Toward large-scale genomic prediction with marker-by-environment interaction. *Genetics*, 203(1):543–555, 2016.

[70] Fabio Verbosio, Arne De Coninck, Drosos Kourounis, and Olaf Schenk. Enhancing the scalability of selected inversion factorization algorithms in genomic prediction. *Journal of Computational Science*, 22(Supplement C):99 – 108, 2017.

[71] D. Kourounis, A. Fuchs, and O. Schenk. Towards the next generation of multiperiod optimal power flow solvers. *IEEE Transactions on Power Systems*, PP(99):1–10, 2018.

[72] David L. Chopp. Another look at velocity extensions in the level set method. *SIAM Journal on Scientific Computing*, 31(5):3255–3273, 2009.

[73] Laurent Demaret, Hermann J. Eberl, Messoud A. Efendiev, and Piotr Maloszewski. A simple bioclogging model that accounts for spatial spreading of bacteria. *Electronic Journal of Differential Equations*, 2009(17):51–69, 2009.

[74] Jan Gundlach, Christina Herzberg, Dietrich Hertel, Andrea Thürmer, Rolf Daniel, Hannes Link, and Jörg Stülke. Adaptation of bacillus subtilis to life at extreme potassium limitation. *mBio*, 8(4), 2017.

[75] Jintao Liu, Rosa Martinez-Corral, Arthur Prindle, Dong-Yeon D Lee, Joseph Larkin, Marçal Gabalda-Sagarra, Jordi Garcia-Ojalvo, and Gürol M Süel. Coupling between distant biofilms and emergence of nutrient time-sharing. *Science (New York, N.Y.)*, 356(6338):638, 2017.

[76] Joseph W. Larkin, Xiaoling Zhai, Kaito Kikuchi, Samuel E. Redford, Arthur Prindle, Jintao Liu, Sacha Greenfield, Aleksandra M. Walczak, Jordi Garcia-Ojalvo, Andrew Mugler, and Gurol M. Suel. Signal percolation within a bacterial community.(author abstract). *Cell Systems*, 7(2):137, 2018.

[77] B Tolner, T Ubbink-Kok, B Poolman, and WN Konings. Characterization of the proton/glutamate symport protein of bacillus subtilis and its functional expression in escherichia coli. *The Journal of Bacteriology*, 177(10):2863, 1995.

[78] A. L. Hodgkin and A. F. Huxley. A quantitative description of membrane current and its application to conduction and excitation in nerve. *Journal of Physiology*, 117(4):500–544, 1952.

[79] Wolfgang Epstein. Osmoregulation by potassium transport in escherichia coli. *FEMS Microbiology Letters*, 39(1-2):73–78, 1986.

[80] Jean Meury and Adam Kepes. The regulation of potassium fluxes for the adjustment and maintenance of potassium levels in escherichia coli. *European Journal of Biochemistry*, 119(1):165–170, 1981.

[81] Hannah Schramke, Vera Laermann, Halina E. Tegetmeyer, Andreas Brachmann, Kirsten Jung, and Karlheinz Altendorf. Revisiting regulation of potassium homeostasis in escherichia coli: the connection to phosphate limitation. *MicrobiologyOpen*, 6(3):n/a–n/a, 2017.

[82] Jacqueline Humphries, Liyang Xiong, Jintao Liu, Arthur Prindle, Fang Yuan, Heidi A Arjes, Lev Tsimring, and Gürol M Süel. Species-independent attraction to biofilms through electrical signaling. *Cell*, 168(1-2):200–209.e12, 2017.